THE SOLID STATE PARTICLE DETECTOR

and

THE $Be^9(d,a)Li^7$ REACTION

by

EDWARD GEORGE AULD
B. A. Sc., University of British Columbia, 1959.

A THESIS SUBMITTED IN PARTIAL FULFILMENT OF
THE REQUIREMENTS FOR THE DEGREE OF

MASTER OF SCIENCE

in the Department
of

Physics

We accept this thesis as confirming to the required standard

THE UNIVERSITY OF BRITISH COLUMBIA

August, 1961.

In presenting this thesis in partial fulfilment of the requirements for an advanced degree at the University of British Columbia, I agree that the Library shall make it freely available for reference and study. I further agree that permission for extensive copying of this thesis for scholarly purposes may be granted by the Head of my Department or by his representatives. It is understood that copying or publication of this thesis for financial gain shall not be allowed without my written permission.

Department of Physics

The University of British Columbia,
Vancouver 8, Canada.

Date August 15th, 1961.

ABSTRACT

The important characteristics (the window thickness and energy linearity range) of an RCA type A solid state charged particle detector were measured for protons, tritons, and alpha particles. The window thickness varies from 150 Kev for protons to 1.00 Mev for alpha particles. The maximum energy of the linearity range varies from 5 Mev for protons to 20 Mev for alpha particles.

The RCA detector was then used to study the reaction products from bombarding Be^9 with .500 to 1.35 Mev deuterons. The following reactions were studied in detail:

(i) the angular distribution of the alpha particle transition to the ground (a_1) and first (a_2) excited state of Li^7 in the reaction $Be^9(d,a)Li^7$. The ground state transition fits an analytical curve of the type: $a + b\cos\theta + c\cos\theta^2$, where θ is the angle of emission in the centre of mass coordinates of the reaction products. The ratio a:b:c is approximately: (1): (-.7): (.5). Neglecting the minimum near 150 degrees in the a_2 distribution, if fits a curve of the type $a + b\cos\theta + c\cos^2\theta$ where a:b:c is approximately (1):(.4): (.15).

(ii) the angular distribution of the triton transition to the ground state of Be^8 in the reaction $Be^9(d,t)Be^8$.

An indication of an alpha transition to a $5.64 \pm .11$ Mev excited state in Li^7 was found. No indication of a 6.5 Mev level in Li^7 was found.

Included as an appendix in this report, is a description of the recently installed Corona Stabilizer. The Corona Stabilizer supplies the feedback control that stabilizes the Van de Graaff accelerator energy at any set value.

ACKNOWLEDGEMENTS

The author wishes to thank Dr. K. L. Erdman for his assistance throughout all phases of this research. His suggestion especially on electronic problems, saved many hours of fruitless endeavour. Useful discussions with Dr. G. M. Griffiths and Dr. B. L. White aided considerably in the interpretation of the experimental results.

Thanks are due to Mr. D. Lindquist for his many helpful suggestions concerning the operation of the Corona Stabilizer.

The author gratefully acknowledges the receipt of an NRC Bursary and a scholarship from the British Columbia Telephone Company.

TABLE OF CONTENTS

LIST OF ILLUSTRATIONS

In Body of Text:

After Main Text:

I. INTRODUCTION

The solid state detector is a relatively new tool for the charged-particle spectroscopist, having been developed in the past ten years. McKay and McAfee (51) were one of the original discoverers of the properties that led to the semiconductor diodes usefulness in this field of study. Up until the past year most of the work in the field of these semiconductor charged particle detectors has been channeled into the construction and improvement of the devices. The symposium on Solid State Radiation Detectors, Oct. 3-5, 1960, sponsored by the IRE professional group on Nuclear Science is a good example of the general pre-occupation on device characteristics. Now, however several groups are reported to be using these devices in different applications, such as:

(i) nuclear reaction angular distribution measurements (Dearnaley, 61: Amsel et al. 61).

(ii) electron detection (McKenzie and Ewan, 61).

(iii) fission product measurements (Joyner et al. 61).

(iv) fast neutron spectroscopy (Love and Murray, 61).

One of the purposes of this investigation was to test the solid state devices adaptability to the study of nuclear reactions. The preliminary studies were done by using the device to detect the scattered protons from a thin Nickel target. Further studies of the devices characteristics were done with the reaction products of the bombarding of Be^9 with deuterons.

The main purpose of this investigation was to study the reaction $Be^9(d,a)Li^7$. Up until now, no one had adequately resolved the alpha transitions to the ground and

first excited state of Li^7 so that an angular distribution of these reactions could be measured. The angular distributions have been measured here at several energies. Other groups (Gelinas and Hanna, 53), have resolved these two alpha transitions using magnetic spectrometers, but their angular measurements were usually limited to one position.

The alpha transitions to the other excited states in Li^7 were studied in less detail, however a search was made for a state near 5.5 Mev. A level near this energy has been predicted by Wildermuth et al (61).

The break-up of the excited Li^7 nucleus into a triton and an alpha particle was studied to determine whether the 6.5 Mev state in Li^7 existed. Similar studies have been done by Jung and Cüer (56). Wildermuth et al (61) have cast some doubt on the existence of this excited state.

The angular distribution of the reaction $Be^9(d,t)Be^8$, was studied at three different energies. The reaction $Be^9(d,p)Be^{10}$, $Be^{10'}$ was not studied in any detail; the peaks corresponding to these transitions were only noted.

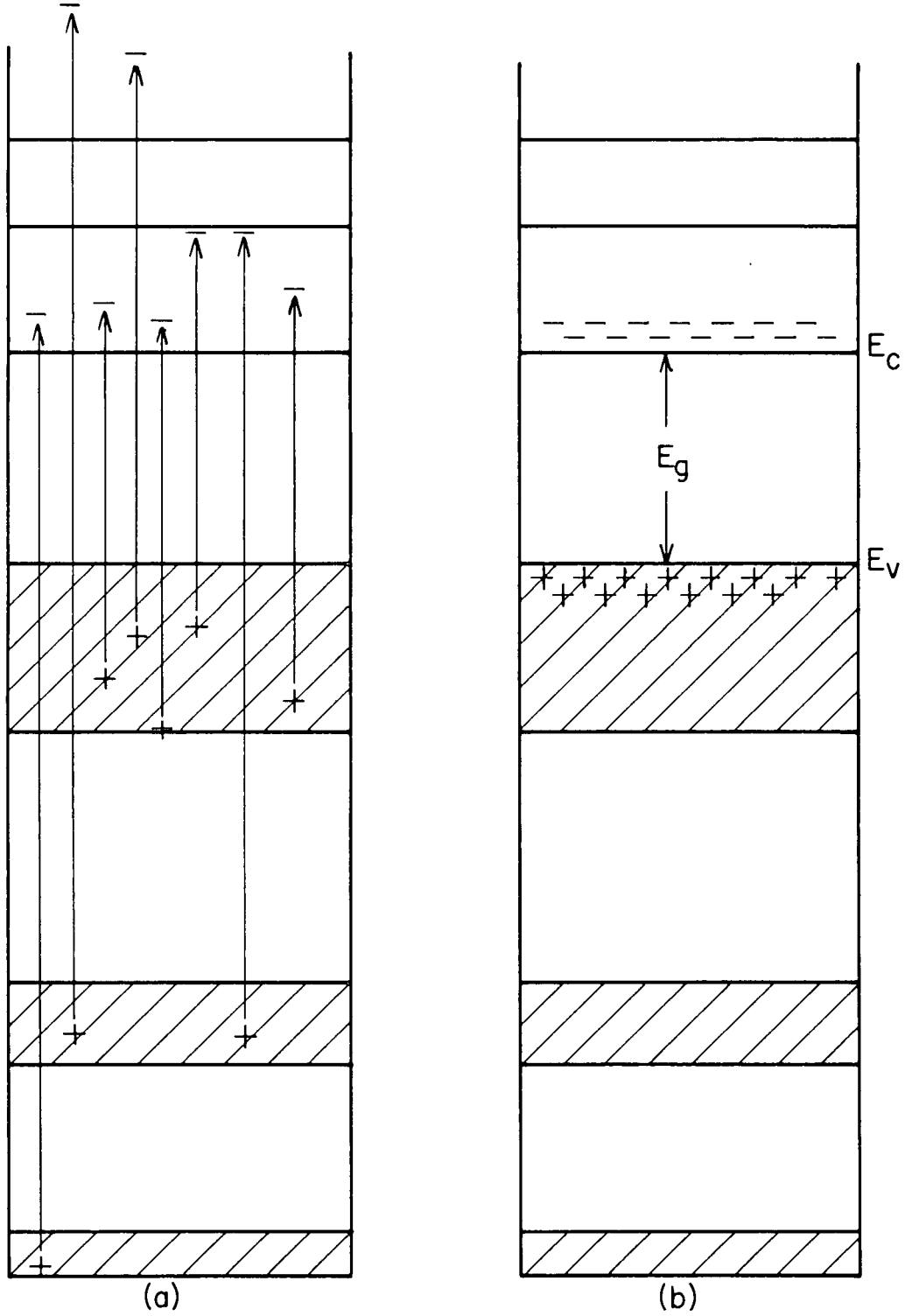

FIGURE 1: (a) Excitation of Electrons in a Semiconductor after the Passage of an Energetic Charged Particle.
(b) Residual Excitation after a time of approximately 10^{-12} sec.

II. THE SOLID STATE DETECTOR:

A. Theory of Operation

1. Interaction of a Charged Particle in a Solid:

Charged particles lose kinetic energy rapidly through interaction with the electrons of solids. For non-relativistic particles the maximum energy that can be transferred to an electron is approximately,

$$E_{max} \cong 4Em/M_1 \qquad (1)$$

where m is the electron mass and M_1 and E are the mass and energy of the heavy particle. In a semi-conductor these collisions may lift electrons from the valence to the conduction band but they may also lift electrons from deeper lying occupied bands. This is illustrated in Figure 1a. Electrons appear at various levels in normally full bands. This condition persists for only about 10^{-12} sec., after which the excited electrons drop to lower levels in the unoccupied band and the holes fill equivalent positions in the valence bands as illustrated in Figure 1b. During this de-excitation process, many more holes and electrons can be created. On the average this complex process results in the creation of one hole-electron pair for each 3.5 ev of energy lost by the incident heavy particle in Si (McKay and McAfee 51, 53). The final step in the de-excitation is the recombination of the electrons and holes in Figure 1b. It is important in semiconductor radiation detectors that the time for the last step not be too short.

A low value for the energy "e" required to form a hole-electron pair is advantageous in a counting device because the larger the number of electron-hole pairs produced per unit energy of the incident particle leads to a reduction in the statistical

fluctuations of the number of pairs produced. Silicon with an "e" of 3.5 ev per electron-hole pair offers a substantial gain in this respect over an air ionization chamber, in which the value of "e" is of the order of 30 ev per ion pair.

The energy gap between the valence and conduction band in Silicon is 1.1 ev. Shookley (60) has recently proposed a theory to explain why it takes 3.5 ev rather than 1.1 ev to produce an electron-hole pair in Silicon. He calculates "e" using constants determined from data on the quantum field for Photons (Vavilov, 59) in the visible and near ultraviolet (Chynoweth, 57). He obtains a value in good agreement with the measured 3.5 ev. The extra energy is wasted through strong coupling of electrons to lattice vibrations of the solid.

Experimentally no significant differences have been found in the value of "e" for a wide variety of particles and energies, although there must be a limit in which this is not the case. As a heavy primary particle slows down, it eventually comes to an energy below which the probability of producing pairs becomes very low and the principal interactions are Rutherford or hard-sphere collisions with the nuclei of the solids. Seitz (49) suggests that this energy is roughly

$$E_i \cong \frac{M_1 I}{8m} \qquad (2)$$

where I is the lowest excitation energy of the electronic system, the band energy gap in the case of a semiconductor. For alpha particles on Silicon, E_i is about 1 Kev. This energy is less than the best resolution yet obtained with solid state detectors.

2. Hole-Electron Pair Motion:

The holes and electrons created by a primary charged particle in a solid are

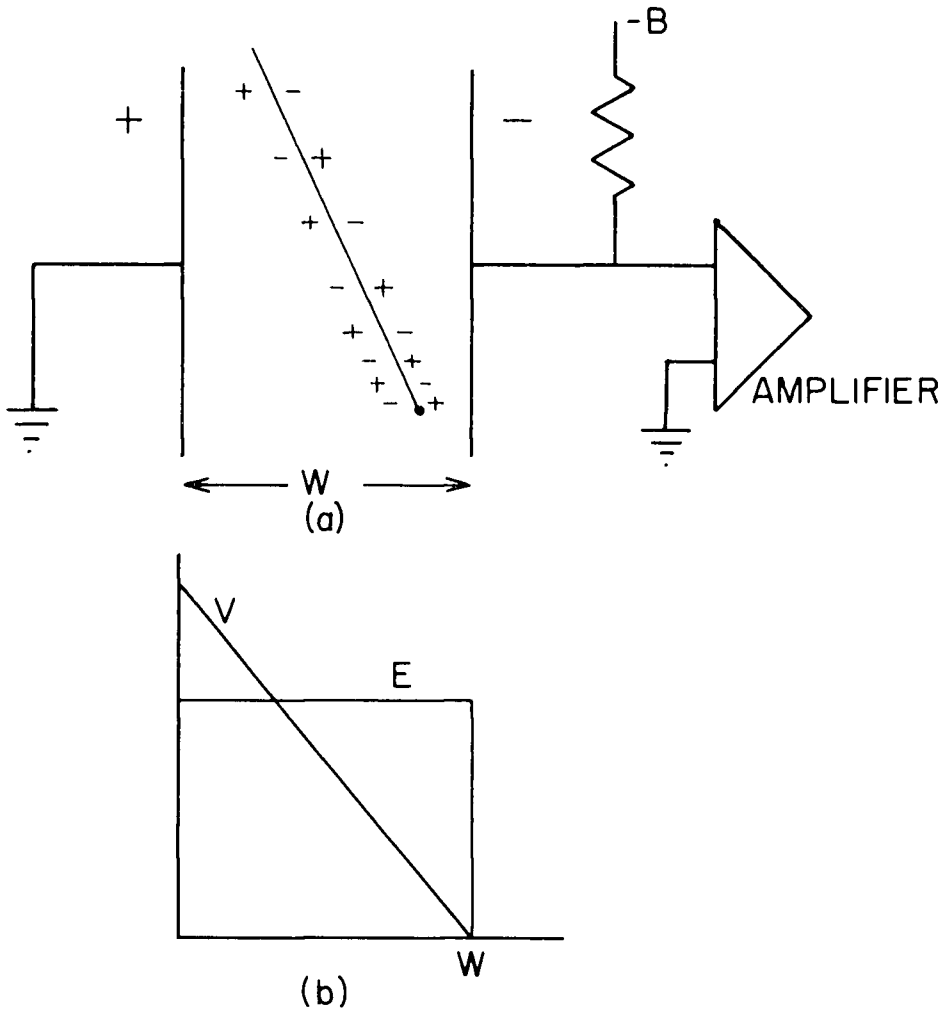

FIGURE 2: (a) Semiconductor Parallel Plate Ionization Chamber with Hole-electron pairs produced by an Energetic Charged Particle.
(b) Potential and Electric Field Distribution across the Chamber

analogous to the positive ions and electrons produced in a gas ionization chamber. The carriers drift in an electric field and give rise to an external current. The integral of the current, the collected charge, can be used as a measure of the energy deposited in the counter by the primary particle.

Figure 2. illustrates the situation for either a solid state detector or a gas ionization chamber in parallel plate geometry. In the electric field the electrons move toward the left and the ions or holes toward the right. The contribution of each carrier to the total current has been derived by Brown (61). The current caused by one carrier is given by (assuming parallel plate configuration)

$$i = \frac{quV}{x^2} \qquad (3)$$

where q is the electronic charge, u the carriers mobility, V the voltage across the device and x in the spacing between the plates. The total current is the sum of contributions of this kind for all the charged carriers. For Silicon at room temperature the electron mobility u_n is 1200 cm^2/volt-sec. and the hole mobility u_p is 500 cm^2/volt-sec.

The rise-time of the pulse in a solid state device is the transit time for a carrier across the device.

$$T_r = \frac{x}{v} = \frac{x}{uE} \qquad (4)$$

where v is the carrier drift velocity under the electric field E. The transit time will be approximately 10^{-7} sec. for the mobilities in silicon, field strengths of 10^3 volts/cm and transit distances of 1 mm. This is a great deal faster than the rise-time in gas ionization chambers of comparable stopping power, principally because of the relatively small transit distance required in the solid state detector. Unfortunately, the mobility

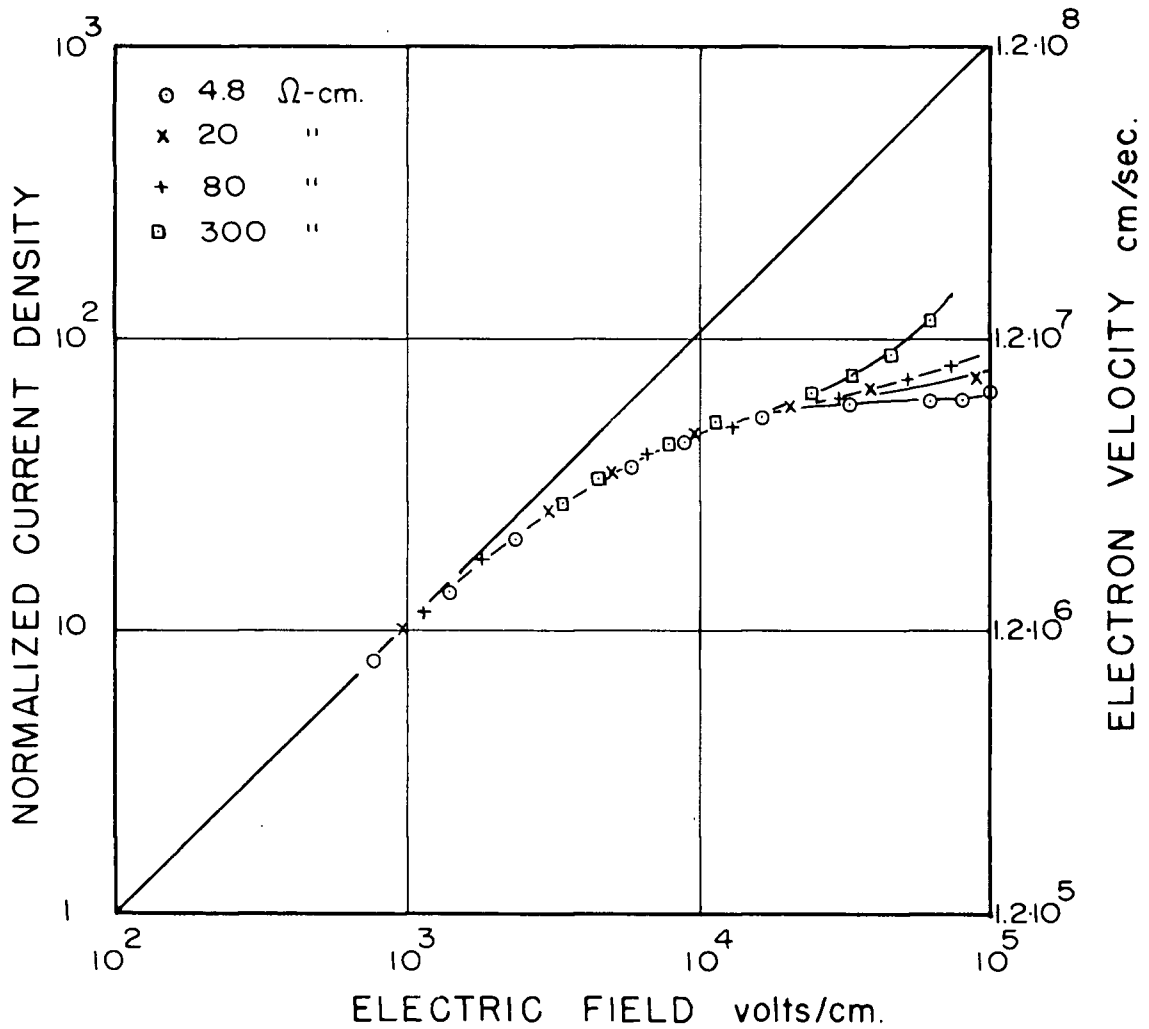

FIGURE 3:

ELECTRIC FIELD DEPENDENCE OF ELECTRON VELOCITY IN SILICON AT ROOM TEMPERATURE

is not a constant for high electric fields; there is an upper limit to the rise-time. Figure 3. is the work of Prior (60) and shows this effect. The vertical scale in the figure is proportional to the drift velocity of electrons. The linear increase in velocity with electric field ceases at fields above 10^3 volts/cm and the maximum electron velocity at 10^3 volts/cm has been obtained by increasing the electric field by a factor of 100.

Trapping of holes and electrons can alter this simple picture considerably. There are structural imperfections and chemical impurities in solids which have significant capture cross-section for the drifting electron. These trapping centres do not necessarily destroy the electron by returning it to the valence band but they interrupt its contribution to the current. The electron may be released and trapped several times before it reaches the edge of the field. The current contribution by this electron will be a group of spikes of random length and at random intervals whose sum is equal to the contribution of one electronic charge. In many cases the release time from the trap is much longer than a microsecond and the rise time of a pulse at the amplifier may be unusually slow. The release time of these traps is a strong function of the temperature. (Shulman and Wylunda, 56). A trap at low temperatures (130 degrees K) becomes a recombination centre at room temperature.

The carrier transit may be affected by recombination as well as trapping. A recombination may occur at a trapping centre if carriers of opposite signs are trapped. In the hole-electron track of a charged particle, as the electrons drift one way and the holes the other, the two particle clouds will be moving through one another until they are spatially separated. If during this time a recombination centre is exposed to both

holes and electrons it can carry out the two-step process which results in the removal of one hole and one electron from the flow. The recombination time, commonly called the lifetime, involves the capture cross-sections for electrons and for holes and the densities of recombination centres. For particle detection the electron and the hole must complete the transit of the field without interruption. This sets a practical limit on the dimension x. The average time an electron remains free before being trapped by centres with a density N_t and capture cross-section d_n is:

$$t_n = \frac{1}{N_t d_n v_n} \qquad (5)$$

where v_n is the thermal velocity of the electrons. For electron transit without significant trapping we require that $T_r << t_n$. A completely analogous situation exists for holes.

Since t_n can be as large as 100 usec. when appropriate care has been taken to reduce the N_t in the crystal, and considering the maximum drift velocity of 10^7 cm/sec., it should be possible to get transit without appreciable trapping across a distance of 10^3 cm. However, experimentally a realistic counter thickness is found to be of the order of 1 to 10 mm across the charge-depleted region. As mentioned, the density of trapping centres can be reduced to a point where t_n is 100 usec, but according to Brown (61) there are other considerations which limit t_n to a value of 10^{-7} to 10^{-8} sec. In the p-n junction device where the carrier lifetime can be long there are other considerations which limit "x" to the same range. These considerations are discussed in the next section.

3. Production of High Fields in Semiconductors:

The uniform field, parallel plate geometry can easily be achieved in a semiconductor counter, but the need for a high DC electric field demands special attention

FIGURE 4: SOLID STATE DIFFUSED JUNCTION DETECTOR

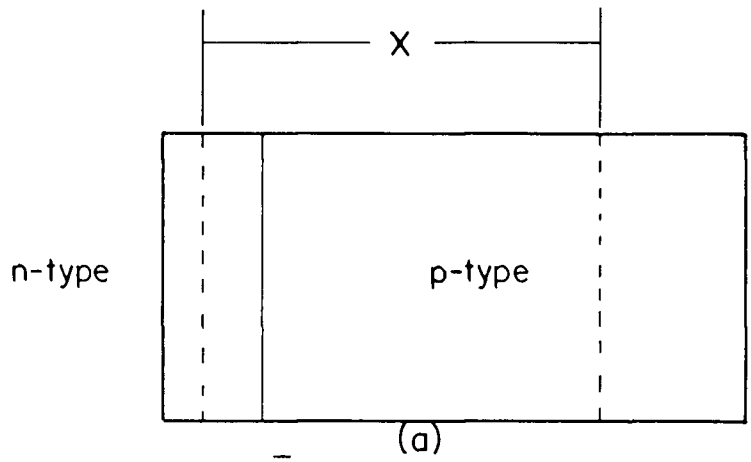

Charge-depleted Region of Detector

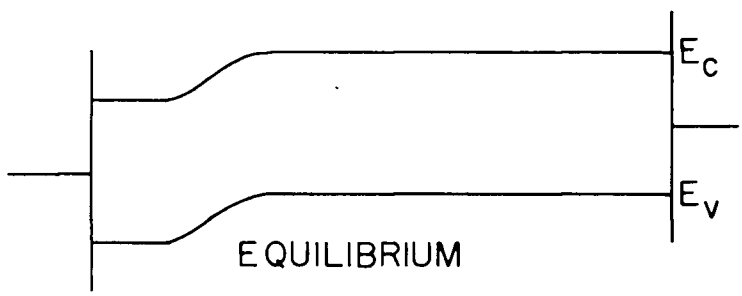

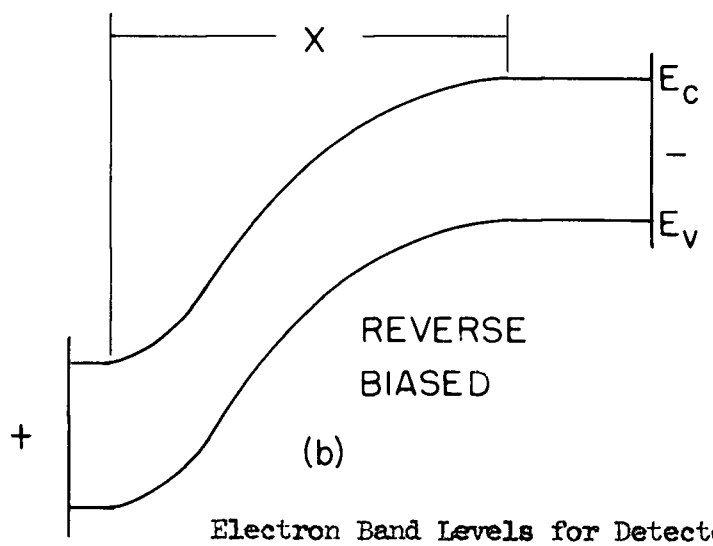

Electron Band Levels for Detector

to the DC current. The magnitude of the current resulting from hole-electron pairs produced by a charged particle is in the order of 10^{-6} amps. For a good device this current should be very large compared with the noise fluctuations in the DC current of the device. Obviously a high resistivity is required before any solid state device could be of any use. As an example; a device 5 mm^2 in area and 1 mm thick made of 1000 ohm-cm silicon, will have a resistance of about 500 ohms. At a field of 10^3 volts/cm it would carry a current of .2 amps and develop 20 watts. Such a resistivity is not nearly high enough. A resistivity of 10^{10} ohm-cm, for the same sized device would give a noise current of about 0.02 microamps; a more useful level of noise. Ways in which the resistivity of the material may be increased are discussed by Brown (61), and will not be discussed here.

There is a second way of achieving a high electric field in a semiconductor without having to use high resistivity material. This is through the use of a reverse biased p-n junction. A discussion of the principles of operation of this device will be aided by referring to Figure 4. This is a junction formed by diffusing donor impurities to a shallow depth into the surface of originally high purity p-type material. In the RCA solid state counter, as used in these experiments, the p-type material is silicon and the shallow layer at the surface is phosphorous. In this configuration a charge-depleted region is formed between the p-type and n-type material. This region contains an equal number of positive donors and negative acceptors. Since the density of the acceptors is relatively low the charge-depleted region is much wider on the p-type side than on the n-type side. The potential difference between the two sides may be

0.5 volts and the region may be 10^{-3} cm wide.

The electric field in the charge-depleted region may be reduced considerably by the cloud of holes and electrons produced by the passage of a charged particle. For a 1 Mev proton, in Silicon, the density of this cloud will be about 10^{18} pairs/cm^3. The electric field in the region of this plasma will be much less than in the rest of the depletion region. Therefore only the carriers on the surface of the plasma will be affected by the electric field. This plasma effect should increase the collection time beyond the simple transit time of a single charge in the field. An indication of an increase in collection time which may be attributed to this effect has been observed in fission fragment counting (Miller et al, 60).

The charge depleted width x may be increased with reverse bias. In the type of junction shown, the magnitude of x_p or x_n is given by:

$$x = \sqrt{k(V+V_o)/2qN_i} \qquad (6)$$

where x_p and x_n are the widths of the charge-depleted region in the p-type and n-type material. V_o is the potential barrier at zero bias volts V and N_i is the concentration of ionized impurity centres in the region considered, and k is the dielectric constant for the p-type material. In a diffused junction, $x_p/x_n = (d_n/d_p)^{\frac{1}{2}}$ may typically have a value of 10^3, where d_n and d_p are the conductivities of the n and p-type regions. Thus the major portion of the depletion region exists beyond the junction into the bulk of the p-type silicon, and only a small region exists in front of the junction approaching the surface. The charge-depleted region does not extend right to the surface of the n-type region, leaving a particle insensitive window. Since the resistivity of the material is

$$\rho = \frac{1}{(nqu_n + pqu_p)} \qquad (7)$$

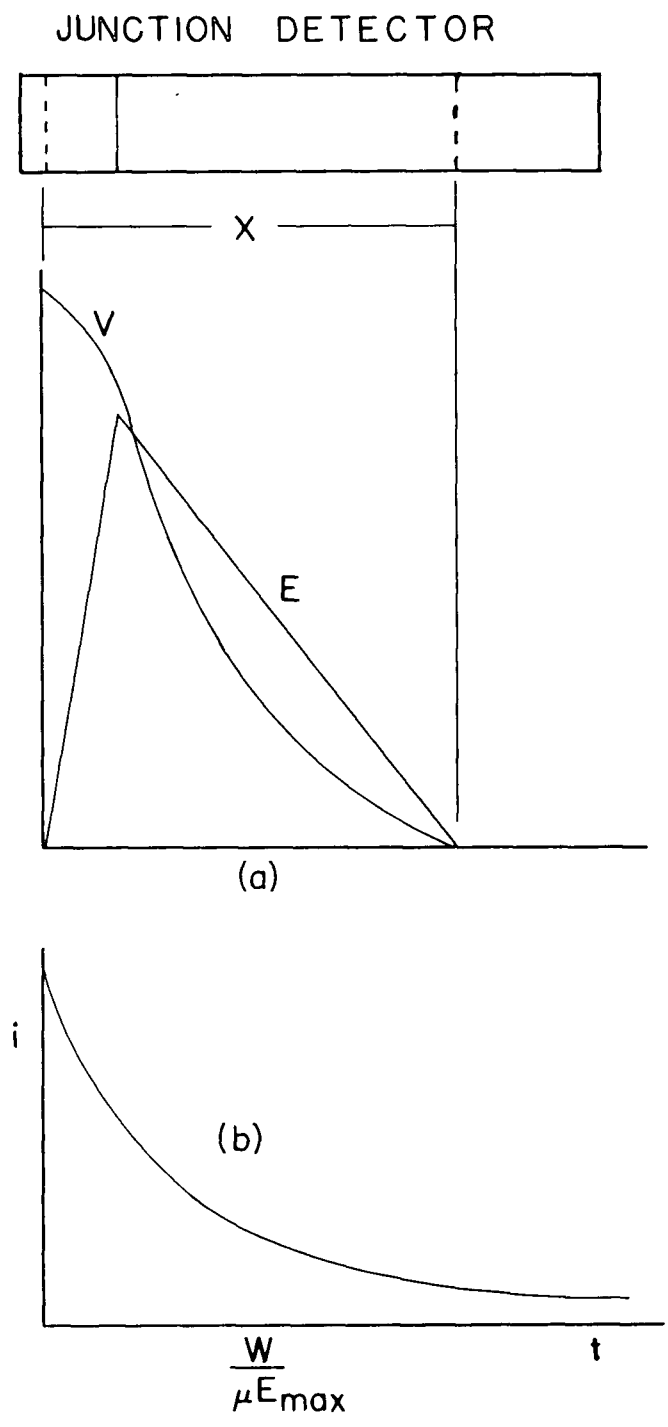

FIGURE 5: (a) Electric and Potential Field for a p-n junction detector under reverse bias.
(b) Current wave shape resulting from a hole produced at maximum field.

where n and p are the concentrations of electrons and holes, the width of the depletion region or sensitive depth of the device is proportional to $(u_p V)^{\frac{1}{2}}$. From this it can be seen that the combination of high resistivity and high applied voltage is required to utilize detectors that respond linearly to highly penetrating particles. The maximum applied voltage that can be used is governed by the reverse current noise level of the device. This level increases with increasing applied bias voltage.

The electric field in the charge-depleted region is not a constant. It is zero at the edges of the region and a maximum at the inner edge of the donor concentration, as shown in Figure 5a. The maximum field is given very approximately by:

$$E_{max} \approx \sqrt{8 q N_i V / k} \qquad (8)$$

A representative value of Emax is 10^4 volts/cm. When a charged particle is incident on the face of the device the resulting holes and electrons will be swept out of the charge-depleted region by this field. The current due to the motion of one carrier is (Brown 61),

$$i = \frac{qvE}{V} \qquad (9)$$

where E is the local electric at the position of the carrier. The total current is the sum of the contributions of this kind from all of the carriers produced by the charged particle. The shape of the current pulse in time, assuming constant mobility, is

$$i = \left[u_p E_m^2 q / V\right] e^{-(2u_p E_m t / x)} \qquad (10)$$

for carriers created at the position of the maximum field E_m. This current pulse is shown in the second half of Figure 5b.

Hole-electron pairs created outside the charge-depleted region do not contri-

FIGURE 6:

CHARGE COLLECTED VS TIME

(a) From Charge-depleted Region
(b) From Field-free Region

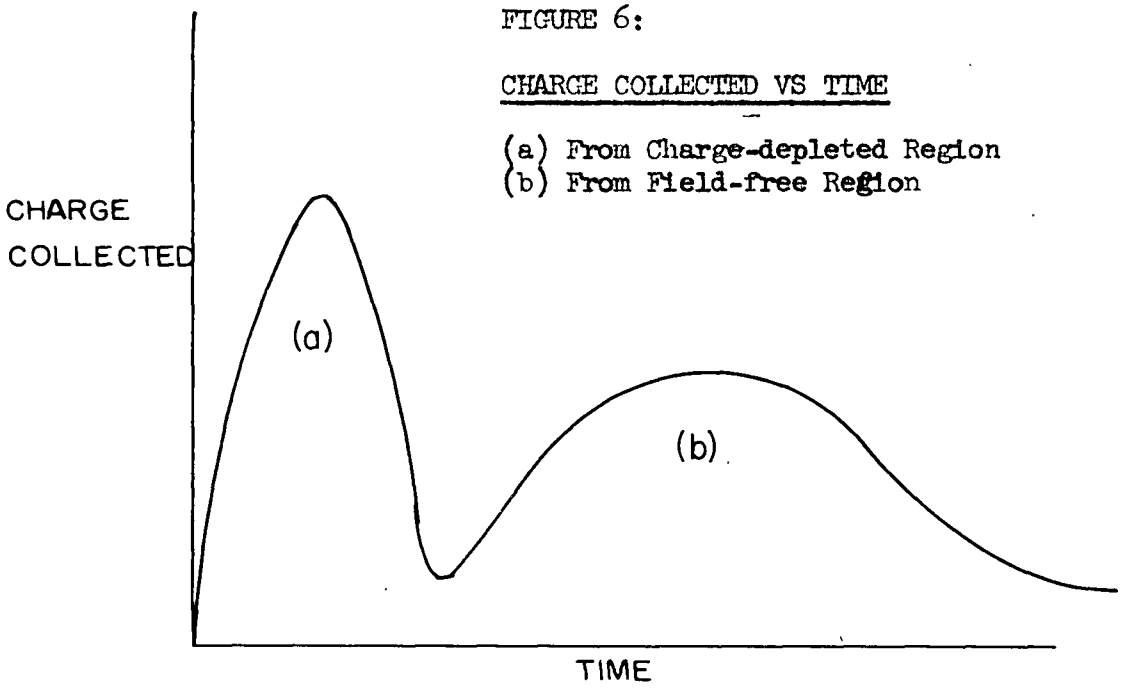

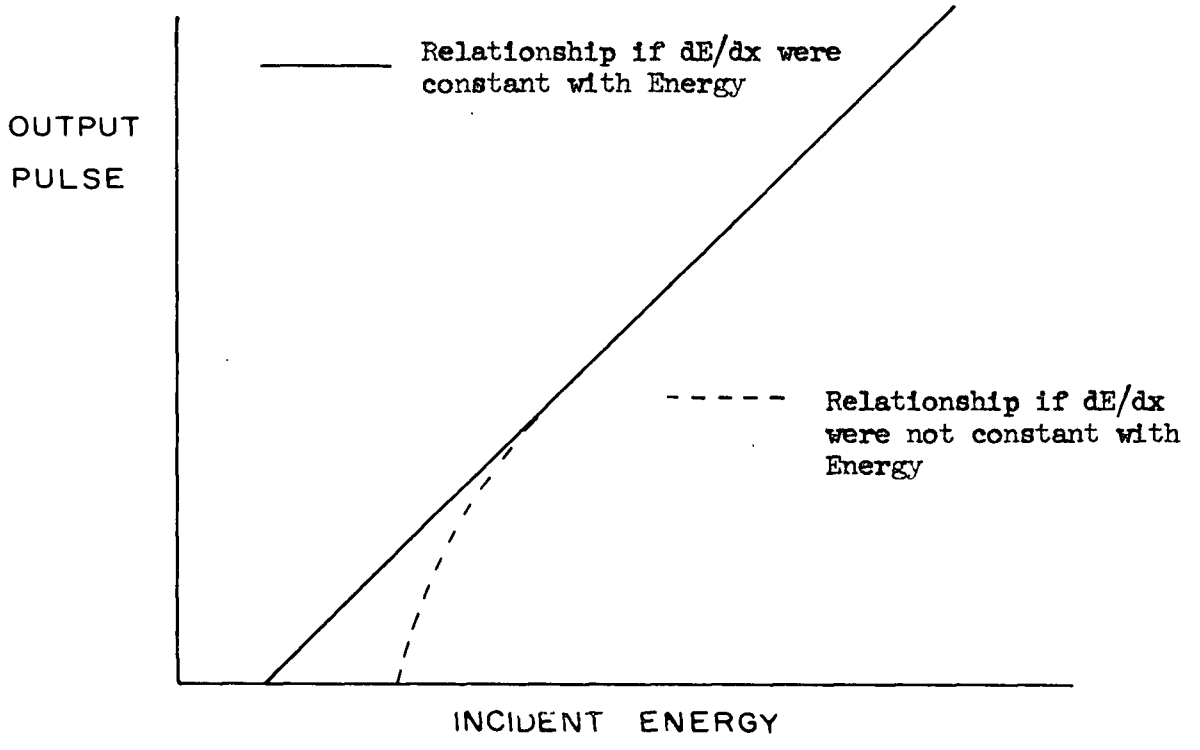

FIGURE 7: OUTPUT PULSE VS INCIDENT ENERGY

bute to the current immediately. This will occur every time a particle passes through the thin dead window in front of the charge-depleted region and every time a particle passes right through the region without losing all of its energy. These free holes and electrons will diffuse about in the field free region and may come to the edge of the charge-depleted region where one or the other type (depending on whether the region is in front of the active area or behind it) of carrier will be swept across. This second contribution to the current pulse caused by an incident charged particle, will occur much later after the main contribution from the active region, and will be much broader in time, (see Figure 6). Carriers in the field free region diffuse a distance given by:

$$L = \sqrt{Dt} \qquad (11)$$

in a time t, where D=ukT/q is the diffusion coefficient. The possibility of ever observing a carrier created outside the charge-depleted region depends upon the lifetime in the material, since the lifetime process is working to destroy the carriers that have been produced. In silicon D is 10 to 30 cm^2/sec so that in 10^{-7} sec. carriers will diffuse approximately 10^{-3} cm. Collection through diffusion is slow if it is to be used over significant distances, and because it requires long lifetimes for good collection efficiency, it is not a very useful way of extending the sensitive region of a junction particle detector.

The thickness of the charge-depleted region limits the energy range of the solid state device, but the "window thickness" of the surface layer may limit the linearity of the output pulse vs incident charged particle energy relationship. Because of the variation of the dE/dx for charged particles with energy, the dead window will cause low

FIGURE 8:

OUTPUT PULSE VS INCIDENT ENERGY:
RCA DEVICE WITH TWO DIFFERENT
WINDOW THICKNESSES

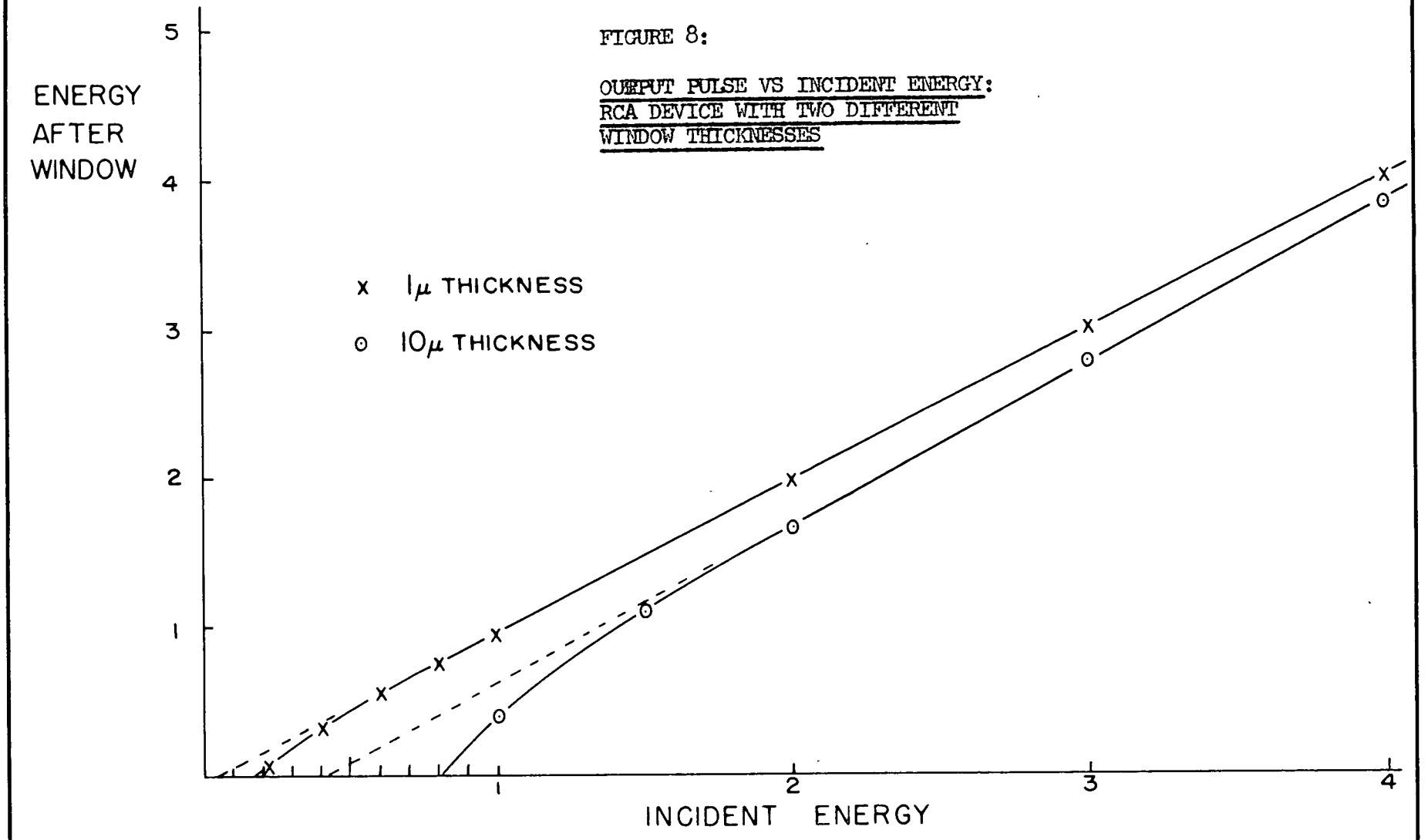

energy particles to lose more energy in passing through it than higher energy particles. This effect is shown in Figure 7. Figure 8 shows the possible effect on an RCA device with different dead window thicknesses.

The surface barrier detector (Dearnaley, 61) which works under the same principles as the diffused junction detector has the advantage that its dead window thickness is zero. Unfortunately, at the present level of development, its charge-depleted region is considerably thinner than a diffused junction region using the same resistivity silicon.

4. Noise in the Devices.

All junction devices have leakage currents under reverse bias that arise from several sources:

1. diffusion
2. space charge generation (Sah et al. 57)
3. surface effects. (Kingston, 56; Garrett et al. 56)

The first is a current due to the small equilibrium density of electrons in the p-type material. The electrons can diffuse to the charge-depleted region edge and contribute current. This is the normal reverse current found in all solid state diodes, and is of little importance in silicon devices at reasonably low bias voltages (50 volts or less for the old RCA type A and 75 volts for the new).

The second current is due to recombination centres in the charge-depleted region. Here the centres generate holes and electrons in succession at a rate depending upon the cross-sections and density of such centres and their location in the energy band

gap. The rate depends roughly upon inverse lifetime. This contribution can be very significant and it has a dependence on the junction bias because the number of centres inside the charge-depleted region increases with x.

The third current contribution is the most serious in most devices and is subject to change, as the surface chemistry at the edge of the junction changes with time and environment. It is, of course, not the current magnitude that matters but the fluctuations in the current, and it seems that the surface generated currents often contain much more than shot noise. The origin of the surface current is still open to some question, although a number of features seem explicable on models of junction leakage such as proposed by Kingston (54).

5. Variation of Signal Pulse with Reverse Bias.

If a voltage sensitive pre-amplifier is used in conjunction with the solid state device, the overall resolution of the system will be decreased, because of the effect the reverse bias has on the ouput voltage signal of the device. The signal pulse from the device, is:

$$V_s = \frac{Q}{C} \qquad (1)$$

where Q is the charge collected from the passage of a charged particle of energy E through the device. For Silicon:

$$Q = \frac{(E - E_w)1.6 \cdot 10^{-19}}{3.5} \qquad (2)$$

where E_w is the energy the particle loses in passing through the dead window of the device. C is the total output capacitance to the pre-amplifier. It includes the device capacitance C_d, and all the stray capacitances C_s. Normally C_d is much larger than

FIGURE 10a:

DETECTOR PULSE HEIGHT VS PROTON ENERGY

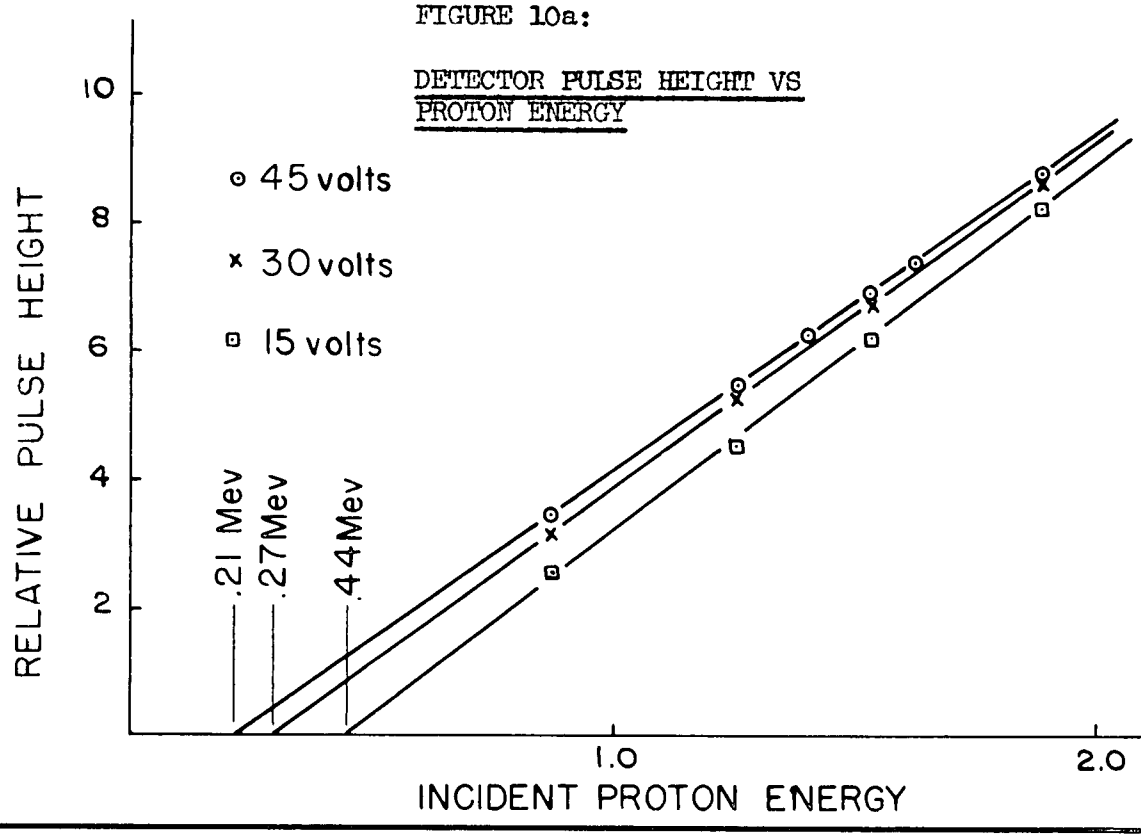

FIGURE 10b:

LINEARITY RANGE OF DETECTOR FOR PROTONS

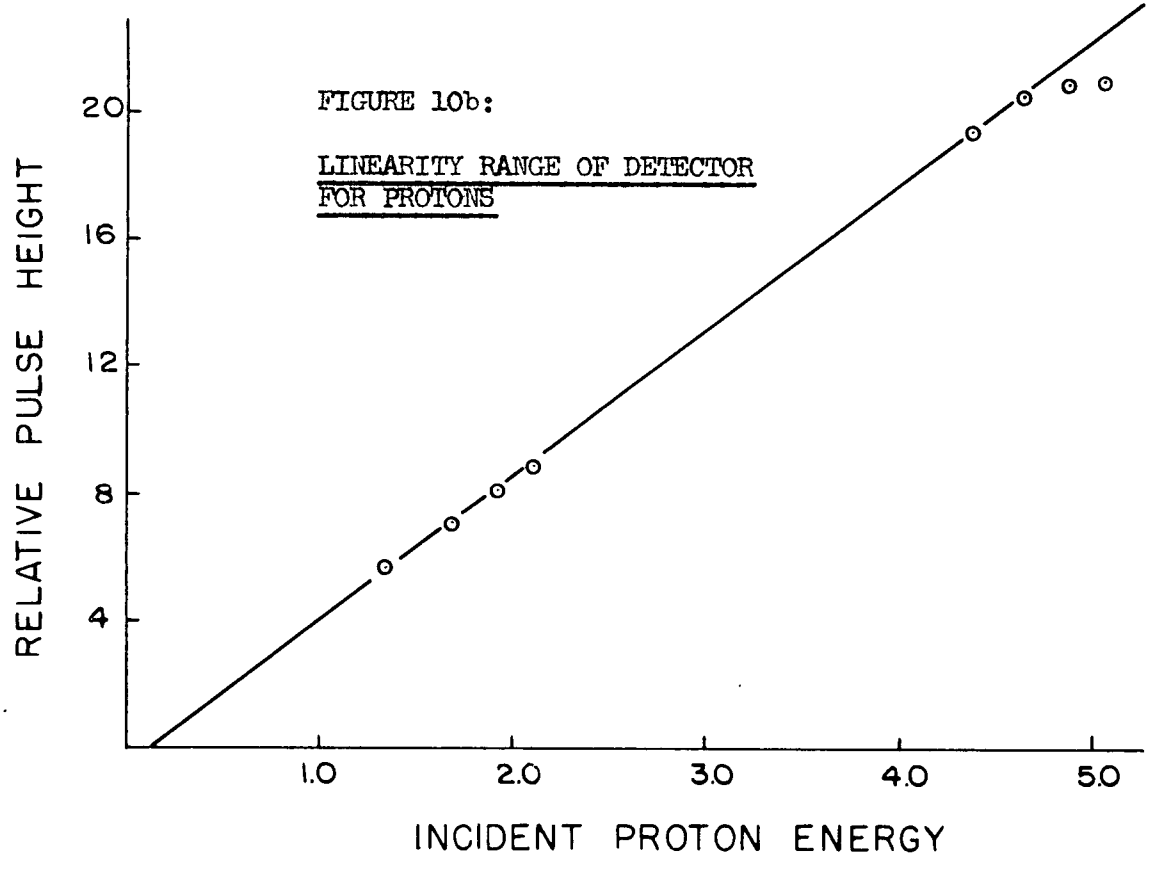

C_s , so for simplicity assume that $C = C_d$. From the parallel configuration of the charge-depleted region of the counter:

$$C_d = \frac{kA}{4\pi x} \qquad (3)$$

where A is the counter area, x is the charge-depleted region thickness and k is the dielectric constant of silicon $(13.32 \cdot 10^{-10}$ farads/meter)

From (1) and (3): $V_s \propto x$

But: $x \propto \sqrt{V_b + V_o}$

Therefore: $V_s \propto \sqrt{V_b + V_o}$

To avoid this situation, a charge sensitive pre-amplifier can be used. Then the output pulse from the pre-amplifier will be proportional to the total charge Q. Q is a slowly varying function of the bias voltage as the energy loss E_w in the device window changes with bias. However this effect is small compared to the change of V_s with respect to the reverse bias.

B. Characteristics of Solid State Devices.

Before using these devices for the detection of charged particles in an experment, several of their properties must be known. The more important ones are:

(i) the linearity of the output pulse vs the incident energy of the particle.

(ii) the range of particle energy over which the linearity holds.

(iii) the dead layer thickness. This determines the amount of energy an incident particle loses before it reaches the active region of the device.

(iv) the capacity of the device (the parallel plate configuration of the

FIGURE 11:

INCREASE OF DEVICE NOISE WITH NEUTRON FLUX

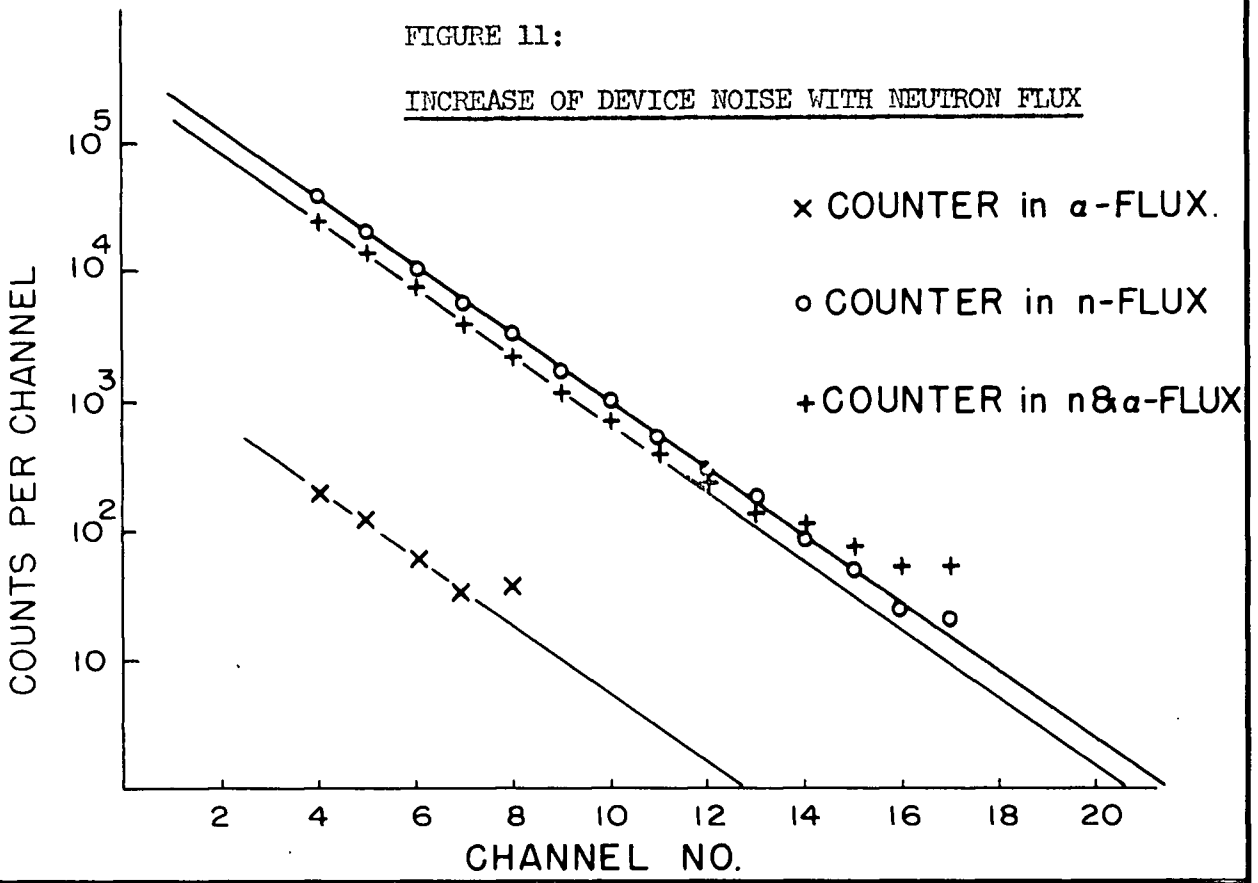

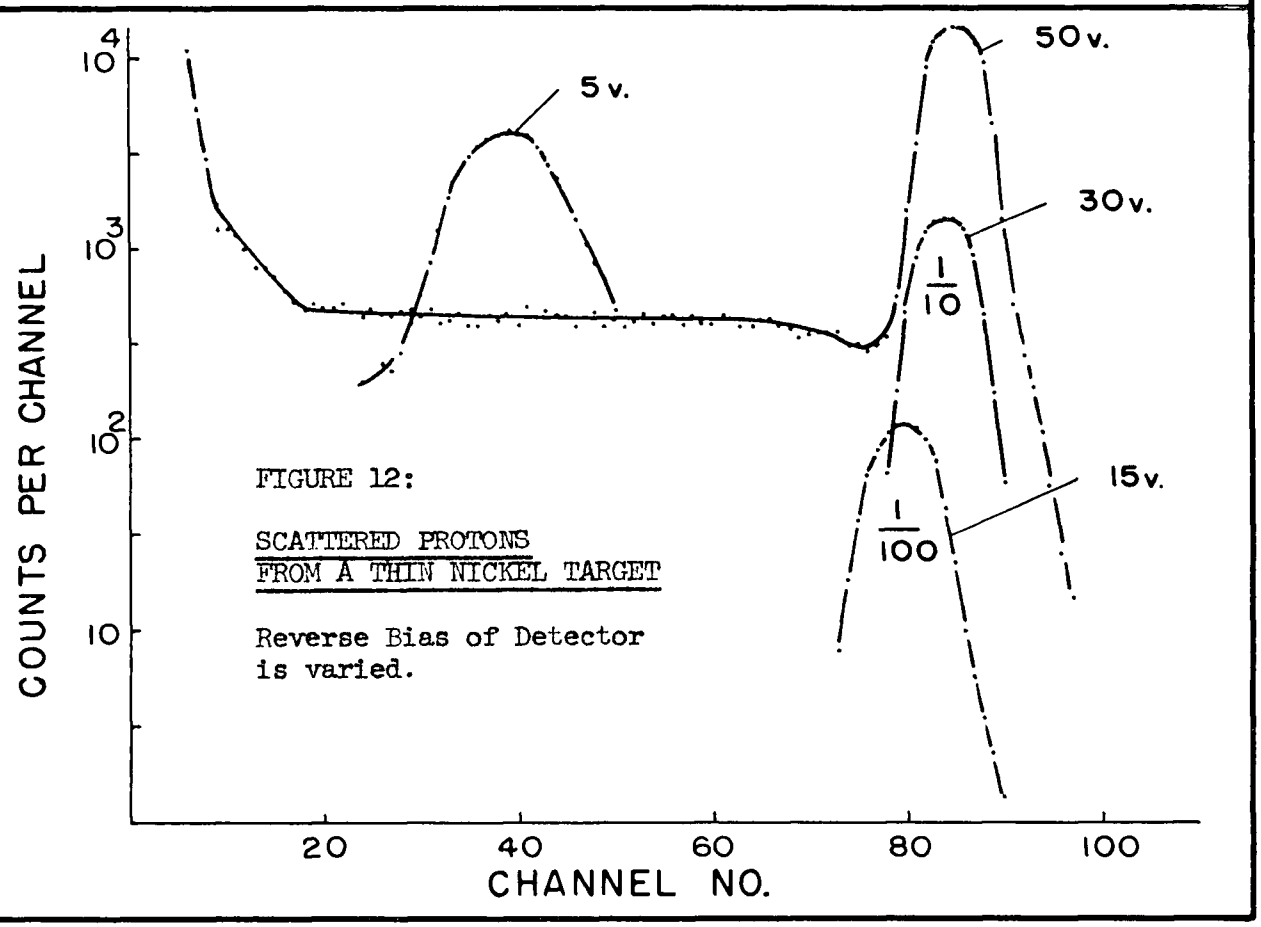

FIGURE 12:

SCATTERED PROTONS
FROM A THIN NICKEL TARGET

Reverse Bias of Detector
is varied.

charge-depleted region).

(v) the effective lifetime of the counter when it is subject to the radiation damage caused by any particle impinging on its surface.

For all experiments an RCA type A charged particle detector was used. A scale drawing of it and its mounting (as supplied by RCA) is shown in Figure 9. Figure 10a shows a plot of pulse height vs incident proton energy for one of these devices. The slight increase in the slope for the lower device bias voltages shows the effect of the change in the device capacitance. The increasing energy intercept with decreasing bias is caused by the increasing window thickness. The slopes and intercepts were calculated by the usual least squares method. The protons were obtained by scattering a beam on a thin Nickel film. A typical scattering spectrum is shown in Figure 12.

Figure 10b shows the range of linearity for protons. The high energy protons were obtained from the reactions $Be^9(d,p)Be^{10}$ (Q=4.59 Mev) and $Be^9(d,p)Be^{10'}$ (Q= 1.22 Mev). The proton peaks are identified in Figure 18 of Section IV-A. Estimating the dE/dx of the protons in silicon from Whaling (58), gives the thickness of the charge-depleted region as .16 mm at 60 volts reverse bias. This compares favourably with .115 mm at 40 volts bias, as calculated from the know pulse height and capacitance relationships shown in equations (1) and (3) of section II-A-5. These results were obtained using a different device than that used to look at the Be^9 reactions. Figure 13 shows the variation of the thickness of the charge-depleted region and of the capacitance with reverse bias, and also shows the thickness and capacitance values for the device used in the Be^9 reactions. For the calculations the stray capacitance of the wiring

FIGURE 13:

VARIATION OF CHARGE-DEPLETED REGION WITH REVERSE BIAS

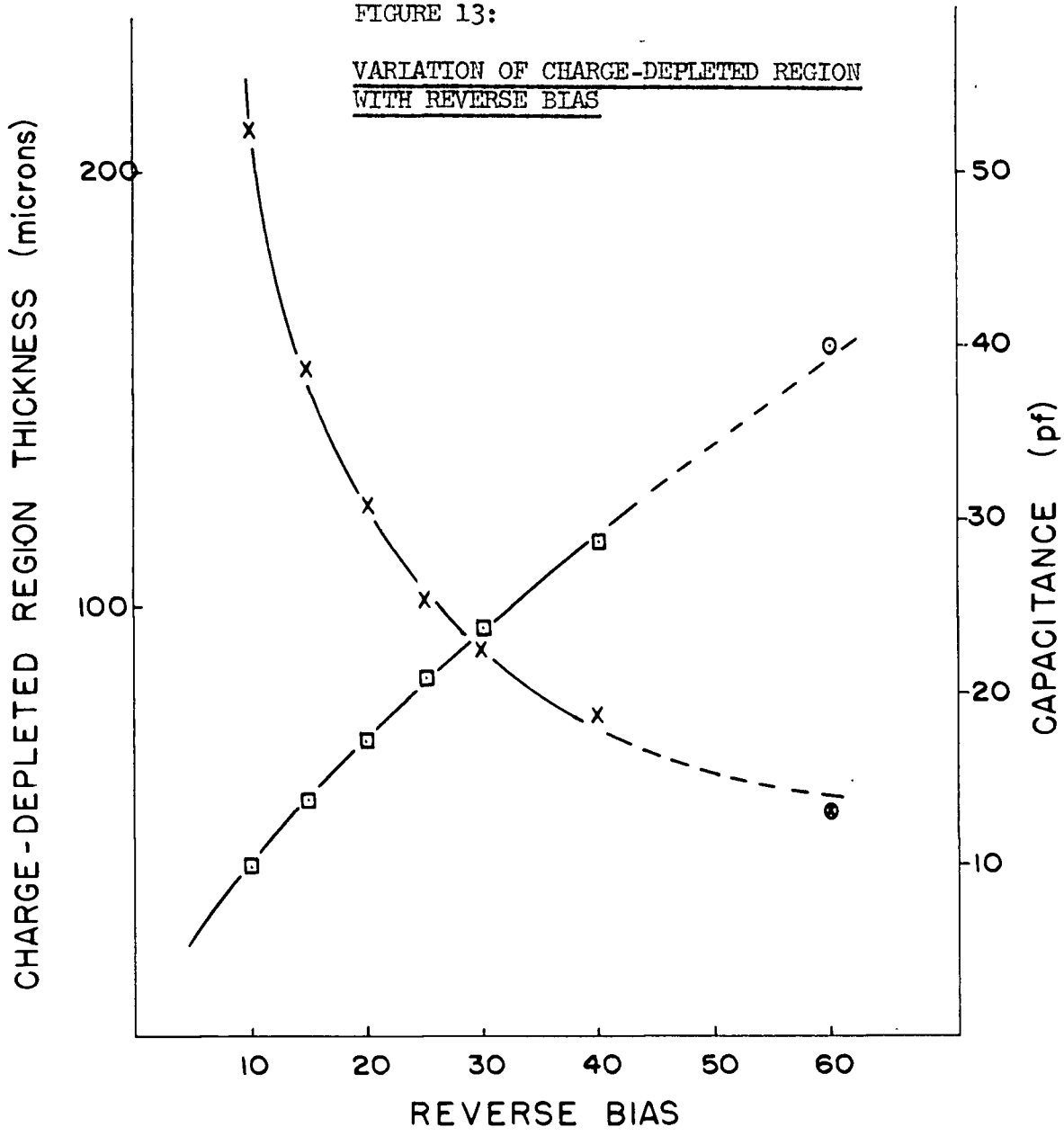

⊡	Region Thickness	Alpha Measurements
X	Region Capacitance	Alpha Measurements
⊙	Region Thickness	Proton Measurements
⊛	Region Capacitance	Proton Measurements

outside the device was assumed to be 5 pf. These measurements were done using a voltage sensitive pre-amplifier. Enumerated below are the counter characteristics for alphas, protons and tritons.

Counter Characteristics:

	Proton		Triton		Alpha	
Reverse Bias (volts)	60	10	60	10	60	10
Window loss (Mev)	.200	.450	-	.500	.750	.850
Maximum of Linearity Range (Mev)	4.60	2.60	-	4.00	-	8.00

These values will vary about 10% for different devices. The pulse-height vs incident energy curves for alphas and tritons is essentially the same as that for protons; the only difference being that caused by the fact that the dE/dx for alphas and tritons is larger, hence making the window thicker and the linearity range larger for the alphas and tritons.

Radiation damage is the limiting factor for the useful lifetime of a solid state device. According to Babcock, (61) the reverse current of the device increases about five-fold during an exposure to 10^{13} neutrons per cm^2. At this level of integrated neutron flux the device capacitance was found to increase by about 25%. A 1000 hour room temperature anneal restores about 50% of the change caused by this total irradiation. A neutron flux of $7X10^5$ per cm^2 per sec. was found to increase the counter noise by a factor of two while it was being used, as illustrated in Figure 11. The largest integrated flux of charged particles and neutrons reached by one device in this lab was 10^{10} per cm^2. This caused no measurable change in the proporties of the device.

Because of electronic considerations, the maximum counting rate allowable was about 10^5 counts/second. This corresponds to approximately $2x10^6$ particles per sec per cm^2. To reach a total integrated flux of 10^{13} particles per cm^2 means approximately 1400 hours of continuous running.

FIGURE 15

TARGET CHAMBER

SCALE: $\frac{1}{2}$ FULL SIZE

DETECTOR MOUNT

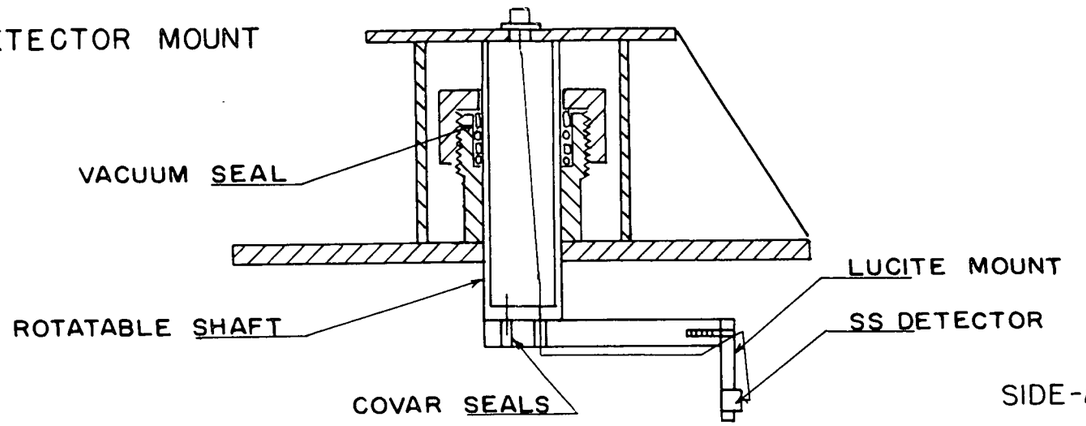

FARADAY CAGE ASSEMBLY

SIDE-ARM COUPLING

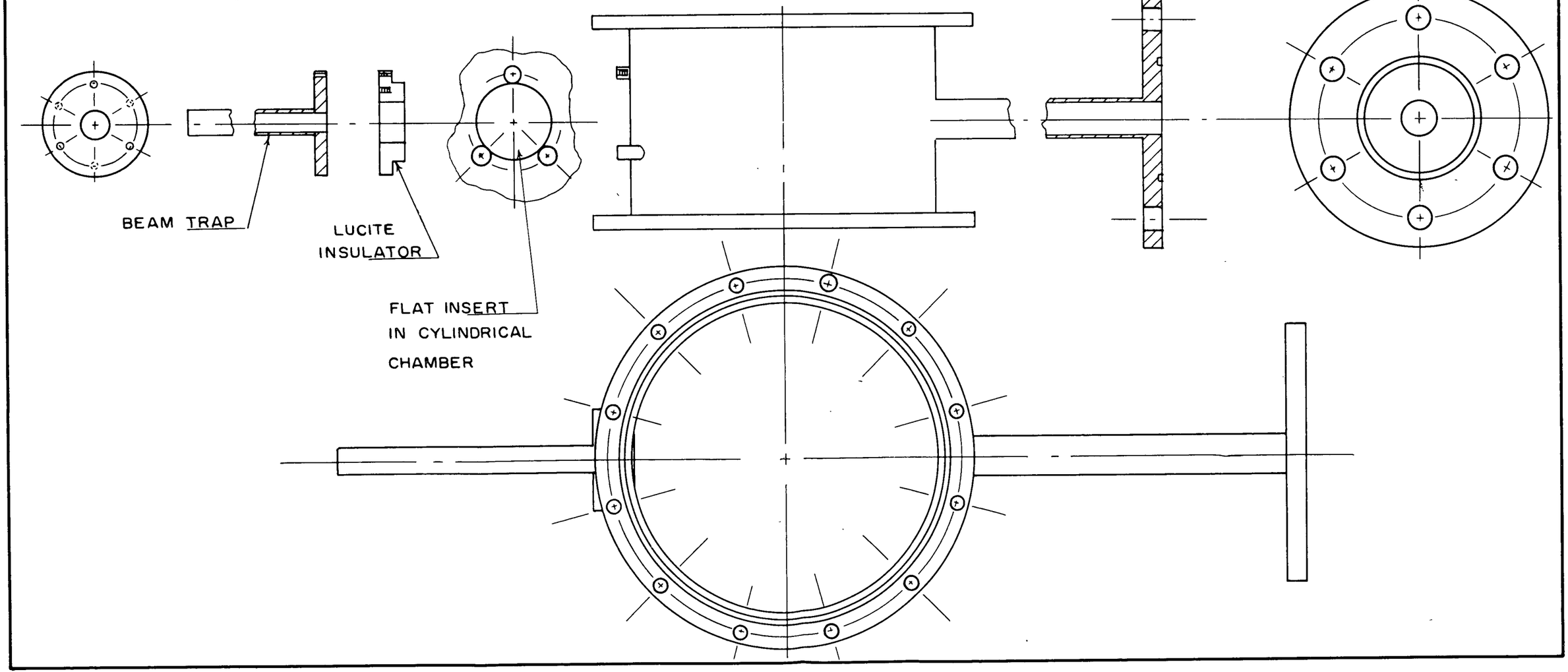

III. EXPERIMENTAL APPARATUS:

A schematic diagram of the experimental set-up is shown in Figure 14, and the target chamber in more detail in Figure 15.

The target chamber was designed so that the Solid State counter, mounted inside on a rotatable shaft, would subtend a small angle without making the overall chamber size too cumbersome. The RCA type A counter, used in the experiments, has a 5 mm^2 window area. This window has an angular width of 1.1 degrees and subtends a solid angle of 1.3 steradians at 6 cm from the target. The energy variation of a charged particle has a function of angle due to kinematical effects is much less than 1% (the approximate resolution of the counter) in the chosen geometrical arrangement. The general target and detector geometry is shown in Figure 16. The counter was mounted to a lucite holder with an epoxy resin (R-313), and was shielded with a copper strip which allowed particles, to enter the device window only when they came from the target areas. The counter holder is small enough to allow the beam to hit the target while the counter is sitting at a backward angle of 165 degrees. The central post has a vacuum seal that allows the counter to be rotated 360 degrees. The necessary electrical lead goes through one of the covar seals in the central post of the counter-mount assembly, and connects to an amphenol plug at the other end of the mount.

The counter bias supply and the pre-amplifier are mounted directly on the target chamber. The bias supply is a battery and potential divider, to vary the bias voltages. The pre-amplifier is a charge-sensitive type similar to that built by Higinbotham (61). The pulses from the pre-amplifier were fed directly to the main amplifier

of the Nuclear Data 256 Channel Pulse-height analyzer, which was used to record all the reaction spectra. A diagram of the bias supply and the pre-amplifier is shown in Figure 17. Section II-B gives a detailed description of the solid state counters used in these experiments.

TARGETS:

The Nickel targets, used for the proton scattering experiments to measure the solid state device characteristics, were obtained from Chromium Corporation of America.

The Beryllium targets were made by the evaporation of Be metal on a formvar film backing. All evaporations were done in vacuums of 10^{-5} mm Hg or less. The Beryllium was evaporated onto the Formvar until the white-hot Tantalum boat, containing the melted Beryllium was no longer visible through the film. Stopping the evaporation at this point gave a layer of Beryllium approximately 5000 Å thick. Attempts were made to remove the formvar backing from the Beryllium by bathing the target in an atmosphere of Trichlorethylene. However, all attempts at removal were unsuccessful, so the Carbon contamination from the formvar had to be taken into consideration.

FIGURE 18

REACTION PRODUCTS DEUTERON ON Be^9

E_d = .500 Mev at 160°

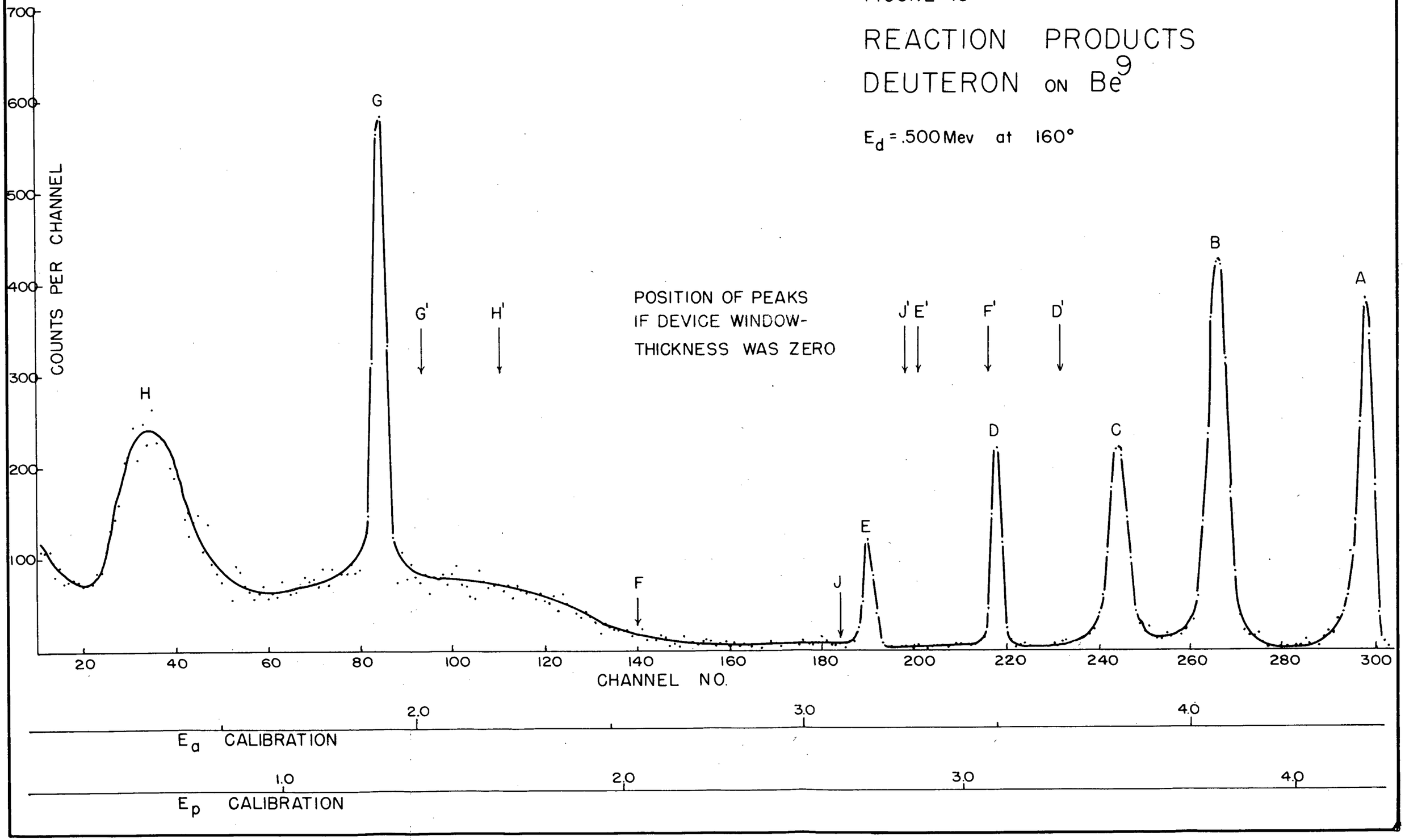

IV RESULTS:

A. Introduction:

The following reactions from Be^9 were observed and studied:

(1.) $Be^9(d,a)Li^7$: The angular distributions of the alpha decay to the ground state and first excited state of Li^7 were studied in detail at deuteron energies of .5 to 1.35 Mev, and the angular distribution of the alpha decay to the 4.5 Mev excited state of Li^7 was measured at a deuteron energy of .500 Mev. This 4.63 Mev state was first discovered by Gove and Harvey (51), and also noted soon after by Gelinas et al. (51) and Ashmore and Raffle (52). An alpha group to an excited state at approximately 5.5 Mev in Li^7 was looked for at deuteron energies from .5 to 1.00 Mev.

(2.) $Be^9(d,t)Be^8$: the angular distribution of the triton decay to the ground state of Be^8 was studied at deuteron energies of .5 to 1.35 Mev.

(3.) $Be^9(d,a)Li^{7''}$, (t)a:

$Be^9(d,t)Be^{8'}$, (a)a: the wide continuum of charged particles from these reactions due to the short lifetime of the $Li^{7''}$ and $Be^{8'}$ nuclei was noted and compared with the findings of Gelinas and Hanna (53) and Jung and Cüer (56).

(4.) $Be^9(d,p)Be^{10}$: the peaks corresponding to the proton to the ground state and first excited state of Be^{10} were noted. Several reactions from target impurities were noted:

(i) $C^{12}(d,p)C^{13}$, $C^{13'}$

(ii) $C^{13}(d,a)B^{11'}$, $B^{11''}$

(iii) $C^{13}(d,t)C^{12}$

(iv) $O^{16}(d,a)N^{14}$, $N^{14'}$

(v) $O^{16}(d,p)O^{17}$, $O^{17'}$

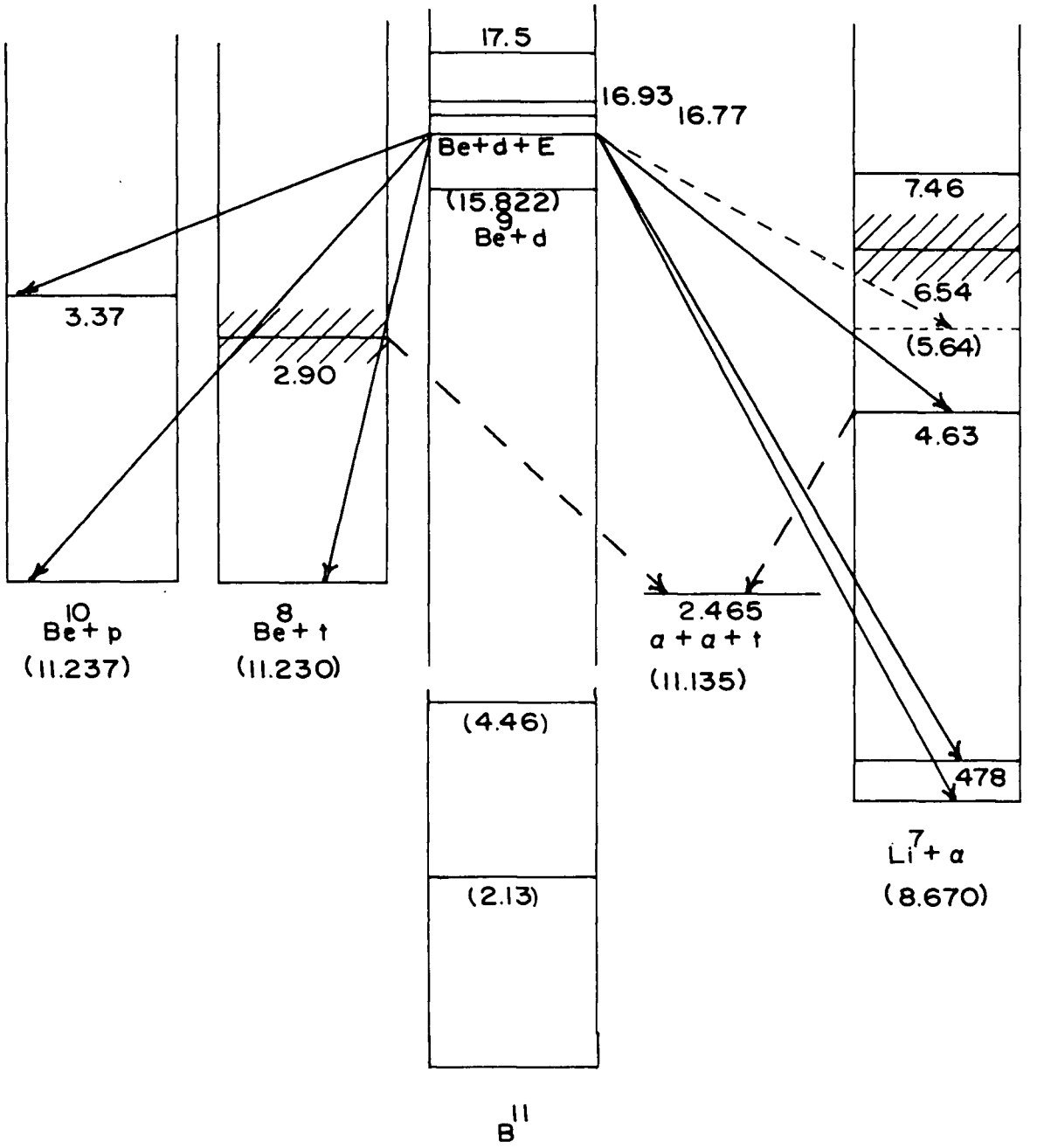

FIGURE 19:

TRANSISTIONS NOTED IN THIS EXPERIMENT

Typical spectra of the reaction products, as detected by the charged particle detector are shown in Figures 18, 20, 21 and 22.

Figure 18 shows the complete spectrum of reaction products above the scattered deuterons at an angle of 160 degrees with respect to the incident deuteron beam of .500 Mev energy. As an aid to identifying the peaks with their corresponding transitions refer to Figure 19, where all the transition, except one, found in this spectrum are marked. Starting from the high energy side of the spectrum:

A: is the proton to the ground state of Be^{10} in the reaction $Be^{9}(d,p)Be^{10}$.

B: is the alpha particle to the ground state of Li^{7} in the reaction $Be^{9}(d,a)Li^{7}$.

C: is the alpha particle to the first excited state of Li^{7}.

D: is the triton to the ground state of Be^{8} in the reaction $Be^{9}(d,t)Be^{8}$.

E: is the proton to the ground state of C^{13} in the reaction $C^{12}(d,p)C^{13}$. (This transition is not shown in Figure 19).

F: is the highest possible energy of the alpha particles from the secondary emission of alphas from the excited states in Be^{8} and Li^{7}. In Appendix I, an analysis is done on the possible energy range of these particles.

J; is the highest energy of the tritons from the secondary emission of the excited states in Li^{7}.

G: is the proton to the first excited state in Be^{10}.

H: is the alpha particle to the second excited state in Li^{7}.

Because of the different energy losses for alphas, tritons etc., in the device window, the channel numbers on this and subsequent spectra do not correspond to the

FIGURE 20:

HIGH ENERGY EMISSION PRODUCTS

E_d: 1.35 Mev at 160 degrees

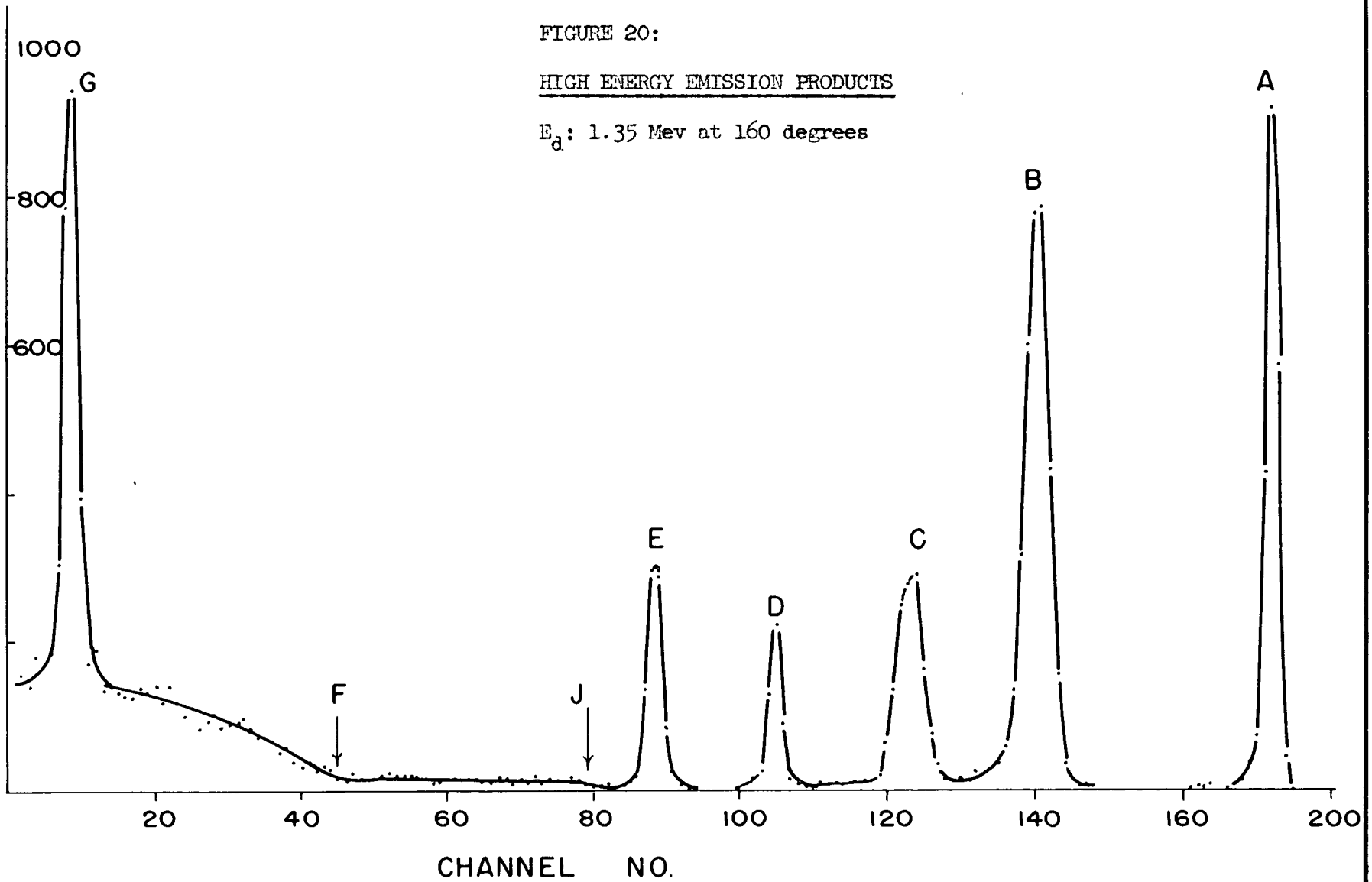

same energy calibration for the different particles. Each particle has its own calibration as shown by the different scales in Figure 18. The arrows on Figure 18 correspond to the positions where the peaks would occur if the solid state device had no window.

All energy vs channel calibrations were made using the fact that the reaction product energies change with the angle of emission. For an incident deuteron energy of 1 Mev, the energy of the alpha particle to the ground state of Li^7 is 4.02 Mev at an emission angle of 165 degrees with respect to the beam direction and 6.11 Mev at 30 degrees with respect to the beam direction. The energy variation for tritons, deuterons, and protons is not as much, but it is still sufficient to obtain a reasonable calibration curve that enables other energies to be measured with 5% accuracy.

Figures 20, 21 and 22 show the effect of the emission angle on the high energy end of the reaction product spectrum. The bombarding deuteron energy is 1.35 Mev. Figure 20 shows the emission products at 160 degrees and Figure 21 at 120 degrees. Several reaction and kinematical effects can easily be seen in Figures 20 and 21. They are:

(i) the energies of the alpha particles to the ground and first excited state of Li^7 change much more rapidly with the angle than does the energy of the proton to the ground state of Be^{10} and the energy of the triton to the ground state of Be^8. This effect can be noted by the relative change in position of the peaks in Figures 20 and 21.

(ii) the reaction cross-section changes as a function of the angle as can be seen by the change in the peak heights between figures. The integrated beam of deuterons is the same for all these spectra (40 microcoul.)

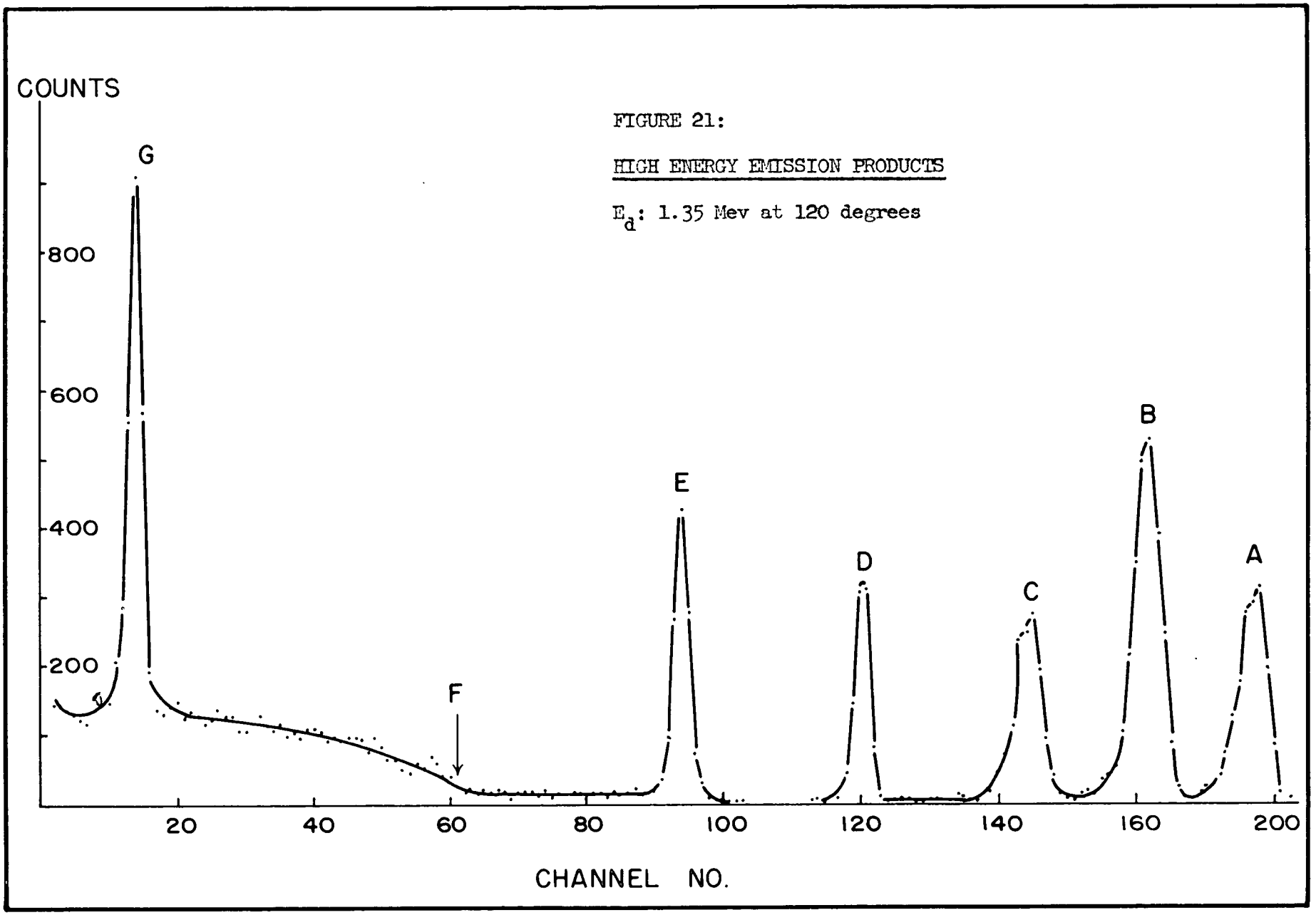

FIGURE 21:

HIGH ENERGY EMISSION PRODUCTS

E_d: 1.35 Mev at 120 degrees

The highest energy proton peak (A) in Figure 21 shows a distinct broadening and assymetric effect from that in Figure 20. At 120 degrees, these protons have enought energy to pass right through the charge-depleted region of the solid state device at a reverse bias of 60 volts. The straggling effect on the peak is caused by the non-uniformity of the charge-depleted region thickness. In order to further study the reaction spectrum at lower angles this broad proton peak had to be shifted from the interesting part of the spectrum. This was done by decreasing the reverse bias of the devices by a factor of 4; hence decreasing the charge-depleted region thickness by approximately a factor 2. This thickness still stops a high energy alpha or triton, but the proton now loses only about half of its energy in the charge-depleted region: hence the peak (A) corresponding to protons from $Be^{9}(d,p)Be^{10}$ is shifted far to the left in the spectrum as shown in Figure 22. With a reverse bias of 15 volts, the charge-depleted region is still thick enough to stop approximately 10 Mev alpha particles.

B. The $Be^{9}(d,a)Li^{7}$ Reaction:

The angular distributions of the alpha particle transition to the ground (a_1) and first (a_2) excited state of Li^{7} were measured at deuteron energies of .500, .750, 1.00, 1.16, and 1.35 Mev, using two targets of Be^{9} on Formvar. These distributions are shown in Figures 23, 24, 25, 26 and 27. The distributions at .500, .750 and 1.00 Mev were taken with the same target.

As can be seen from Figure 16, reaction products from 90 to 165 degrees were measured from the beam entrance side of the target, and products from 90 to 15 degrees

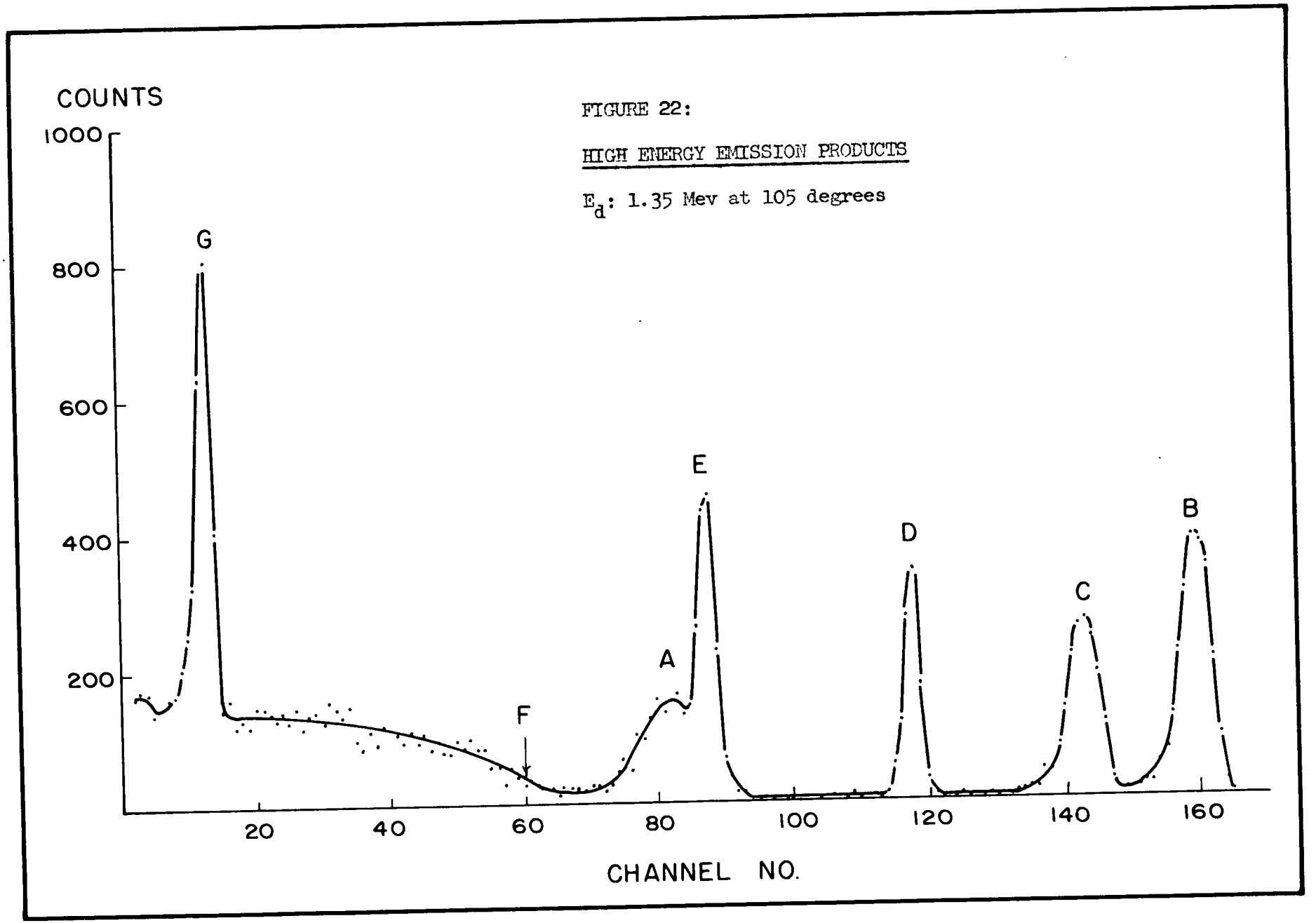

FIGURE 22:

HIGH ENERGY EMISSION PRODUCTS

E_d: 1.35 Mev at 105 degrees

were measured from the beam exit side of the target. To change the counter from a position of 95 degrees with respect to the beam direction to 80 degrees, required a rather long angular movement. This movement could easily have caused the whole target chamber to be moved lightly, thus moving the position where the beam would hit the target. Since the target does not have a uniform thickness of Be^9, the reaction yield could easily change. This effect was thought to have caused the small peak near 90 degrees in the distribution of a_2 at energies of .500, 1.16 and 1.35 Mev. So further measurements were made at 1.16 and 1.35 Mev, making sure the chamber did not move and using a target of more uniform thickness. These distributions are shown in Figures 28 and 29. The small peak at 90 degrees in the a_2 distribution still remains after these precautions, but the distributions of a_1 shows a minimum near 60 degrees indicating that the target may have shifted for the previous measurements.

The absolute cross-section for these reactions cannot be accurately determined with these results because of the uncertainty of the target thickness measurements. However the cross-section for the reaction is estimated to be between one and five mb/steradian.

Figure 30a shows the fraction of the alphas from $Be^9(d,a)Li^7$, Li^7, which go to the first excited state at an emission angle of 90 degrees in the lab coordinates. These results are in good agreement with those reported by Gelinas and Hanna (53).

The angular distribution of the alpha particles to the second (a_3) excited state in Li^7 was measured for a deuteron energy of .500 Mev. This distribution is shown in Figure 30b. The larger absolute errors in these measurements occur because the alpha

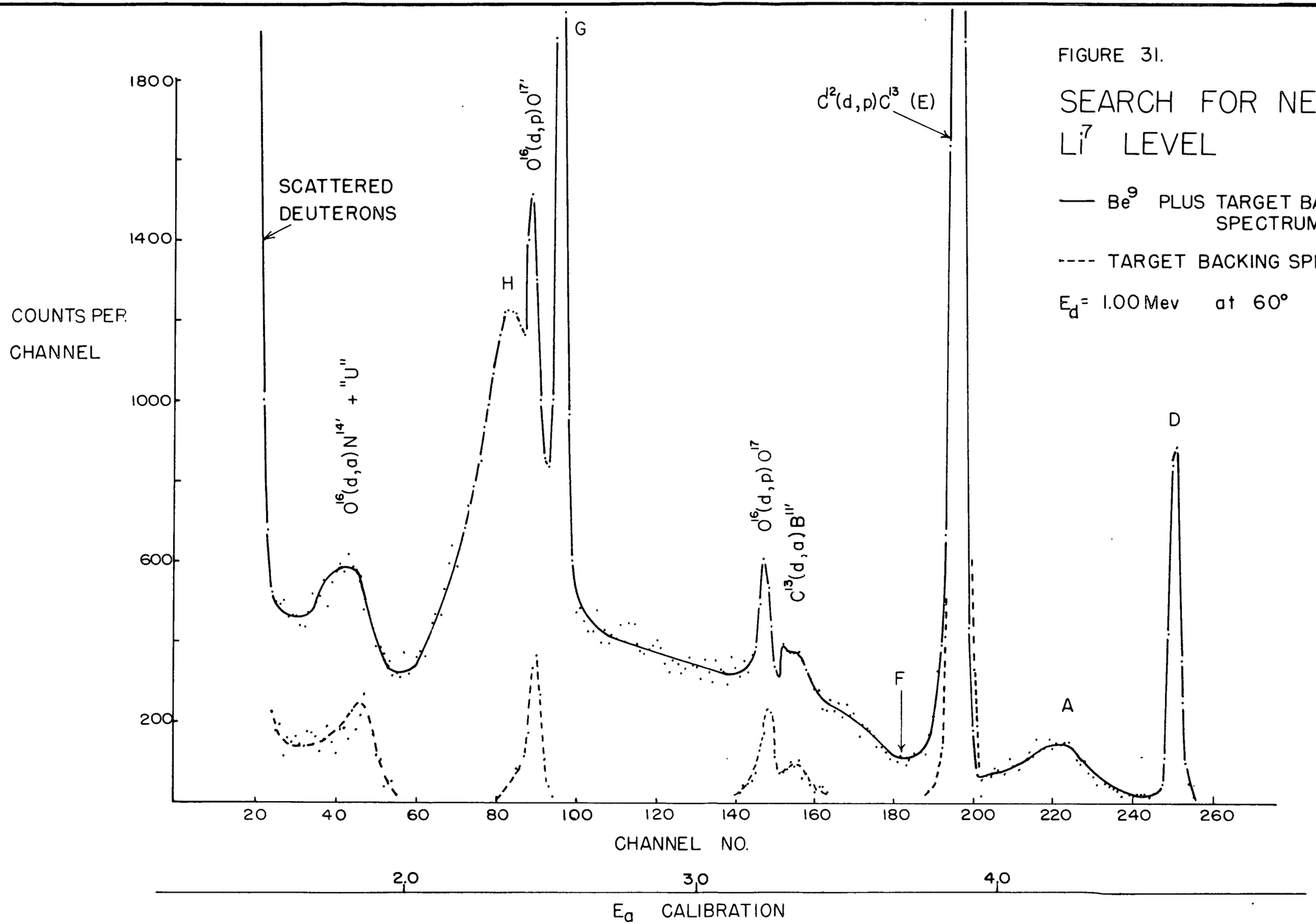

FIGURE 31.

SEARCH FOR NEW Li^7 LEVEL

—— Be^9 PLUS TARGET BACKING SPECTRUM

---- TARGET BACKING SPECTRUM

E_d = 1.00 Mev at 60°

spectrum was super-imposed on the continuum of secondary emission particles. The width of the second excited state was measured from the width of the alpha peak in the spectrum and was found to be 130 ± 30 Kev, as compared with the value of 93 ± 8 Kev obtained by Browne (57).

An alpha transition to a level around 5.5 Mev was looked for at several energies (.500 to 1.35 Mev) and several angles. Because the target was not pure Be^9 as shown from the elastically scattered proton spectrum (Figure 35), no peak can be positively identified as the looked-for transition. However, by subtracting a spectrum of reaction products of the target backing from a spectrum of reaction products of Be^9 plus target backing a fairly reliable spectrum of reaction products from only Be^9 can be produced. Figure 31 is the spectrum from Be^9 plus target backing and the spectrum from the target backing at an angle of 60 degrees and a deuteron energy of 1.00 Mev. Figure 32 shows the subtraction of the two spectra. The peak marked by "U" corresponds to that of 1.76 Mev alpha particle. This corresponds to an excited state of 5.64 ± .11 Mev in the Li^7 nucleus. Other indications of this transition showed up at forward angles of 50 to 75 degrees and at energies of .700 to 1.00 Mev.

No positive indication of a transition to a level near 6.5 Mev in Li^7 was found. A peak corresponding to an alpha transition to this state would be hidden in the scattered deuteron peaks from the target, because of the window thickness of the device. There is, however, another way of testing whether this 6.5 Mev excited state exists. That is by looking for its break-up into a triton and an alpha particle. The maximum possible energies of an alpha particle from the 2.90 Mev excited state in Be^8 and the 4.63 Mev

FIGURE 32.

SEARCH FOR NEW Li^7 LEVEL

DIFFERENCE OF THE TWO SPECTRA IN FIGURE 31.

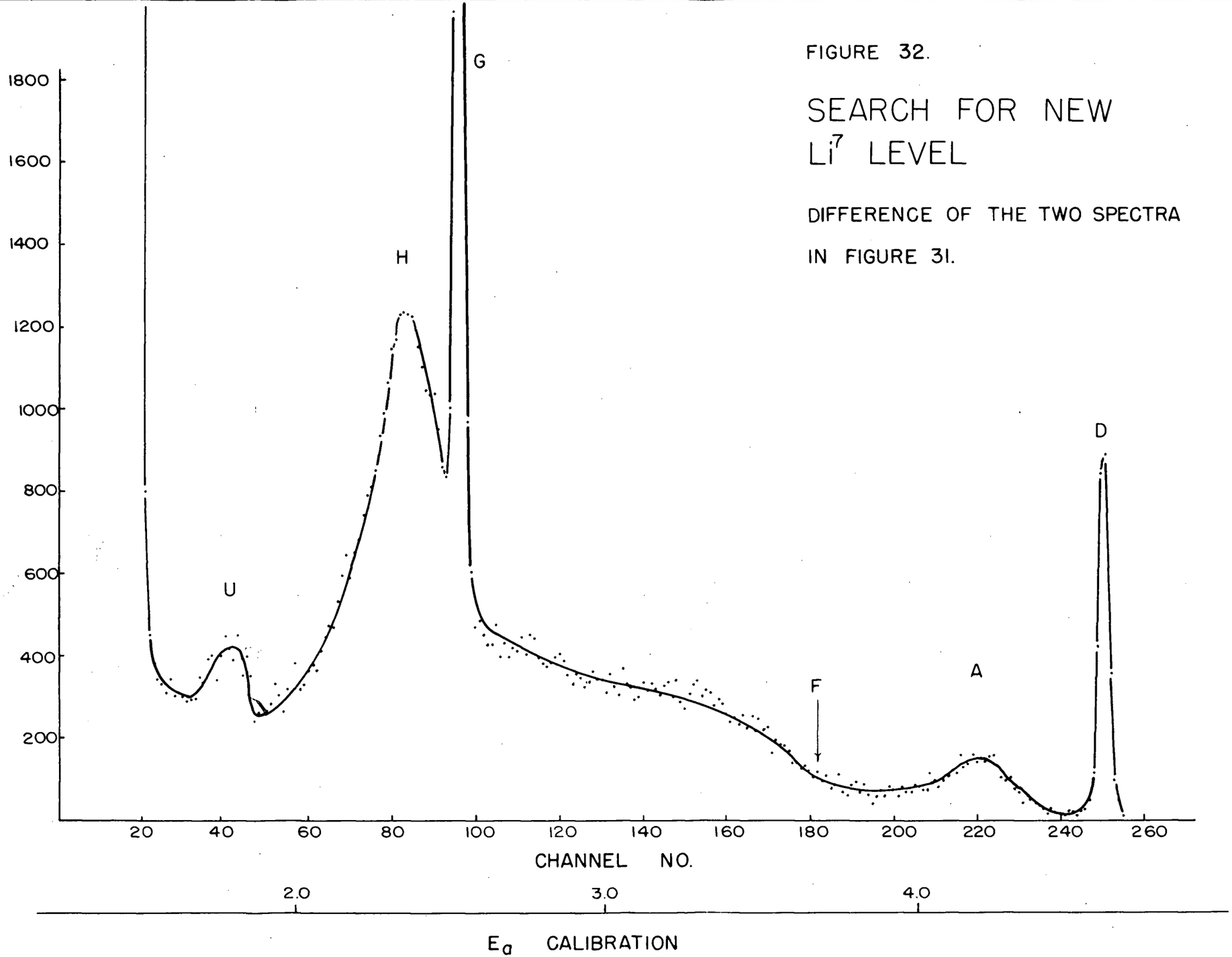

and 6.5 Mev excited states in Li^7 have been calculated in Appendix 1. Figure 33 shows a graph of the calculated maximum energies as a function of the emission angle, for a deuteron bombarding energy of 1.35 Mev. The experimental points on the figure show the measured maximum energy of the alpha continuum for a 1.35 Mev deuteron beam. As can be seen, there is no indication of an alpha particle from the 6.5 Mev state in Li^7. A similar check on the maximum triton energy from these excited states of Li^7 could not be done because the proton peak from the $C^{12}(d,p)C^{13}$ reaction obscured the end of the triton continuum. Jung and Cüer (56) have done this check on the maximum triton energy. Their results indicate a triton from a level at 6.6 Mev in Li^7.

C. The $Be^9(d,t)Be^8$ Reaction:

The angular distribution of the triton transition to the ground state of Be^8 was measured at deuteron energies of .50, 1.16 and 1.35 Mev, as shown in figure 34. These distributions are in good agreement with those reported by: Smither (57) and Haffner (56).

D. Target thickness and Impurities.

The thickness of the Be^9 target was measured by looking at the spectrum of elastically scattered protons from the target. Figure 35 shows the scattered spectrum at 155 degrees with respect to the proton beam of 1.600 Mev. The integrated proton beam was 6.3 microcoul. As shown on the figure, the lowest energy peak is that from scattering on Be^9 nuclei, the middle peak is from scattering on C^{12} nuclei and the high energy peak is from scattering from O^{16}. The target thickness was measured by two independent methods:

(i) calculating the target thickness from the Rutherford Scattering formula,

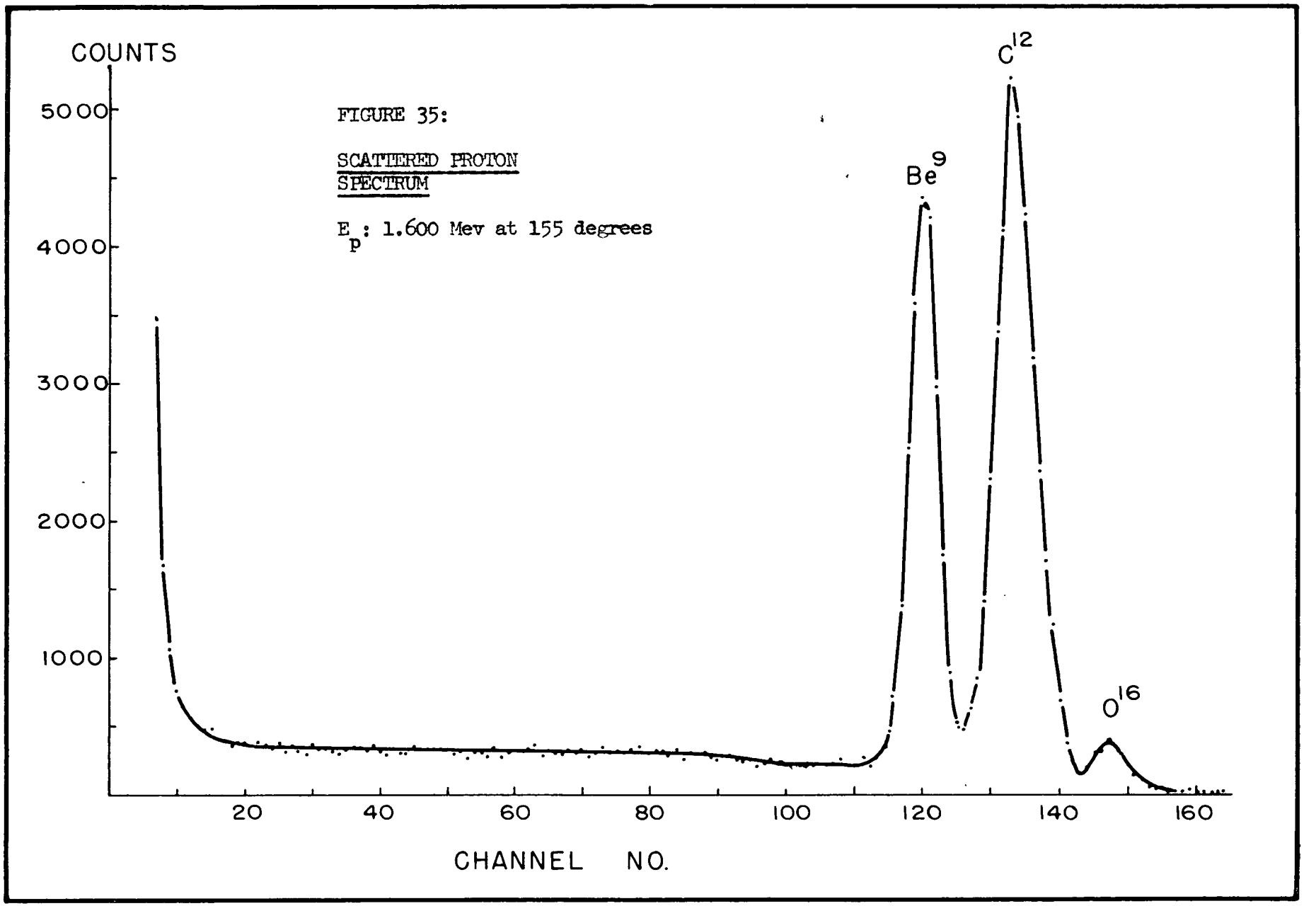

FIGURE 35:

SCATTERED PROTON SPECTRUM

E_p: 1.600 Mev at 155 degrees

after integrating the counts in the Be^9 peak.

(ii) measuring the width of the scattered proton peak from Be^9 and calculating the thickness from the know dE/dx for protons in Be^9. The thickness as measured using the Rutherford formula and the integrated proton flux was about 3 times higher than that measured by the known dE/dx values. This discrepancy may be due to inaccuracy in measuring the beam current passing through the target. The target was at ground potential; hence any electrons knocked out of the target by the impinging protons and in the direction of the proton beam would be collected by the Faraday Cage. These electrons would cause the current reading to be lower than the true beam current. Hence the integrated beam value would be lower than the true value and the resulting target thickness calculation would be higher than the true value. Any absolute cross-section measurement can only be estimated within a factor of 3.

The impurities in the target were more easily determined by looking at the scattered deuteron spectrum. Figure 36 shows the elastically scattered spectrum plus three low energy reaction products at 75 degrees with respect to the 1.35 Mev deuteron beam. By checking the energy variation of the scattered deuterons from C^{12}, N^{14}, and 0^{16}, the C^{12} and 0^{16} impurities were identified. The reaction products shown in Figure 36 are:

M: an alpha transition to the first excited state in N^{14}, from the reaction $0^{16}(d,a)N^{14*}$.

N: an alpha transition to the second excited state in B^{11} from the reaction $C^{13}(d,a)B^{11**}$.

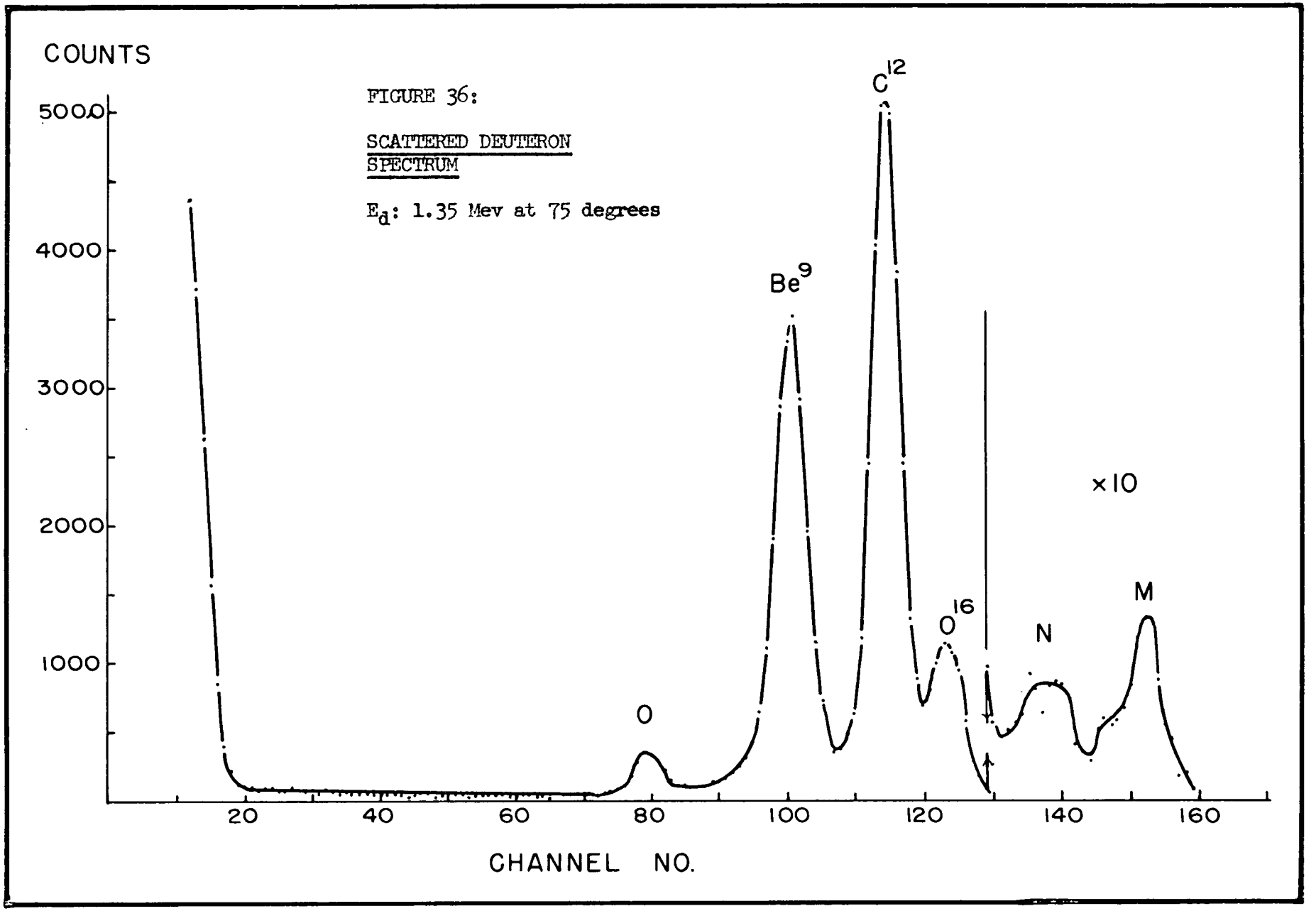

FIGURE 36:

SCATTERED DEUTERON SPECTRUM

E_d: 1.35 Mev at 75 degrees

O: a proton to the first excited state of C^{13} in the reaction $C^{12}(d,p)C^{13*}$.

Figure 37 shows the low energy spectrum at an angle of 45 degrees with respect to the 1.35 Mev deuteron beam. The large peak marked "P" is the recoil protons from the deuterons hitting the hydorgen in the formvar backing. Figure 38 shows the spectrum of low energy products at 45 degrees with respect to the 1.35 Mev deuteron beam for a formvar target only. The reaction products due to the Oxygen contaminants are not present in this spectrum, thus suggesting that the oxygen on the targets may have been picked up during the evaporation of the Beryllium.

V. CONCLUSIONS:

The solid state charged particle detector has proved itself to be an invaluable tool for studying low energy nuclear reactions. Because of its small size it can be used for studying the angular distributions of reaction products. Because of the fast rise-time of its signal pulse(10^{-8} sec), it can be used to study particle-gamma ray correlations and particle-particle correlations. Because of its good resolution, it can resolve the elastically scattered particles from different nuclei, making it an excellent device for target thickness measurements. Because of the devices 100% efficiency in detecting charged particles care must be taken to keep the flux of charged particles incident on the device below 10^{5} per second. Any higher count rate would tend to swamp the electronics.

This study of the Be^{9}(d,a) Li^{7} reaction has yielded several interesting results and has indicated further experiments that should be run on this reaction.

The angular distribution to the ground and first excited states of Li^{7} have been fairly well established between the deuteron energy of .5 and 1.35 Mev. Unfortunately the absolute cross-section for the reaction could only be estimated to be between one and five mb/steradian. A further study of the reaction cross-section of these two transitions, as a function of energy would be of interest, to help determine whether there is compound nucleus formation during the reaction.

The indication of an alpha transition to a 5.64 $\pm$ .11 Mev excited state in Li^{7} is weak, because of the reactions with the target impurities. To check the validity of this indication, the reaction must either be run using a pure Be^{9} target, or be run using

a magnetic spectrometer.

The fact that the maximum energies of the alpha contiuum do not indicate an excited level near 6.5 Mev in Li^7 does not mean this level does not exist. It does mean, however, that the cross-section for populating this level is considerably lower than the cross-section for populating the 4.63 Mev excited level in Li^7. An excellent way of studying these excited states of Li^7 that break up into a triton and an alpha particle would be to run an alpha-triton or alpha-alpha correlation experiment.

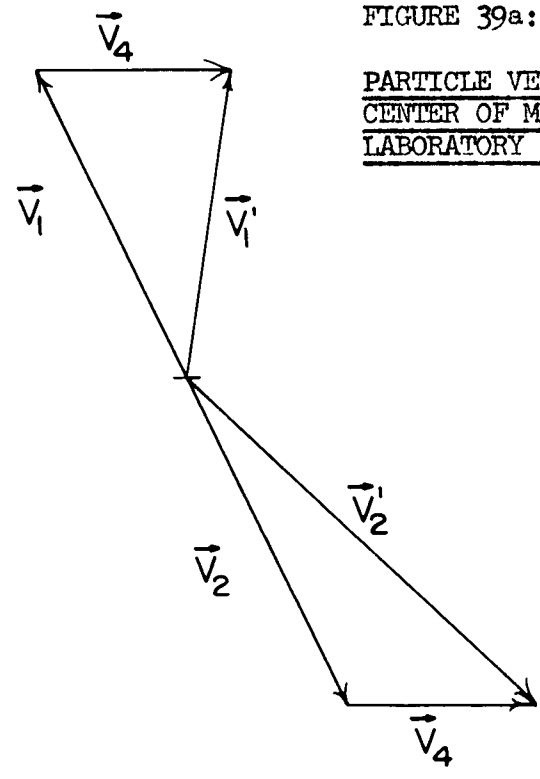

FIGURE 39a:

PARTICLE VELOCITIES IN CENTER OF MASS AND LABORATORY COORDINATES

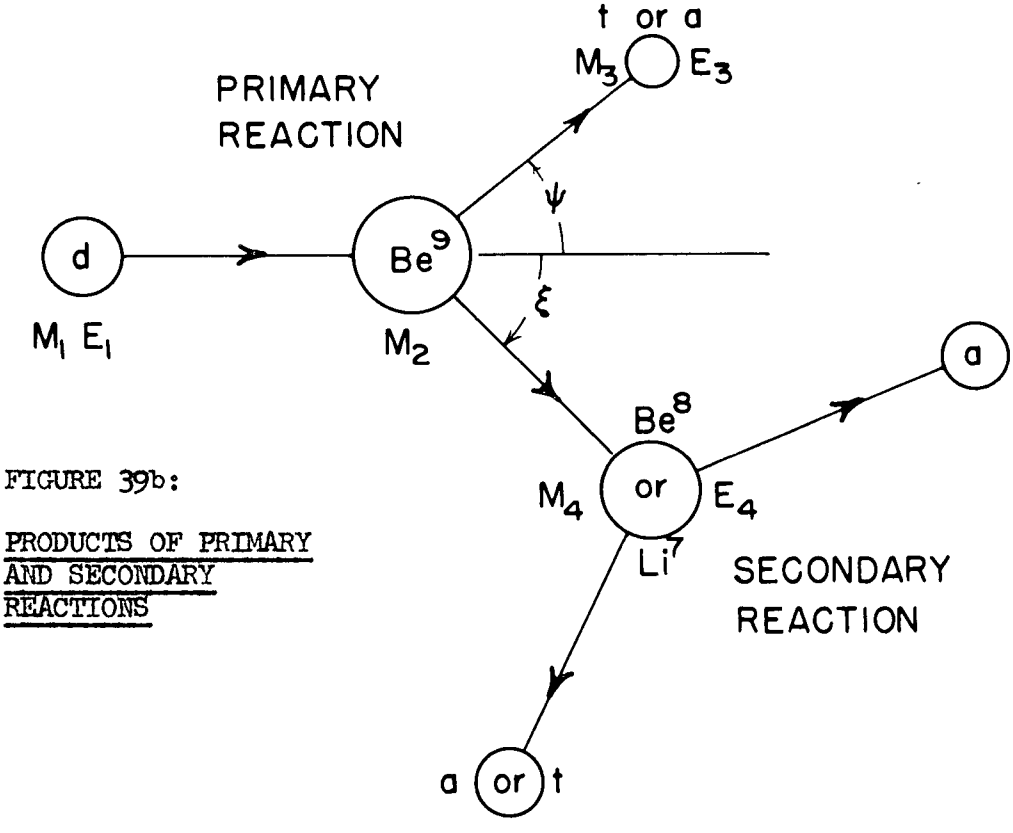

FIGURE 39b:

PRODUCTS OF PRIMARY AND SECONDARY REACTIONS

APPENDIX I

Secondary break-up of $Li^{7''}$ and $Be^{8'}$.

The secondary emission studied in this Appendix is the particle break-up of the:

(i) first (2.90 Mev) excited state of Be^8 into two alpha particles:

(ii) second (4.63 Mev) and third (6.54 Mev) excited states of Li^7 into an alpha and a triton. These transitions are shown in Figure 19. In calculating the possible range of energies for these particles, it is assumed that the parent nucleus has not lost any of the recoil energy it received rom the initial reaction $Be^9(d,t)Be^{8'}$ or $Be^9(d,a)\ Li^{7''}$, $Li^{7'''}$. If the excited nucleus was at rest before the secondary emission occured the energy of the secondary particles would be single-valued. As can be seen from the spectra in figures 18 - 22 the energy is far from being single-valued. Therefore, the assumption that the excited nucleus has lost little of its recoil energy is, at least to a first order approximation, a good one.

The lab energy of the excited nucleus from the primary transition is:

$$\frac{E_4}{E_T} = A\left[\cos\xi + (C/A - \sin^2\xi)^{\frac{1}{2}}\right]^2$$

where:

E_4 = energy of the excited nucleus

$E_T = E_d + Q$ $\quad A = \dfrac{M_1 M_4 E_1}{(M_1+M_2)(M_3+M_4)E_T}$ $\quad C = \dfrac{M_2 M_3}{(M_1+M_2)(M_3+M_4)}\left[1+\dfrac{M_1 Q}{M_2 E_T}\right]$

The remaining symbols are explained in Figure 39b.

After the primary reaction has occured, the system of interest is the heavy

FIGURE 10

GRAPHICAL ANALYSIS
OF LABORATORY VELOCITIES

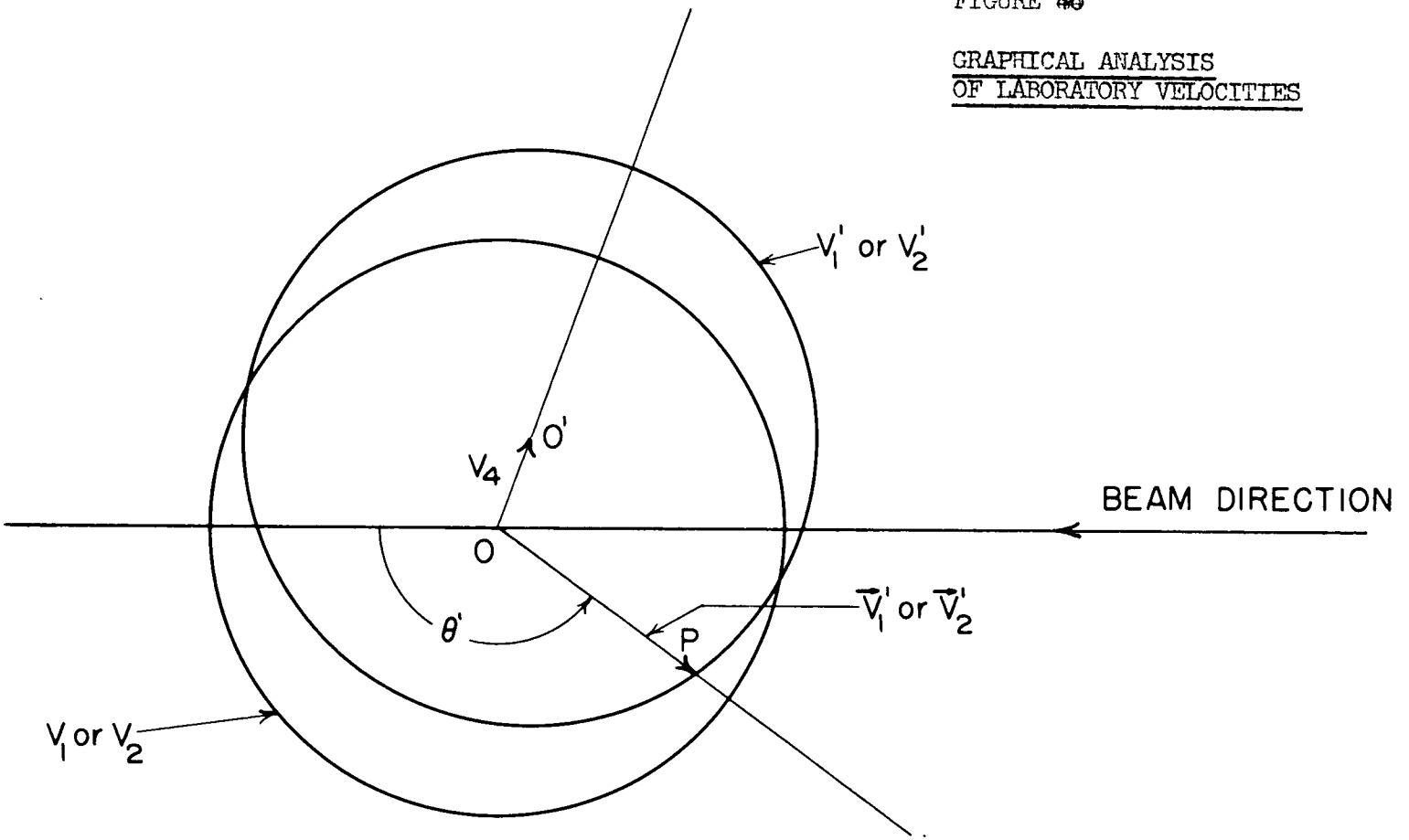

product or residual excited nucleus. In the centre of mass coordinates of the excited nucleus the two secondary particles will be emitted in opposite directions with velocities V_1 and V_2 as shown in figure 39a. These velocities will be determined by the amount of energy available for the break-up of the excited nucleus. To obtain the velocites of the secondary particles in the laboratory coordinates, V'_1 and V'_2, the velocity of the recoil excited nucleus V_4 must be added to V_1 and V_2.

The algebra for the solution of V'_1 and V'_2 in terms of V_4 and the Q of the reaction giving the two particles is tedious. However, there is a simple graphical method that gives sufficient accuracy for most cases. This method is shown in figure 40. The circle, with centre O, and marked "V_1 or V_2" , has a radius proportional to the absolute value of the velocity of the secondary particle in the centre of mass system of the excited nucleus M_4. The second circle, marked "V'_1 or V'_2" , has the same radius as the first, but its centre O' is shifted an amount proportional to V_4 and in the direction of V_4. The velocity of the secondary particle in the direction θ' in the laboratory coordinates is proportional to the distance between O and P, the point where the straight line in the direction θ' cuts the circle of centre O'.

The secondary particle will have a maximum energy in direction θ' , when the recoil velocity of the excited nucleus from the primary reaction is in the same direction. For this special case the expected maximum energies of the secondary alphas have been calculated for a deuteron bombarding energy of 1.35 Mev and are shown on page 32.

Maximum Secondary Alpha Energies: E_d :: 1.35 Mev

θ'	$Be^{8'}$---(a)a $(E_a)_{max}$	$Li^{7''}$---(t)a $(E_a)_{max}$	$Li^{7'''}$---(t)a $(E_a)_{max}$
180	2.34	2.38	2.63
160	2.42	2.44	2.66
140	2.50	2.56	2.75
120	2.68	2.78	2.92
105	2.87	2.98	3.12
90	3.11	3.26	3.38

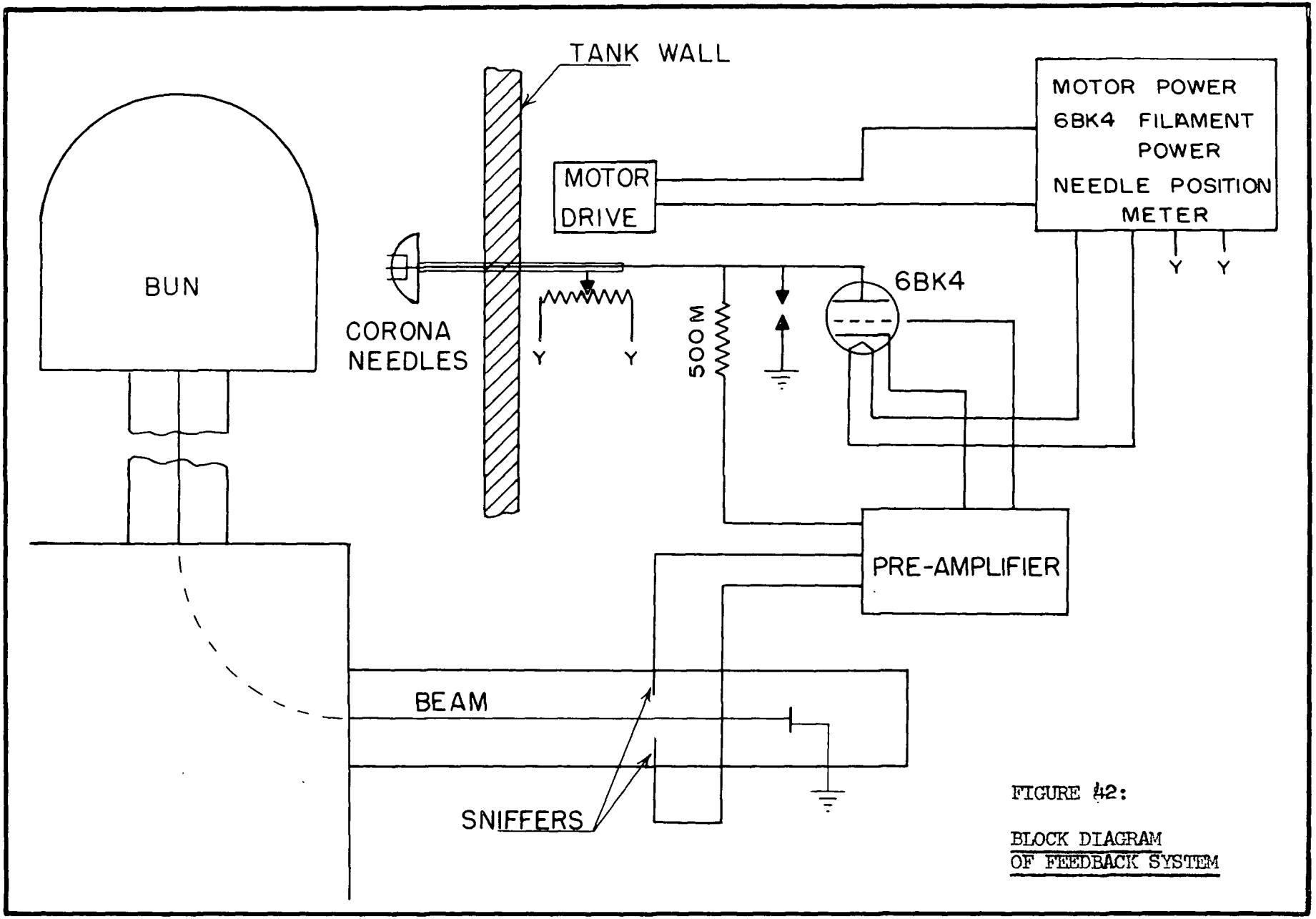

FIGURE 42:

BLOCK DIAGRAM OF FEEDBACK SYSTEM

APPENDIX II

CORONA STABILIZER

A. General Description:

The Corona Stabilizer was designed to replace the electron gun energy stabilization of the U.B.C. Van de Graaff accelerator. The schematic diagram is shown in Figure 41. Its use has several advantages over the electron gun. They are:

(i) the high background of X-rays caused by the accelerated electrons hitting the top terminal bun have been eliminated.

(ii) the energy of the set can be varied easily over a range of 200 Kev, by changing the field of the 90 degree deflecting.

(iii) the vacuum system of the accelerator is greatly simplified, in that the differential pumping column used for the electron gun could be removed. This column space has been replaced by a periscope system allowing a bank of meters monitoring essential points in the circuits of the top-terminal ion source and beam focus lens to be seen from the main control panel.

The essential part of the Corona Stabilizer is the corona needle mount in the Van de Graaff, which is marked on the geneval block diagram, Figure 42. This mount consists of a group of six needles projecting from a grounded aluminum shield, shown in Figure 43. The shield and needles can be moved with respect to the bun by a motor drive mounted outside the tank. The relative position of the needles is given by a slide-wire rheostat, connected to a meter on the control panel. The circuit for the motor drive, 6BK4 filament power, and the needles position meter is given in Figure 44. The con-

figuration of the accelerator bun, needles, and the shield acts like the plate, cathode and grid, of a gas triode. Figure 45 shows the measured characteristics of this triode. The cascode configuration of this gas triode and the 6BK4 triode results in a high gain amplifier with a gain of the order of 40,000. The theoretical gain for this circuit is calculated in Section B-1 of this appendix.

If the beam is not bent exactly 90 degrees the amount of beam hitting the two sniffers will be different. Any difference between the currents hitting the sniffers will be amplified in the pre-amplifier, with a gain of 25, and applied as a voltage signal between the grid and cathode of the 6BK4. This signal will change the accelerator voltage on the bun so as to remove the current difference between the sniffers. For good stability the loop gain for the system should be large. Assuming a 1 KV change in the set energy, an analysis was done on the resulting correction signal applied to the bun by the Corona Stabilizer. The correction signal was found to vary from 100 KV to 1000 KV, depending on the set energy and the beam focus. This analysis is done in Section B-2 of this appendix. Because the focus of the beam is a function of the energy, there is a change in the amount of horizontal current over the range of stabilization, but an adjustment of the two ion source lens voltages can easily be eliminate this effect.

To overcome the problem of radiation of spurious pulses from high voltage corona, the 6BK4 triode, spark gap, and bleeder resistor were mounted right on the end of the brass rod shielding the needle lead: as shown in Figure 46.

B. Theoretical Discussions:

1. The Gain analysis of the gas triode and 6BK4 triode. The

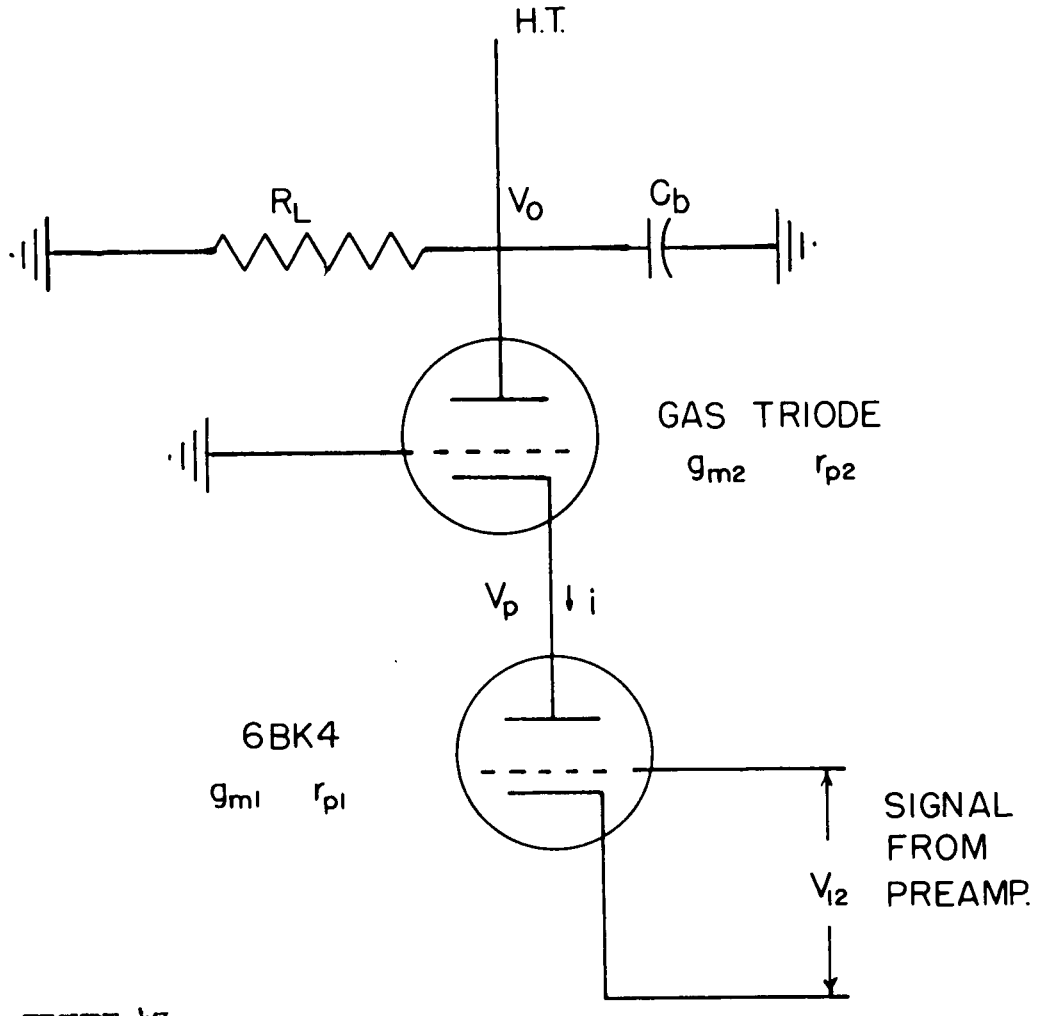

FIGURE 47:

DIAGRAM FOR GAIN ANALYSIS OF CASCODE CONFIGURATION

	GAS TRIODE	6BK4
g_m	4 mumhos	100 mumhos
r_p	2×10^{10} ohms	11×10^6 ohms

$$A = \frac{V_o}{V_{12}} = \frac{g_{m1}}{\frac{1}{R_L} + \frac{1}{g_{m2} r_{p1}} \left[\frac{1}{R_L} + \frac{1}{r_{p2}} \right]} = 49{,}000$$

schematic diagram corresponding to this analysis is Figure 47. V_o is the change in the set volts due to a dc shift in V_{12}, the 6BK4 grid-to-cathode voltage. Let i be the corresponding current caused by this change in voltage. Therefore:

(1) $V_o = iR_L$ R_L is the stack resistance ($26 \times 10^9 \Omega$)

(2) $i = V_{12}g_{m1} - V_p/r_{p1}$ V_p is the 6BK4 plate voltage.

rearranging (2) gives $V_p = r_{p1}(V_{12}g_{m1} - i)$. (2')

(3) $i = V_p g_{m2} - V./r_{p2}$

g_{m1} is the transconductance of the 6BK4 triode.

g_{m2} " " " " " gas triode.

r_{p1} is the plate-resistance of the 6BK4 triode.

r_{p2} " " " " " gas triode.

Substituting (2') into (3) and using (1) gives:

$$V_o/R_L = g_{m2}r_{p1}[V_{12}g_{m1} - V_o/R_L] - V_o/r_{p2} \qquad (4)$$

The gain of the circuit is defined as $A = V_o/V_{12}$.

Substituting into (4) gives:

$$1/R_L = g_{m2}r_{p1}[V_{12}/A - 1/R_L] - 1/r_{p2}$$

and rearranging gives:

$$A = \frac{g_{m1}}{\frac{1}{R_L} + \frac{1}{g_{m2}r_{p1}}\left[\frac{1}{R_L} + \frac{1}{r_{p2}}\right]}$$

FIGURE 48:

FLUCTUATING BEAM

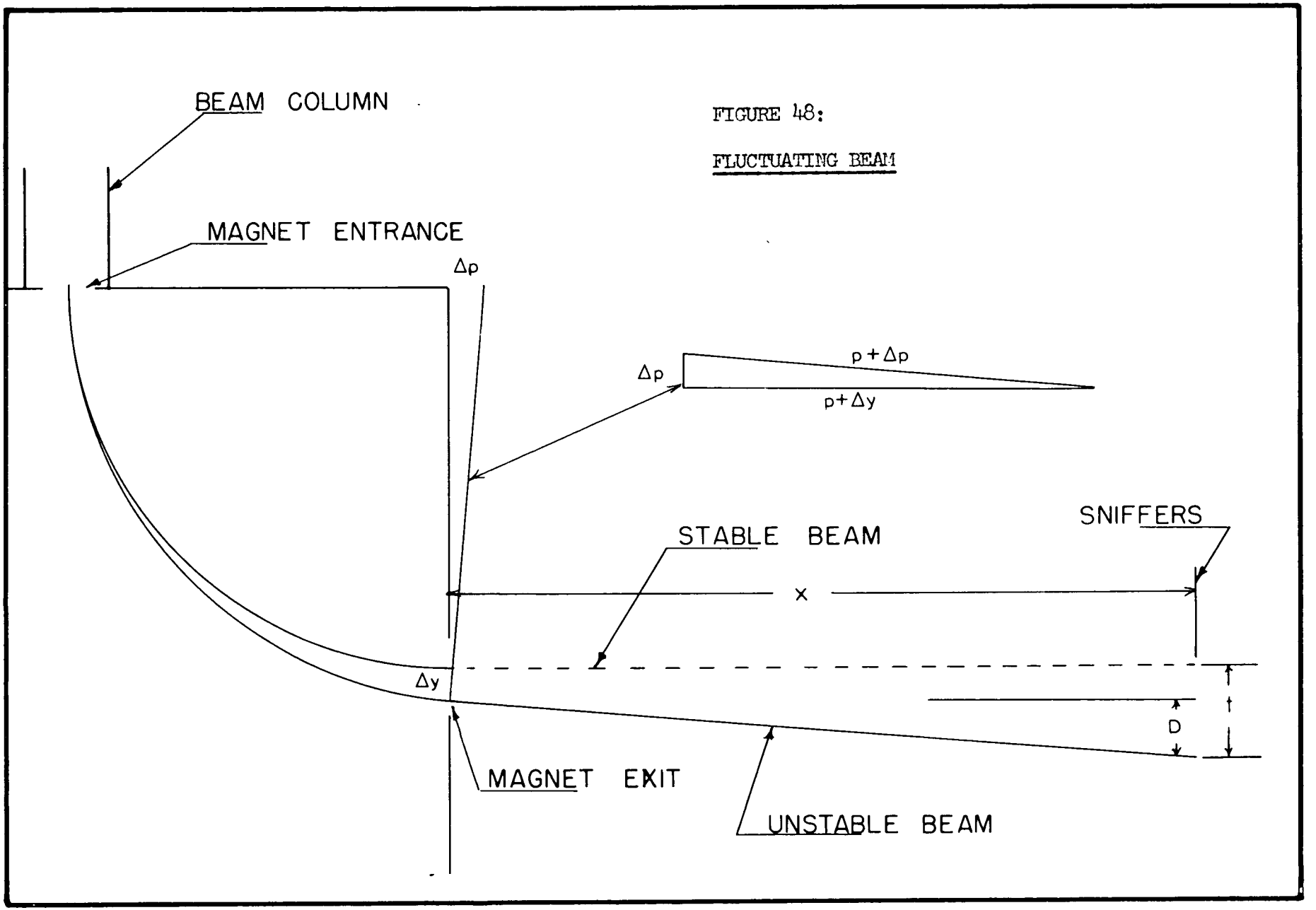

Taking values of g_{m2} and r_{p2} from Figure 45 for the gas triode as:

g_{m2} 4 mumhos

r_{p2} 2×10^{10} ohms

and the measured values of g_{m1} and r_{p1} for the 6BK4 triode as:

g_{m1} 100 mumhos

r_{p1} 11×10^{6} ohms.

gives the value of A as: 49,000.

This is in good agreement with the actual measured gain of 40,000.

2. Loop gain analysis for the whole stabilizer system.

The energy that allows the beam to be bent by 90 degrees through the deflecting magnetic field, is the energy of reference that the corona stabilizer must maintain. The magnetic field bending the beam is the constant of reference to which all stabilization is referred. The corona stabilizer must have enough feedback gain so that any variation in the set voltage is corrected by an even larger feedback signal. The greater the loop gain, the better is the energy stabilization. Figure 48 shows a schematic diagram, used in this discussion, of a beam changing in energy, and hence fluctuating in position because of the magnetic field.

The radius of curvature of the beam in the magnetic field is given by:

(1) $p = K(2mE)^{\frac{1}{2}}/B$, where E is the energy of the particles in the beam, and B is the magnetic field. Dividing the derivative of equation (1) by equation (1) gives:

(2) $dp/p = \frac{1}{2}dE/E$

If the set volts changes by dE, the beam will move a total distance of "t" at the sniffers. At the magnet box opening:

(3) $(p + dp)^2 = (dp)^2 + (p + dy)^2$ Rearranging (3) gives:

(3') $dy = \sqrt{(p - dp)^2 - (dp)^2} - p$

The extra deflection caused by the beam not leaving the magnet box opening:

(4) $D = xdp/(p + dp) \cong xdp/p$

Therefore the total deflection at the sniffers is:

(5) $t = xdp/p + (p^2 - 2dp)^{\frac{1}{2}} - p$

Assuming that the beam has a uniform cross-section and a rectangular shape when it passes through the sniffers, one can make a simple calculation to determine the signal reaching the pre-amplifier when a fluctuation occurs in the set volts. If dE is 1 KV and E is 1000 KV, then dp is .014 cm., as p is 28 cm. for the Van de Graaff magnet. Therefore "t" is .064 cm. If the beam has a shape as shown in Figure 49a, the resulting current difference between the sniffers will be .086 μamp. With a sniffer sensitivity of .47 Meg-ohms, the resulting signal on the bun will be 40,000 volts. The Loop Gain is therefore 40. The effect of different set energies, different beam cross-sections and different sniffer slit widths, on the loop gain are summarized in Figure 50.

Two beam distributions are considered: an unfocused beam, which was approximated by a beam of constant current distribution over its whole area, and a focused

beam which was approximated by the distribution $j = A \exp(-x^2 - .04y^2)$, as shown in Figure 49b. For the constant current distribution, the loop gain is independent of the sniffer width, and is an order of magnitude lower than that for the focused beam. The sniffer width has a definite effect on the loop gain for the focused beam. As seen from Figure 50b, for a given amplifier gain a higher loop gain implies a lower current allowed to pass through to the target. A third curve in the figure is the product of the loop gain and the relative current let through the sniffers. This product reaches a maximum at a sniffer width of approximately .65 cm. so a compromise can be made between energy stability and target current.

C. Physical Operation Characteristics:

Many variables affect the best operation position of the Corona Stabilizer needles. The two most important of these are the tank pressure and the energy of the set. For proper control the needles must be brought closer to the bun as the pressure of the tank is increased, the energy remaining constant; and the needles must be moved farther from the bun as the energy is increased, the pressure remaining constant.

The relative humidity of the tank has has a smaller effect on the stabilizer control. For higher humidity the needles must be farther out for control, if the energy is constant. No measurable change in the stabilization was noted when 10 lbs. of Freon was added to the tank gas. Higher amounts of Freon should have some effect, as it is added to suppress bun-to-ground sparking, so it should also suppress current pick-up on the corona needles. These characteristics are shown in figures 51 and 52.

Because of the voltage specifications of the lead carrying the current from the needles to the plate of the 6BK4 triode, the highest safe voltage that could be applied to the 6BK4 plate was approximately 10 KV. Under conditions of low beam current a range of stabilization of 450 Kev was obtained, with the 6BK4 plate at 10 Kv. Presumably with higher plate voltages even wider ranges could be obtained. Figure 53 shows the effect of increasing the plate voltages on the stabilization range. Because the beam focusing conditions change quite drastically over such an energy range, larger ranges of stabilization would be inadvisable.

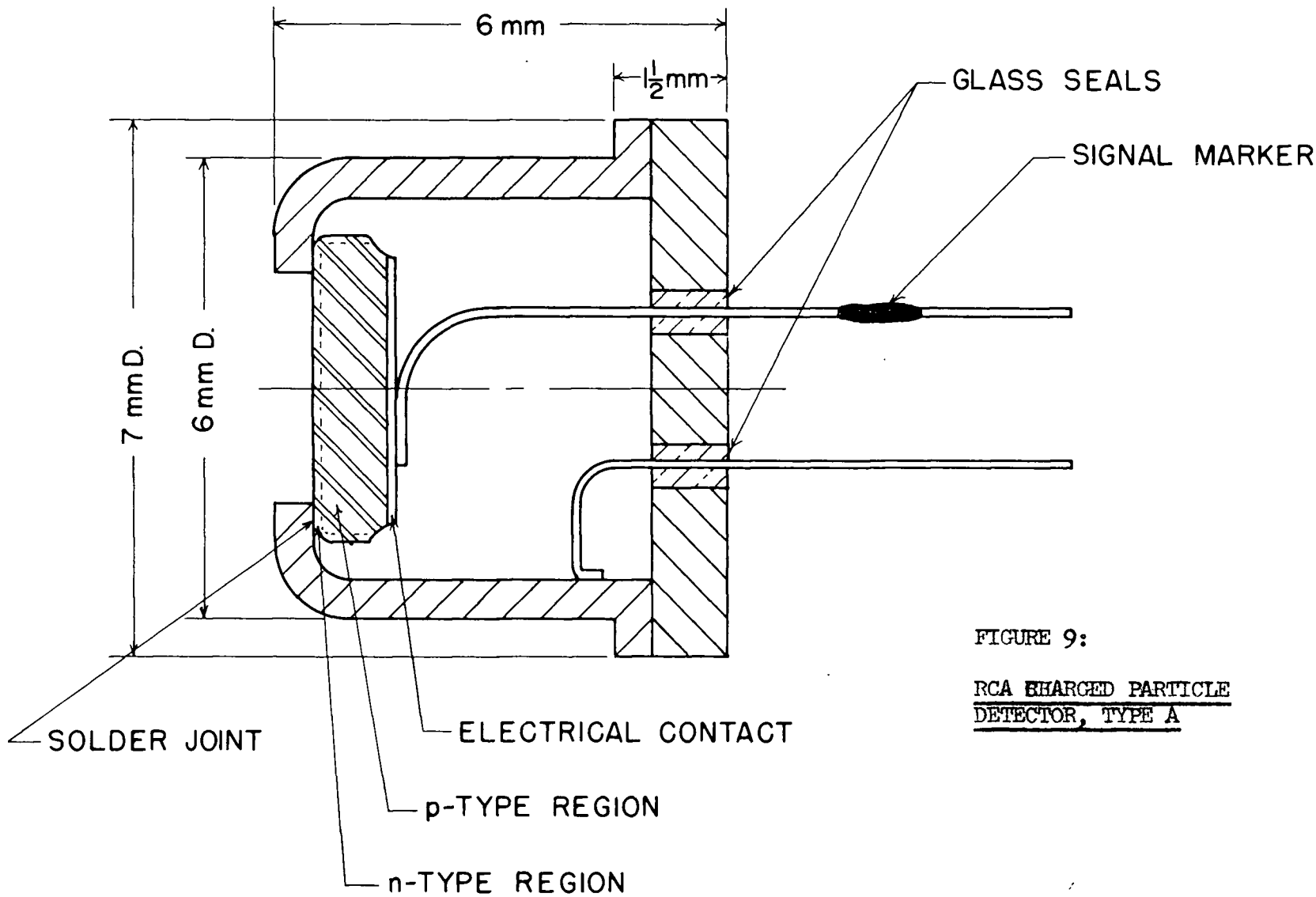

FIGURE 9:

RCA CHARGED PARTICLE DETECTOR, TYPE A

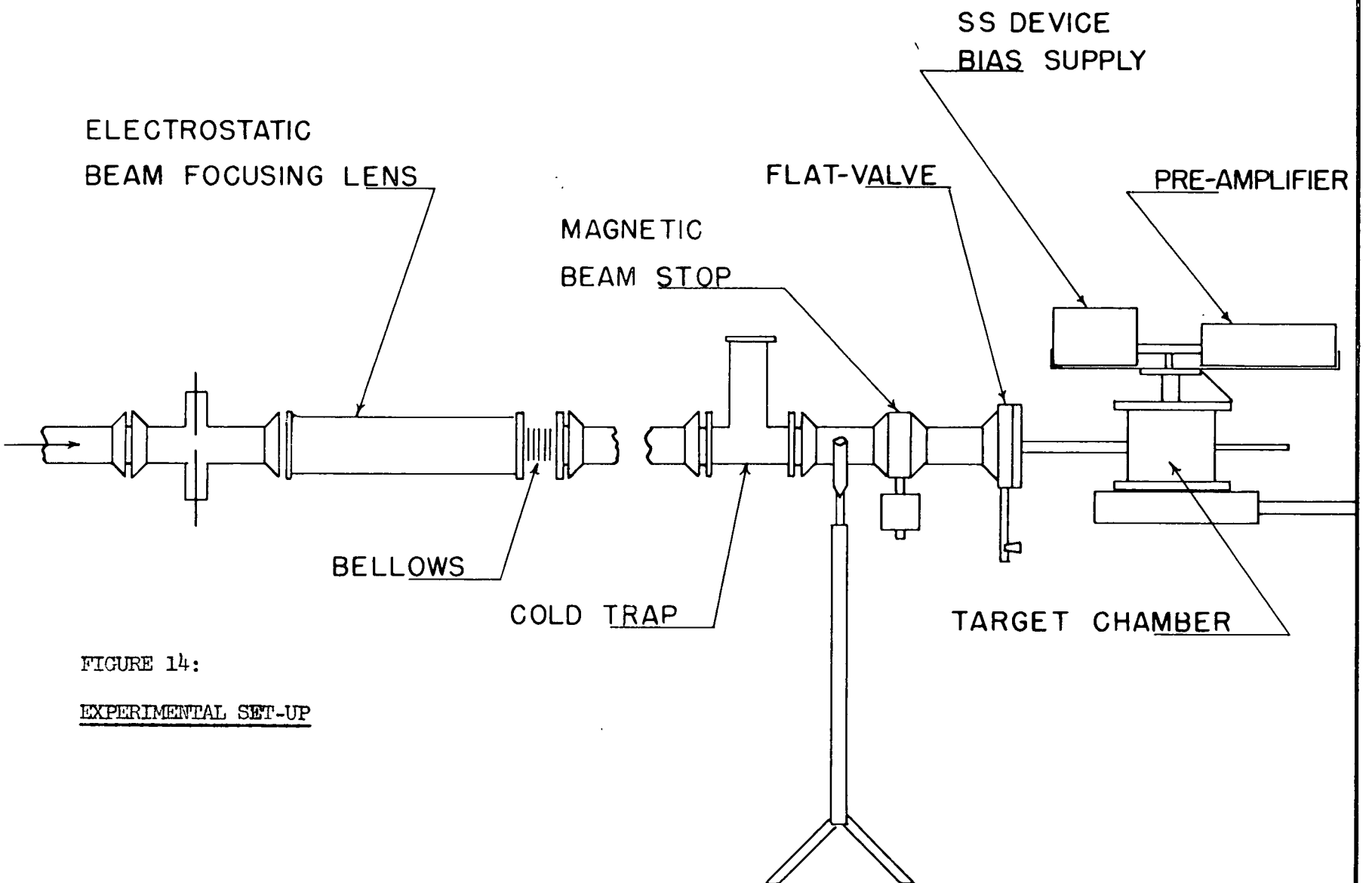

FIGURE 14:

EXPERIMENTAL SET-UP

FIGURE 16:

TARGET AND COUNTER GEOMETRY

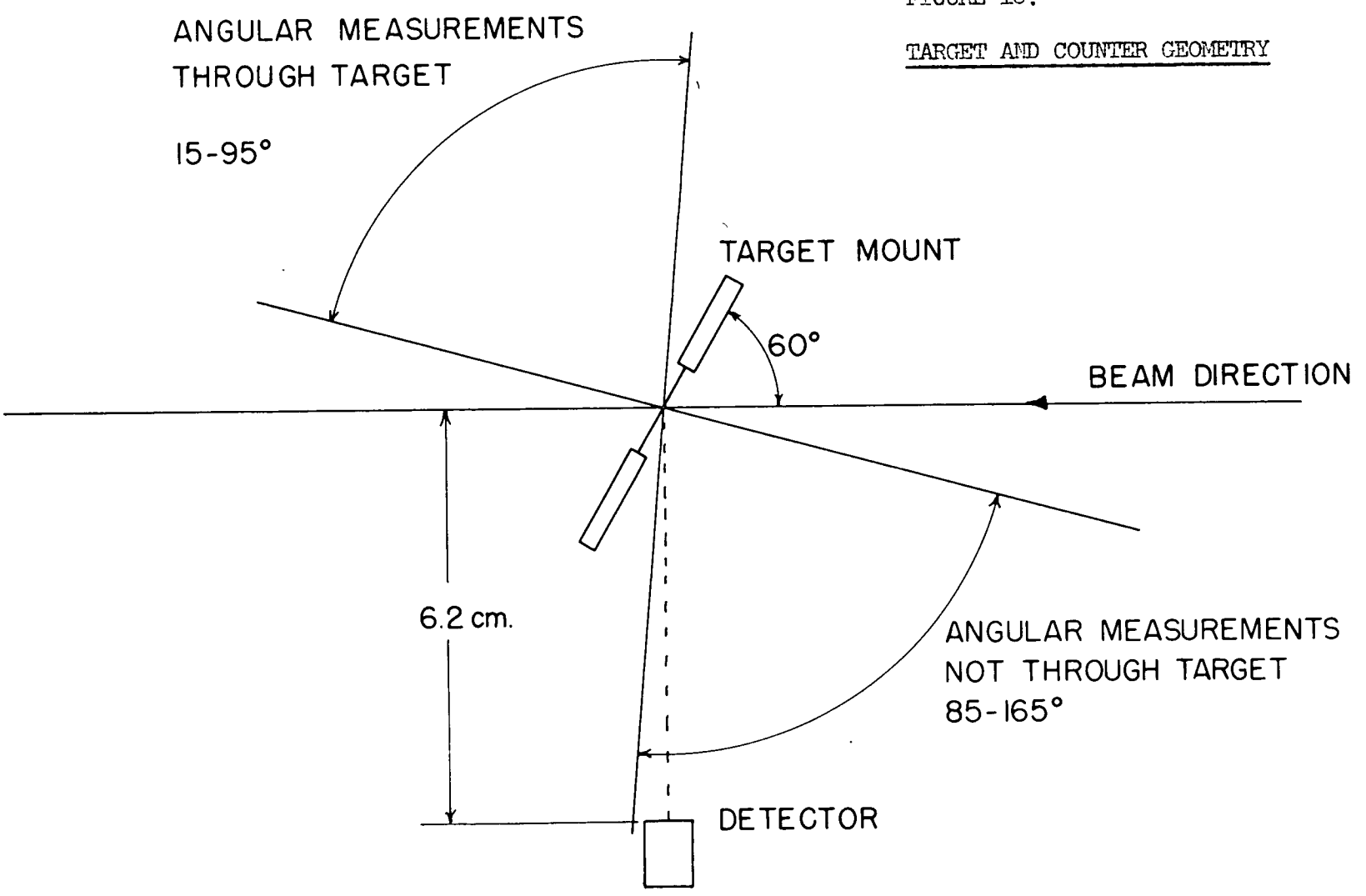

FIGURE 17

ELECTRONICS

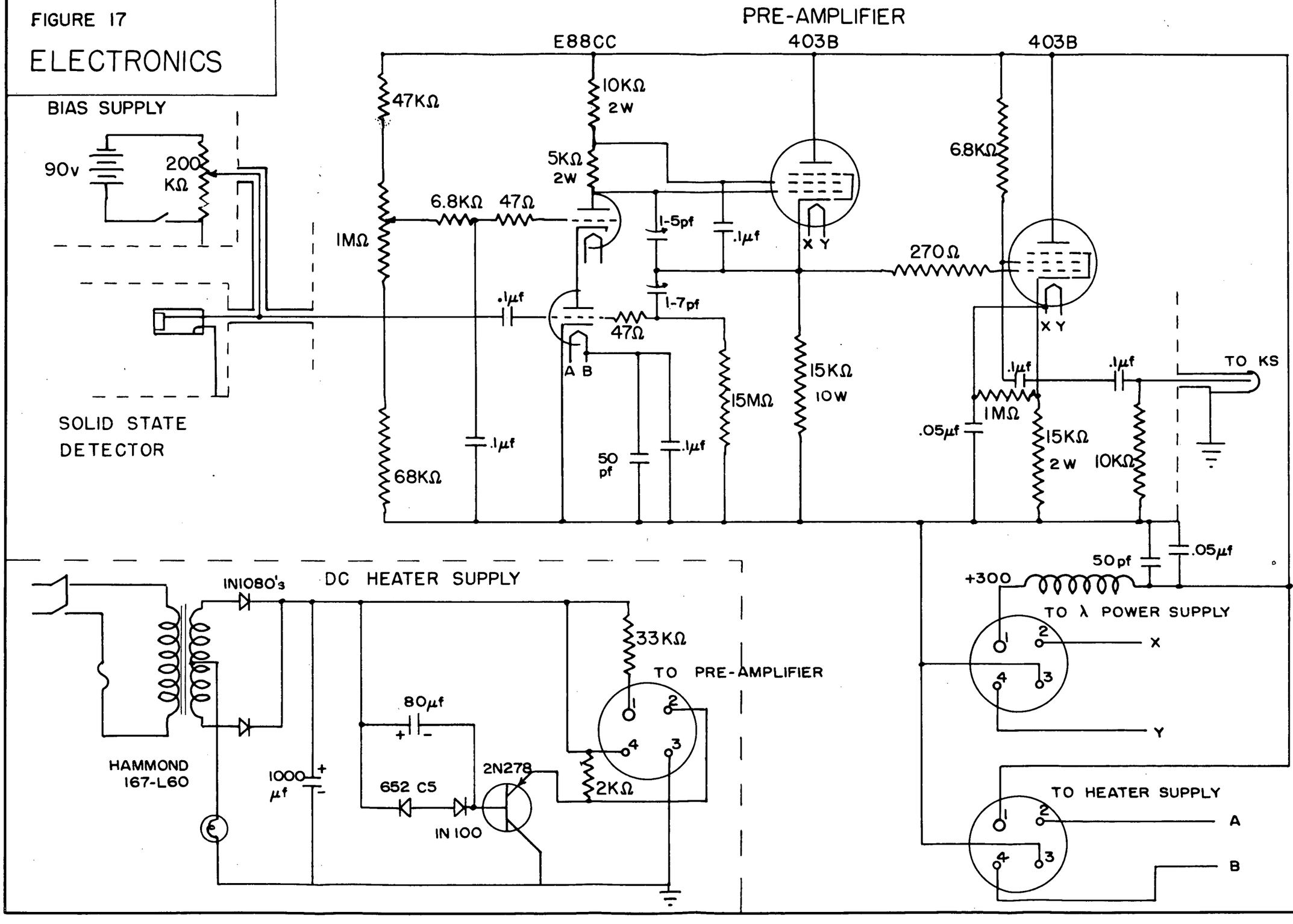

FIGURE 23:

ALPHA PARTICLE ANGULAR DISTRIBUTION

E_d: .500 Mev

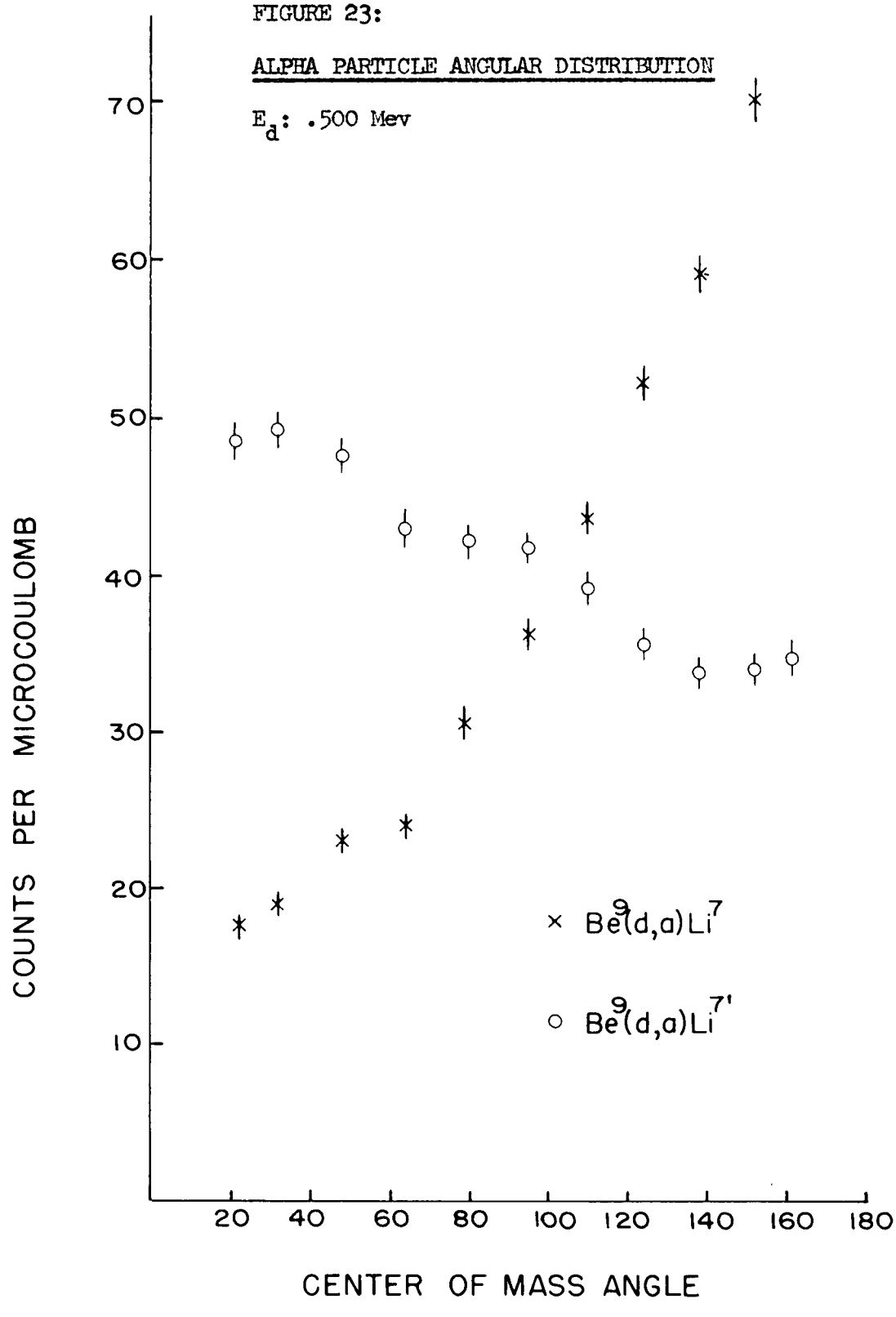

FIGURE 24:

ALPHA PARTICLE ANGULAR DISTRIBUTION

E_d: .750 Mev

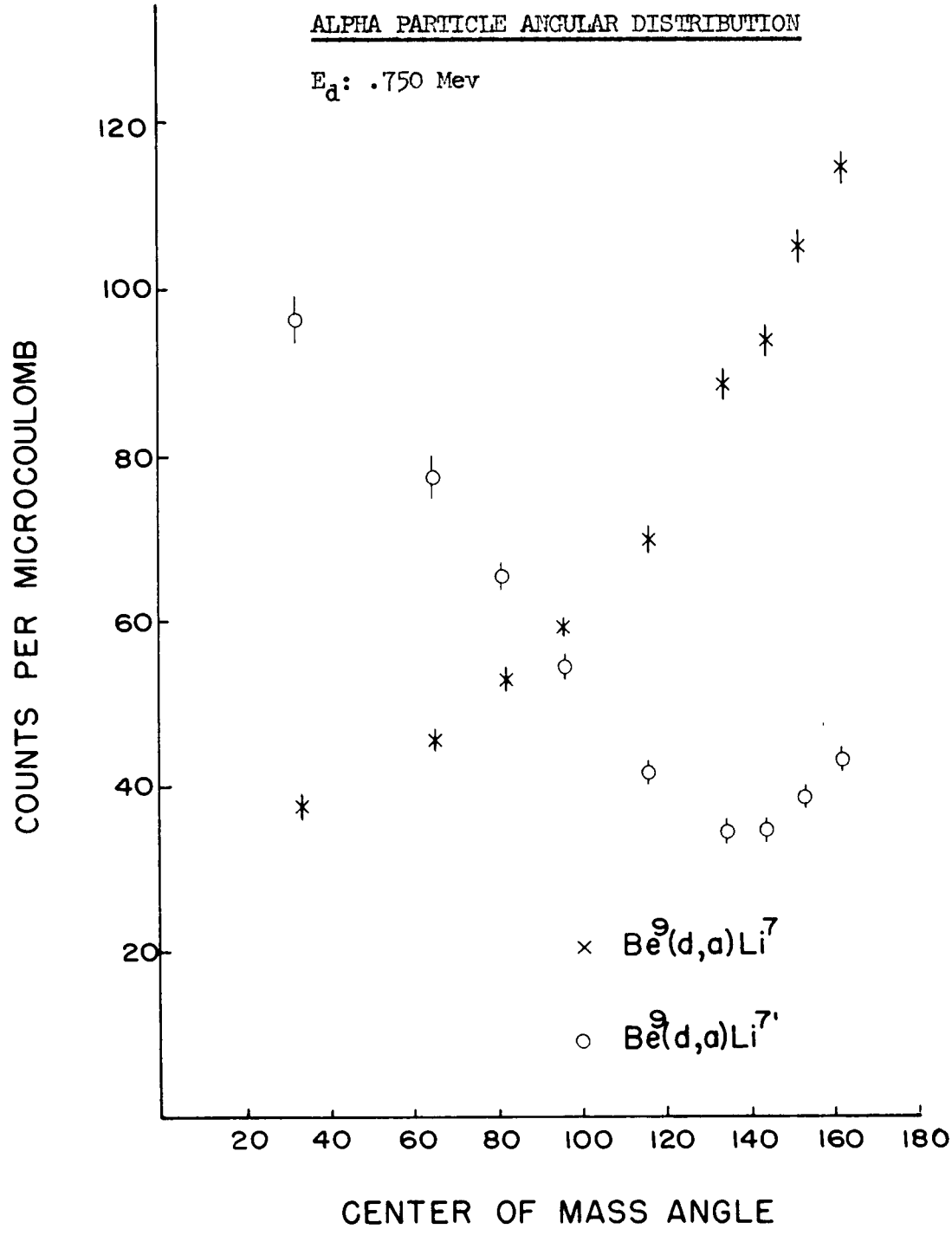

FIGURE 25:

ALPHA PARTICLE ANGULAR DISTRIBUTION

E_d : 1.00 Mev

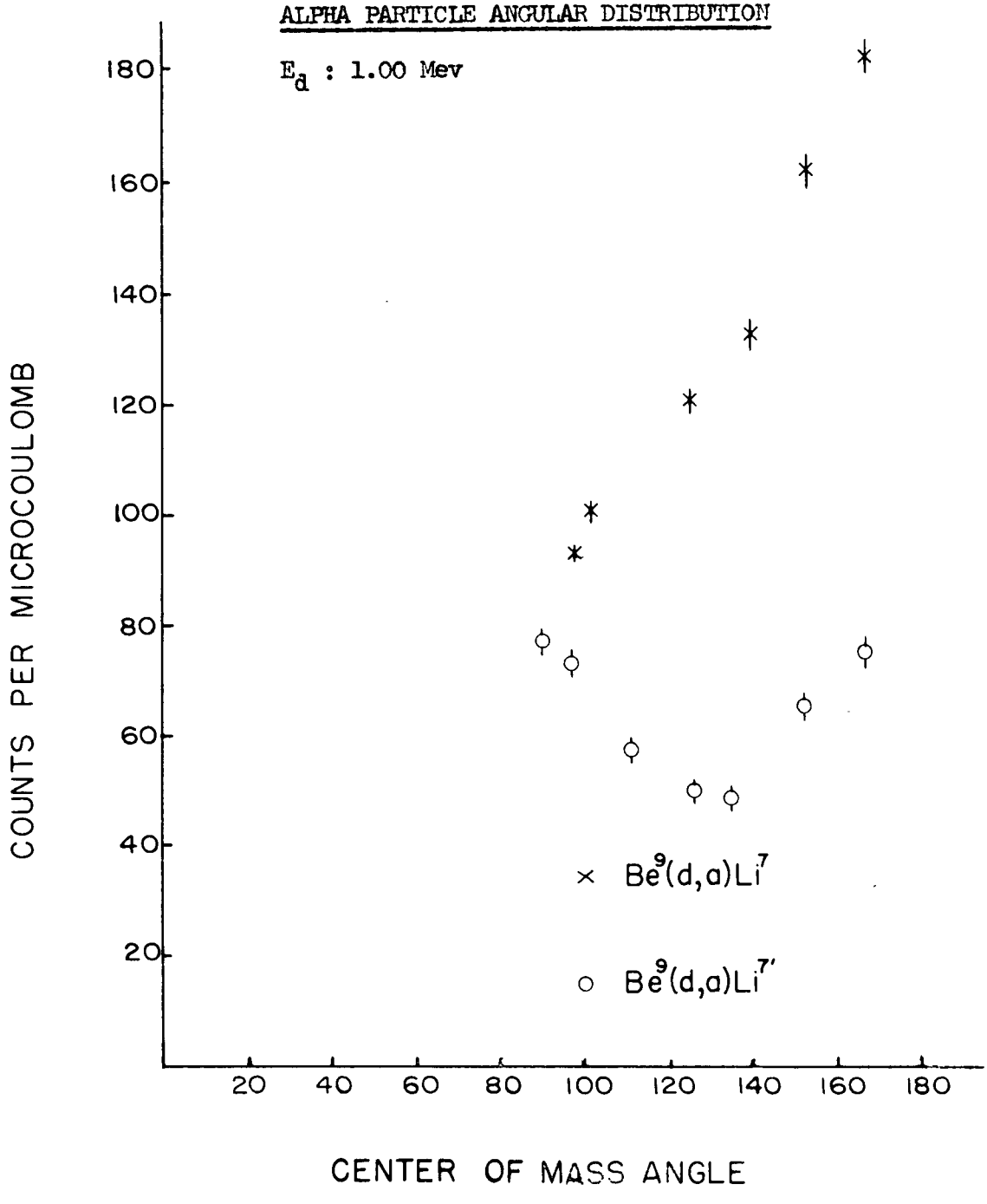

FIGURE 26:

ALPHA PARTICLE ANGULAR DISTRIBUTION

E_d: 1.16 Mev

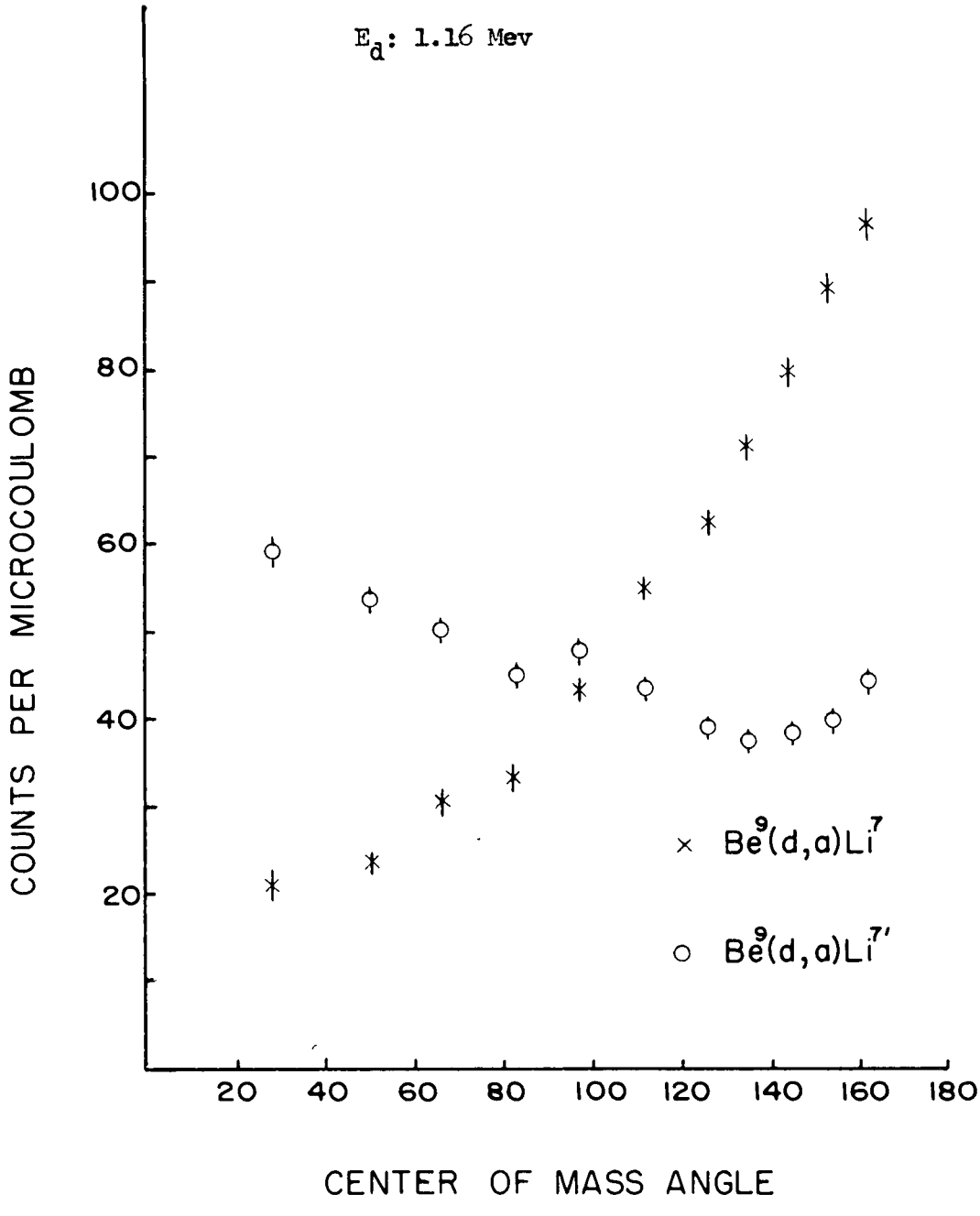

FIGURE 27:

ALPHA PARTICLE ANGULAR DISTRIBUTION

E_d: 1.35 Mev

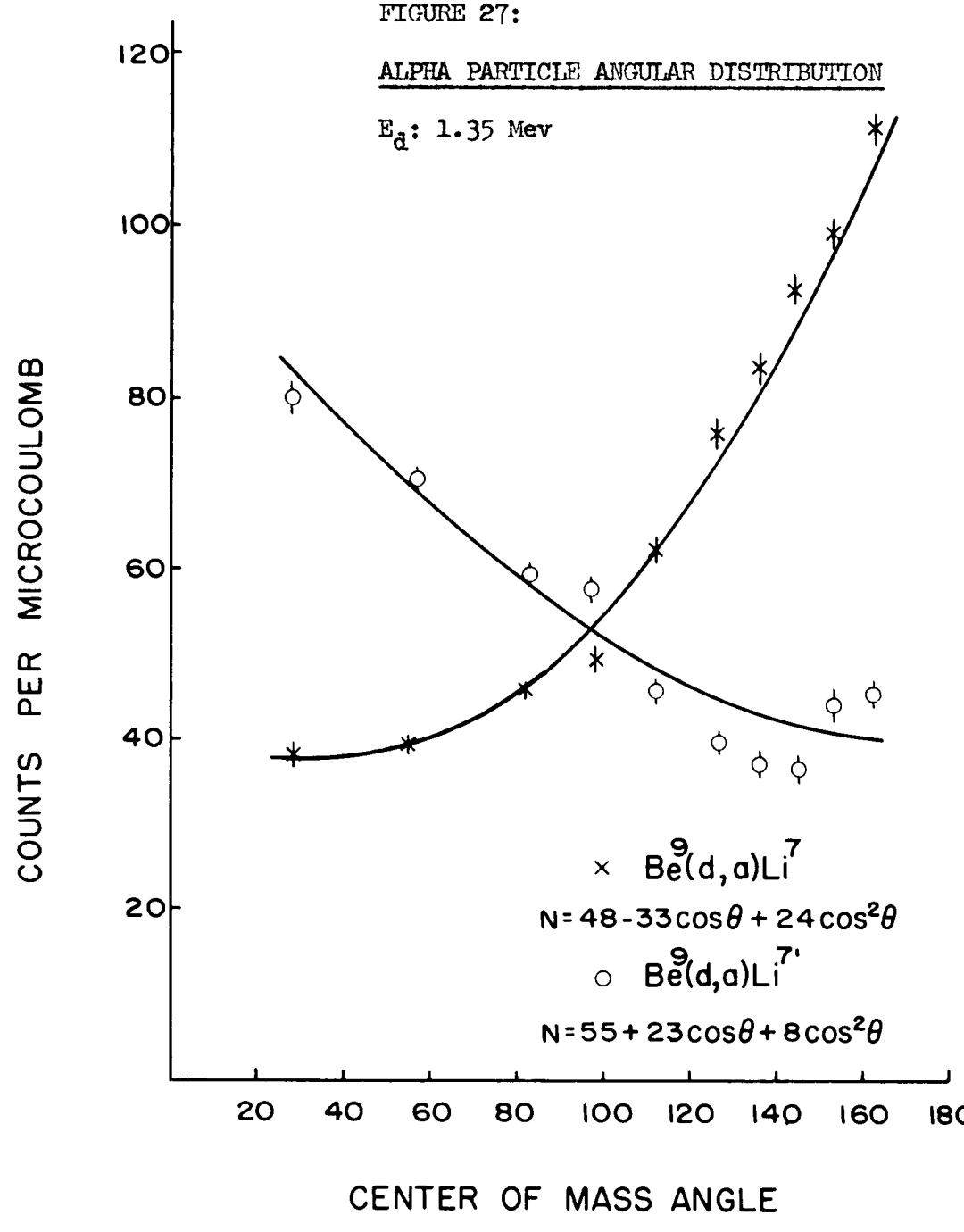

FIGURE 28:

ALPHA PARTICLE ANGULAR DISTRIBUTION

E_d: 1.16 Mev

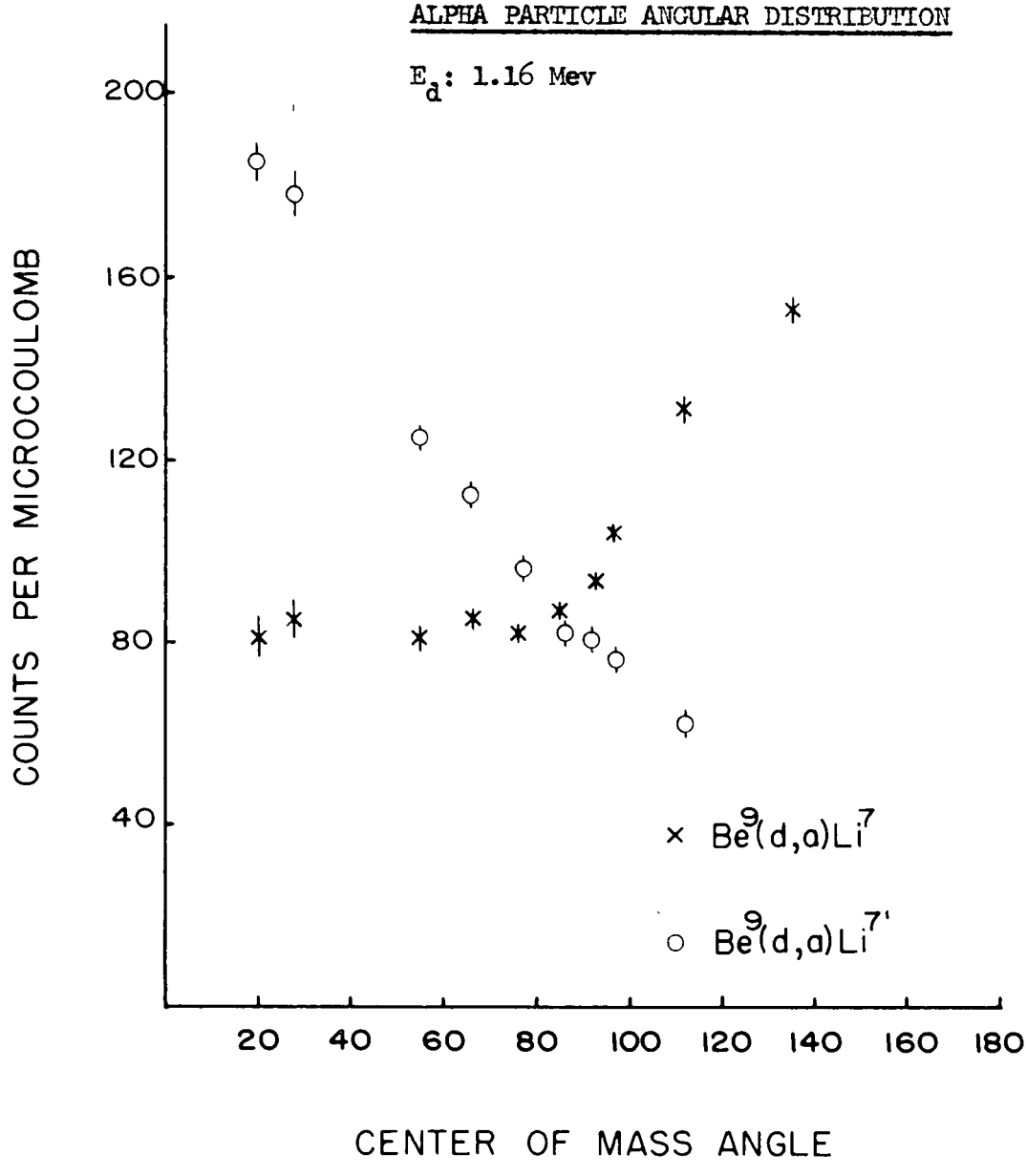

FIGURE 29:

ALPHA PARTICLE ANGULAR DISTRIBUTION

E_d: 1.35 Mev

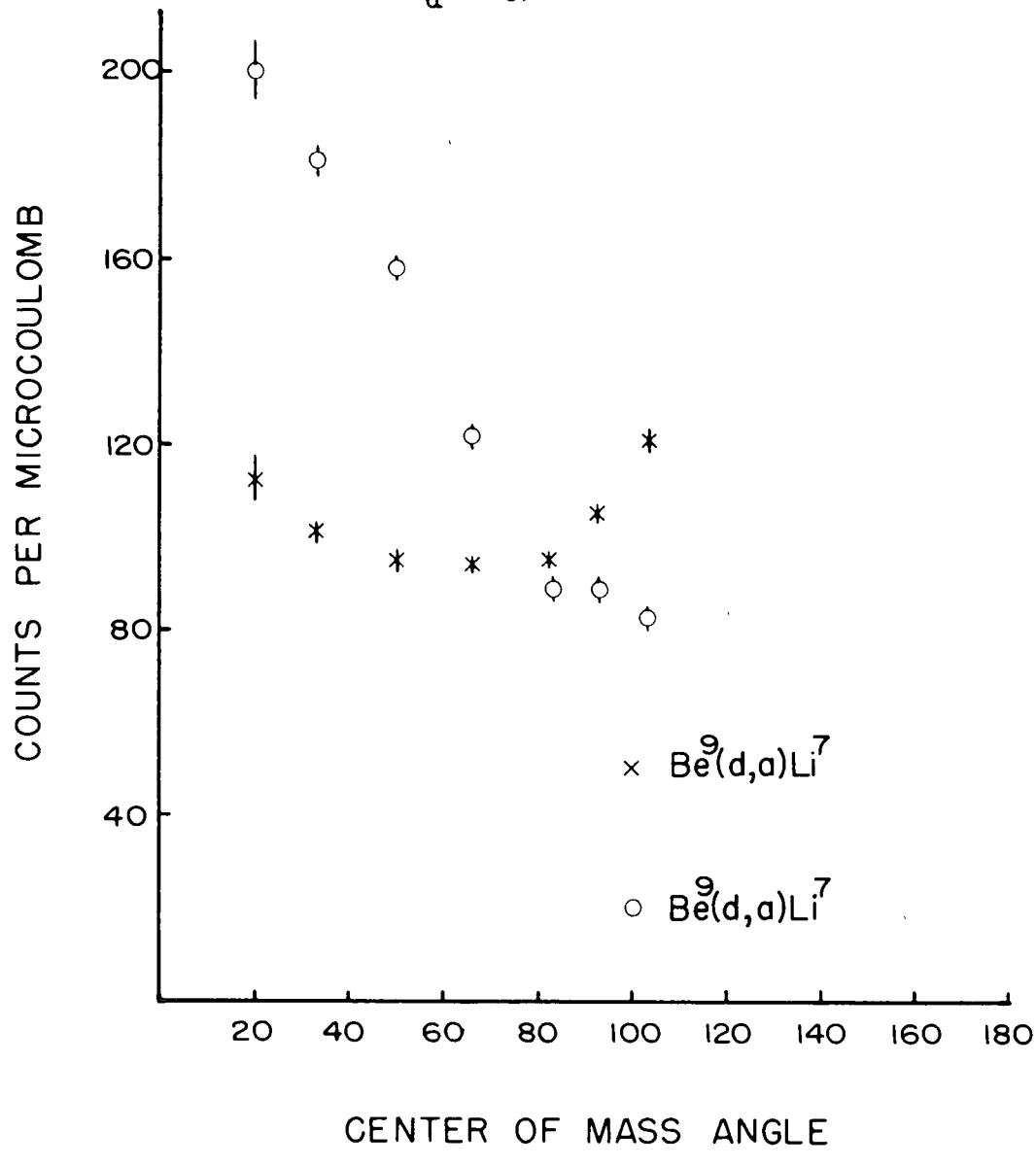

FIGURE 30a: Fraction of Alpha Particles from $Be^9(d,a)Li^7, Li^{7*}$, which go to the First Excited State.

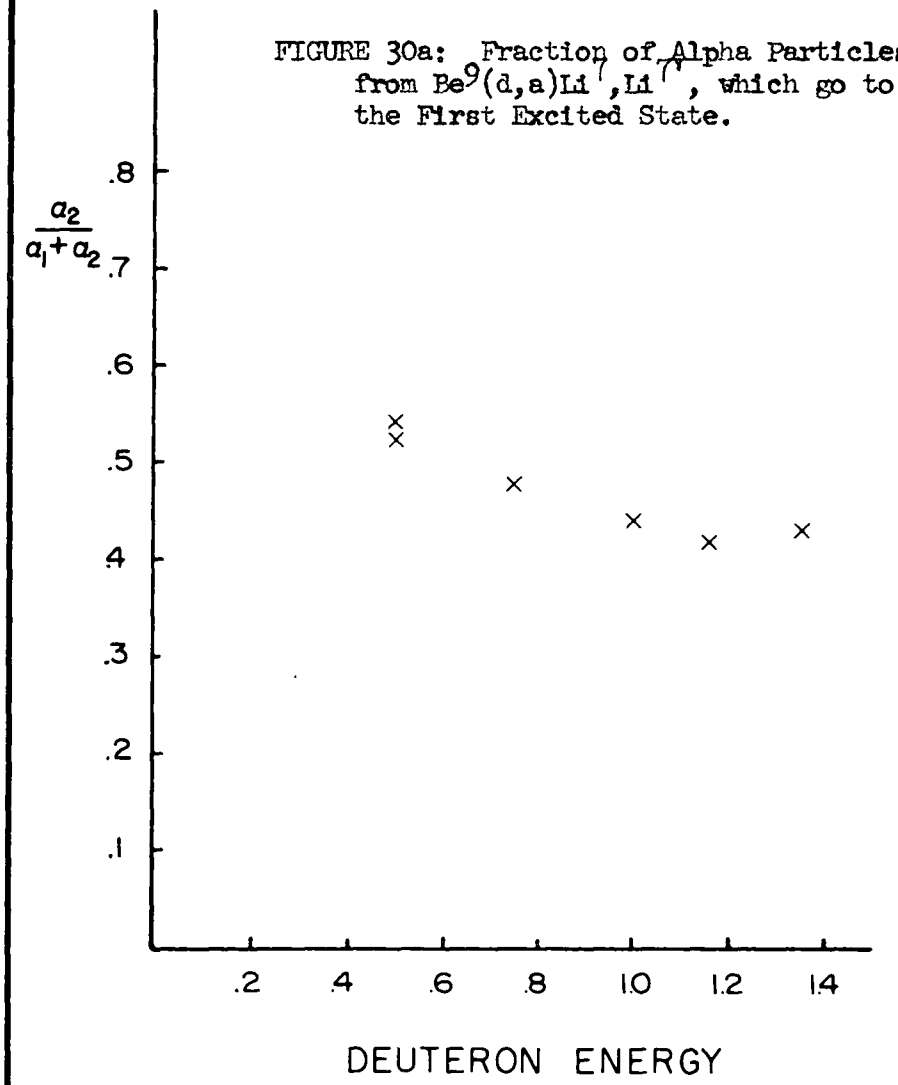

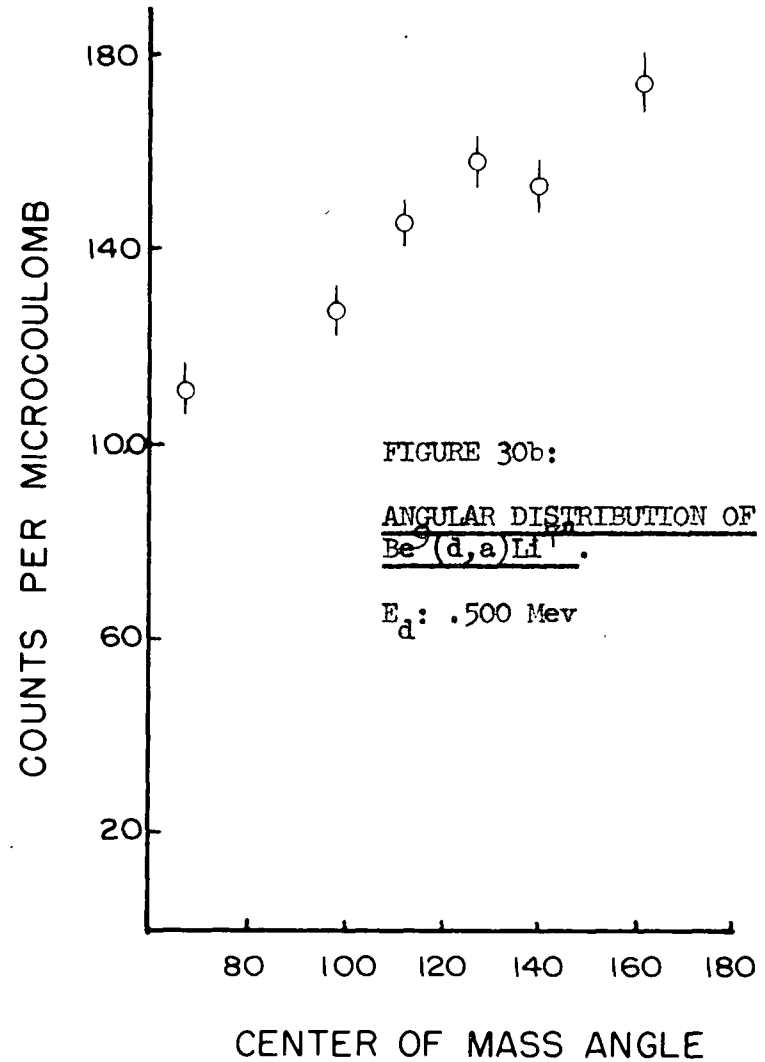

FIGURE 30b:

ANGULAR DISTRIBUTION OF $Be^9(d,a)Li^{7*}$.

E_d: .500 Mev

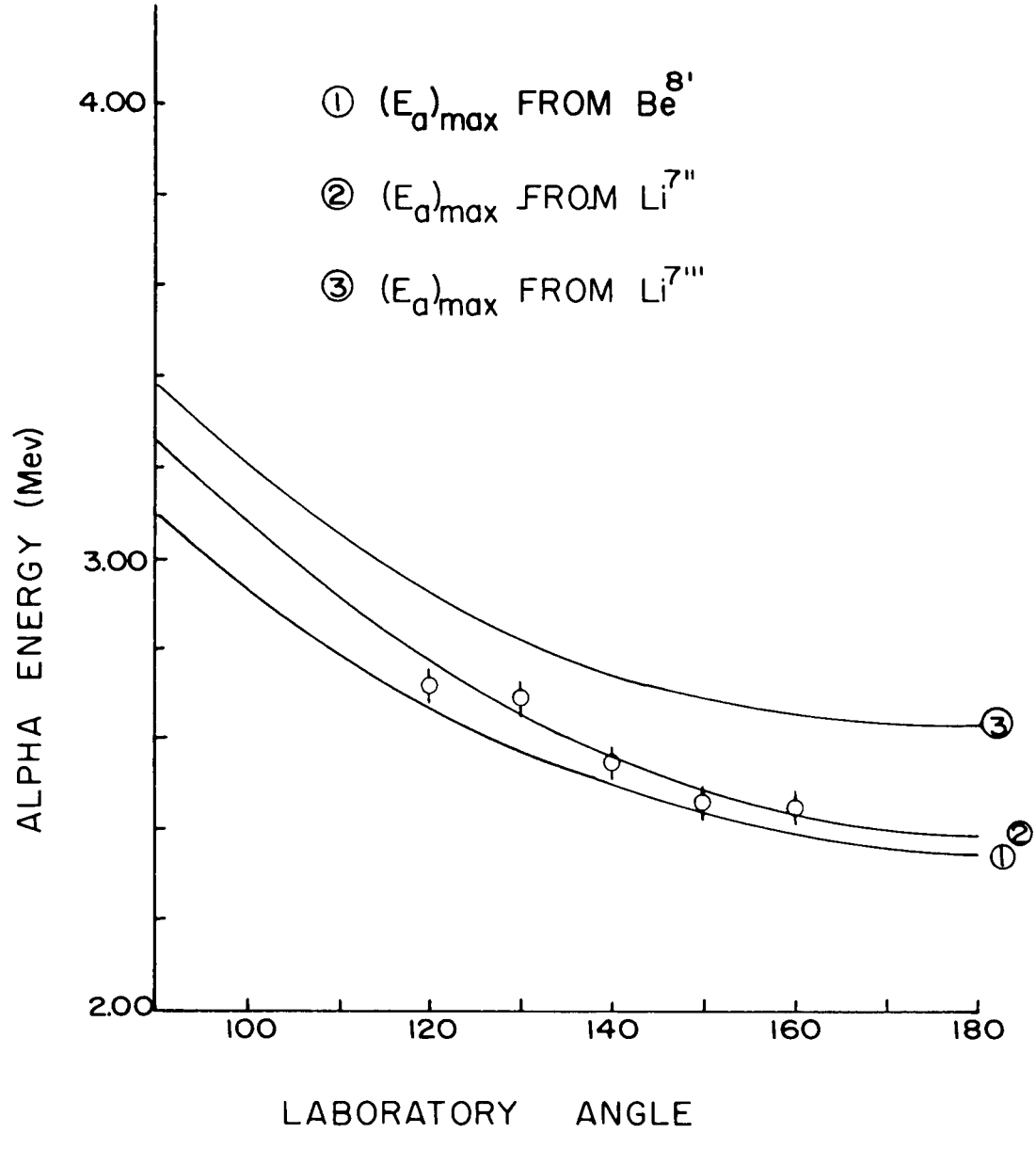

FIGURE 33:

SECONDARY ALPHA MAXIMUM ENERGIES:
THEORETICAL AND ACTUAL

E_d: 1.35 Mev

FIGURE 34:

ANGULAR DISTRIBUTIONS OF $Be^9(d,t)Be^8$

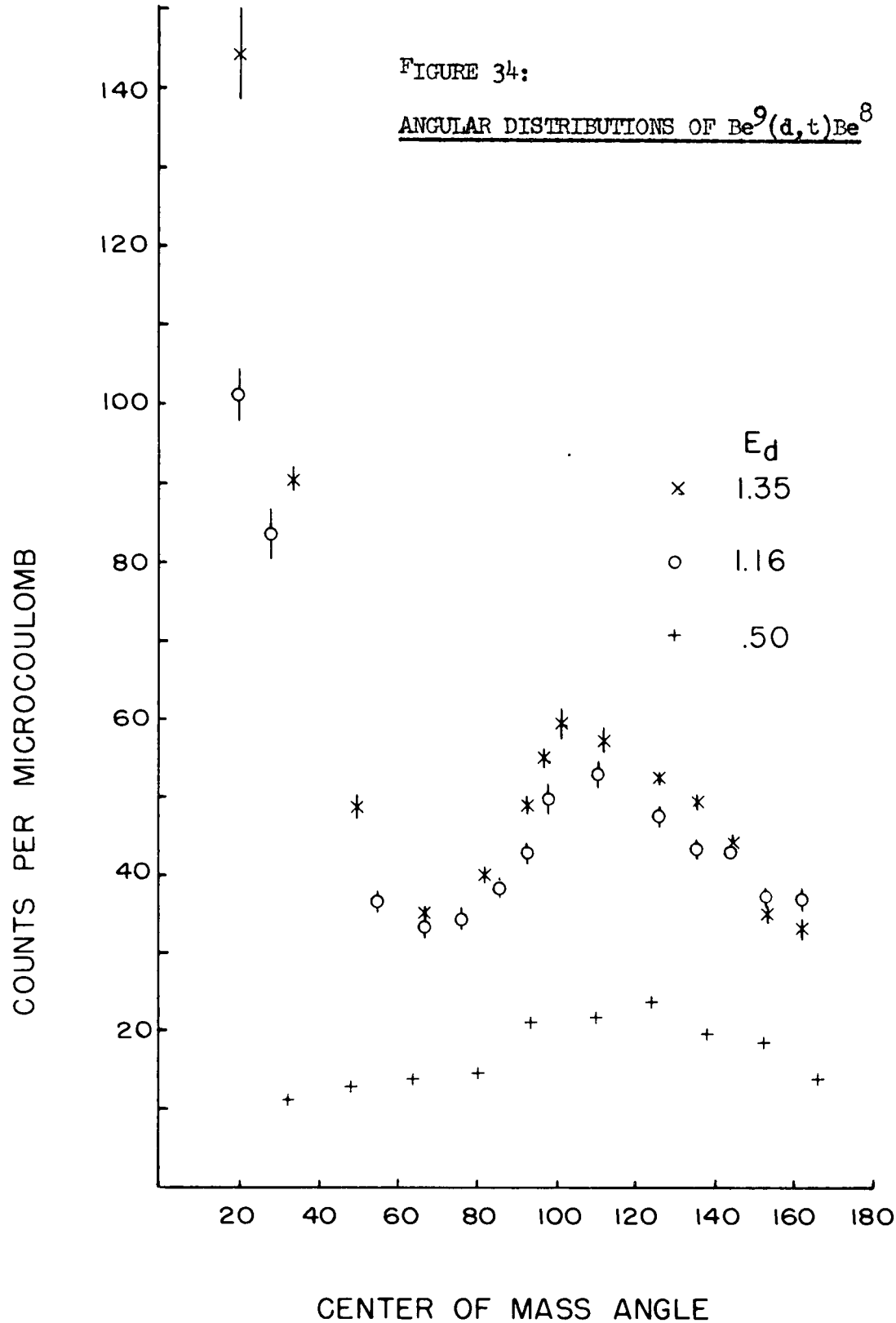

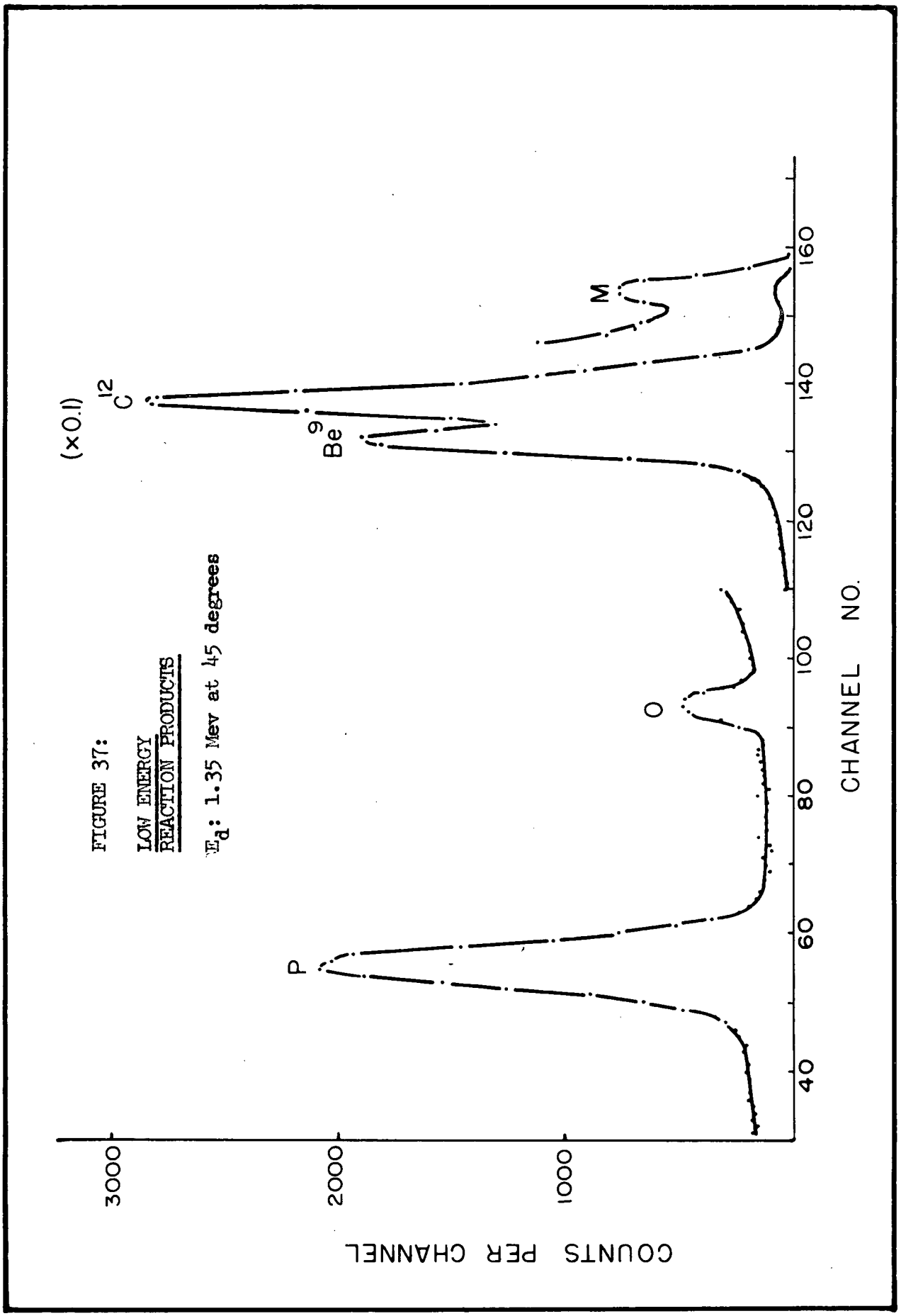

FIGURE 37:

LOW ENERGY
REACTION PRODUCTS

E_d: 1.35 Mev at 45 degrees

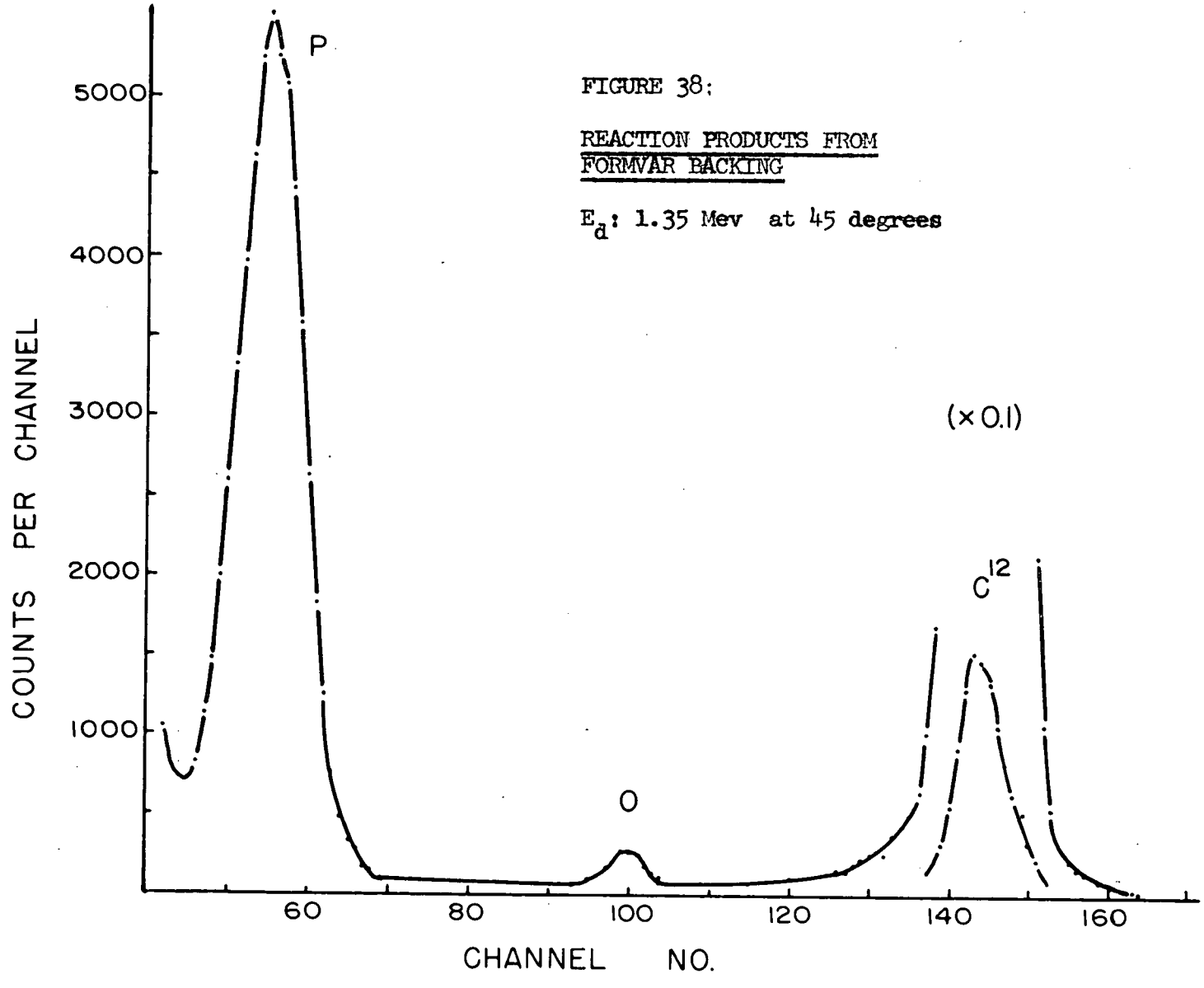

FIGURE 38:

REACTION PRODUCTS FROM FORMVAR BACKING

E_d: 1.35 Mev at 45 degrees

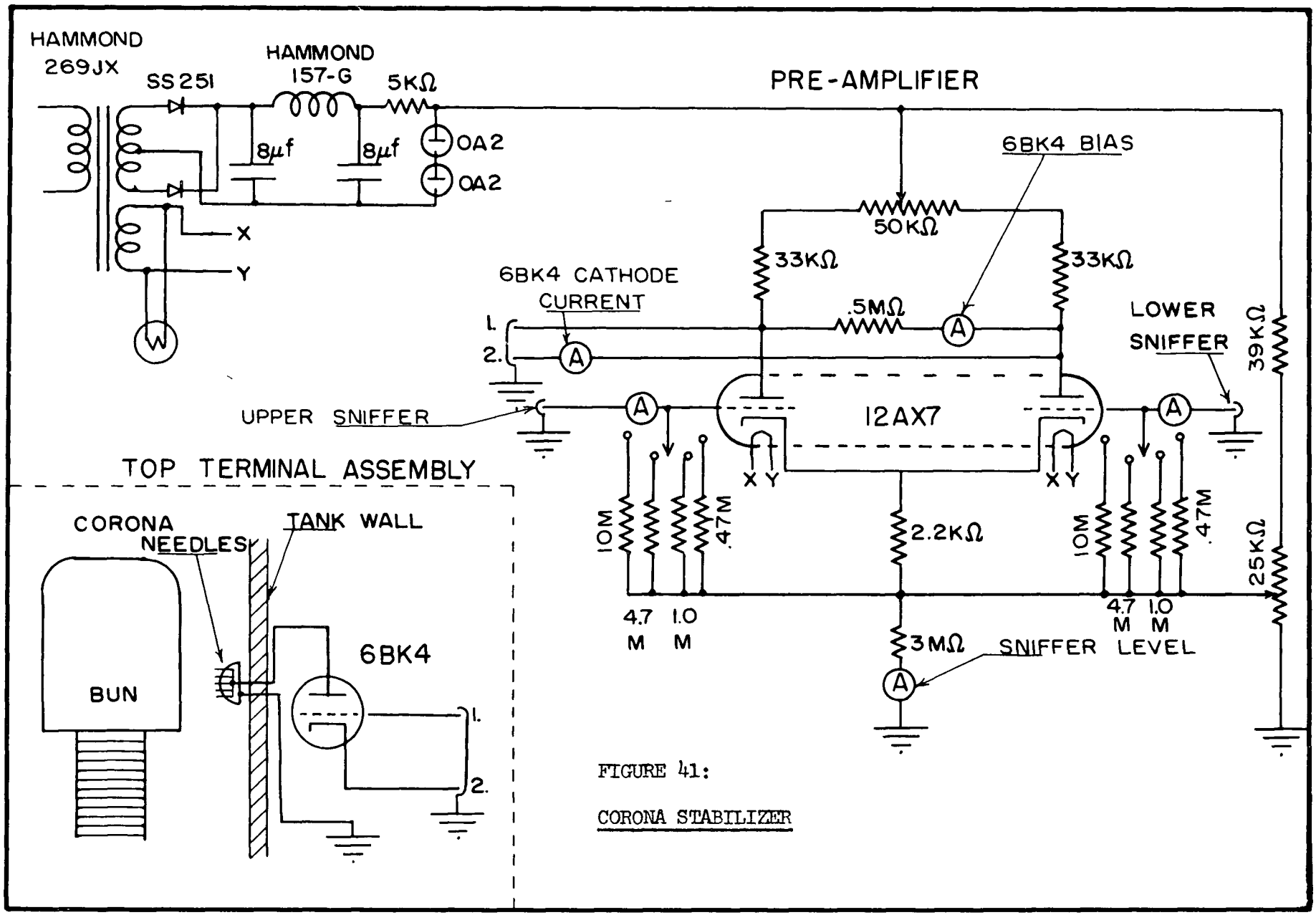

FIGURE 41:

CORONA STABILIZER

FIGURE 43.
CORONA NEEDLE ASSEMBLY

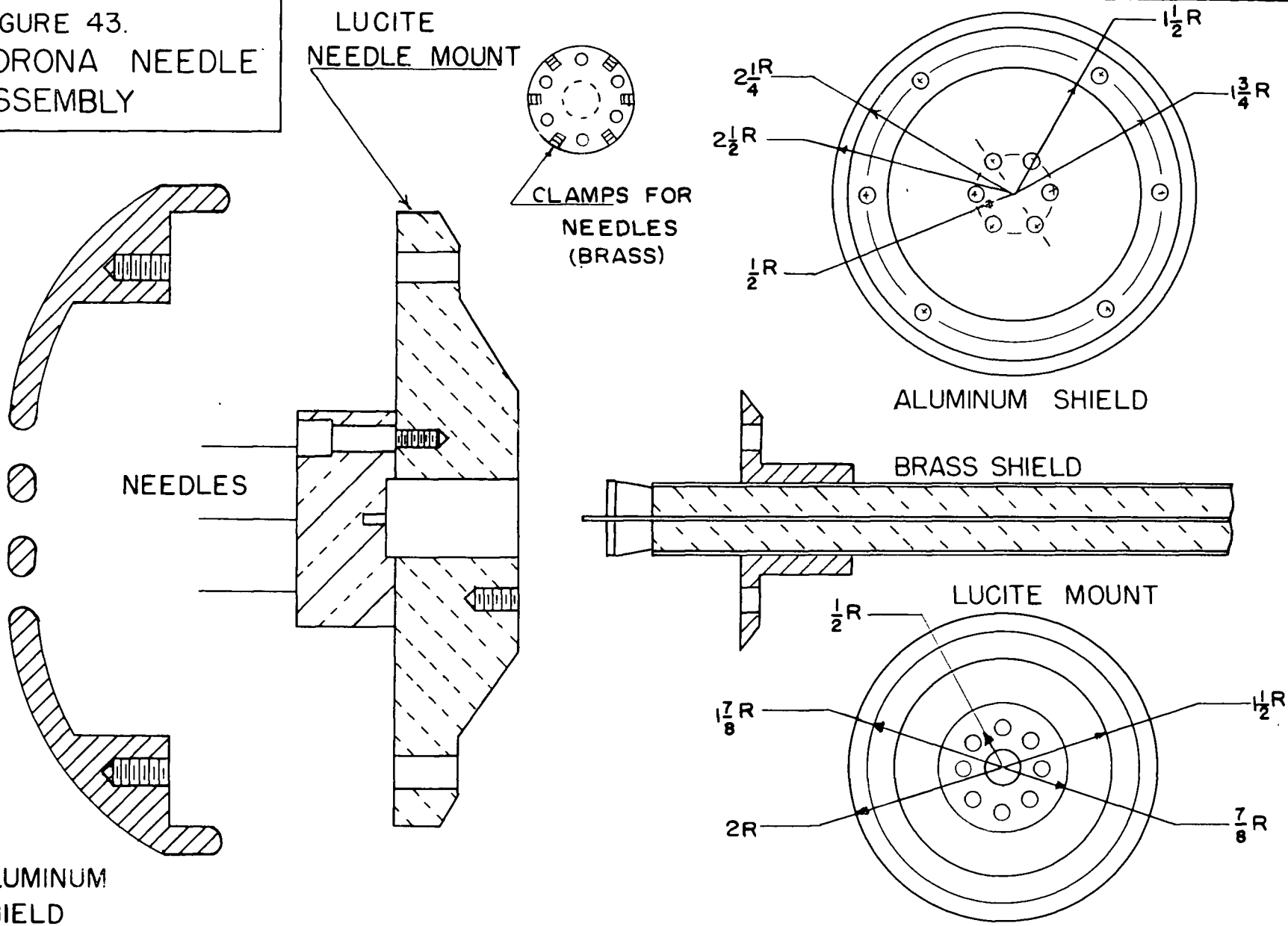

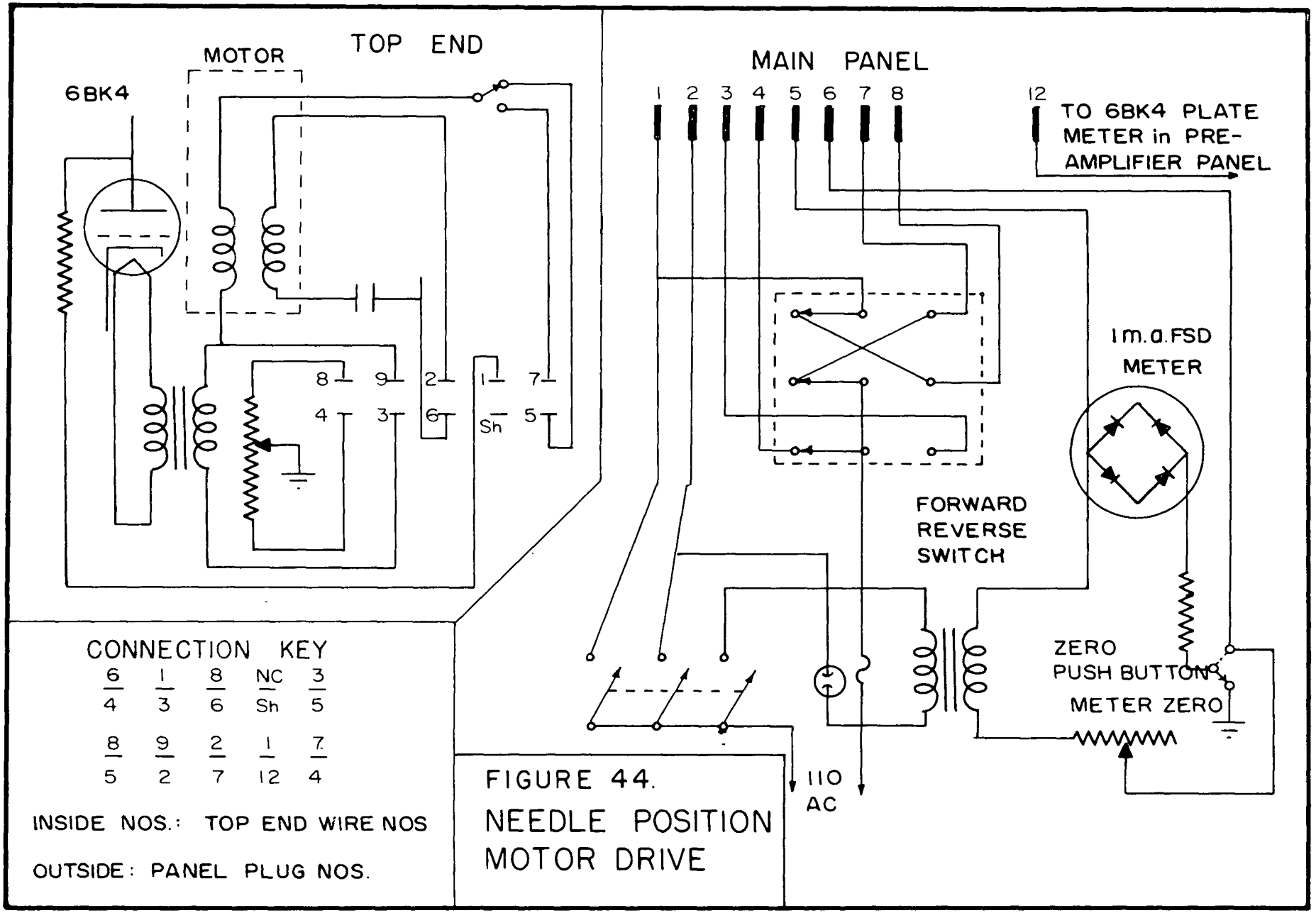

FIGURE 44.
NEEDLE POSITION
MOTOR DRIVE

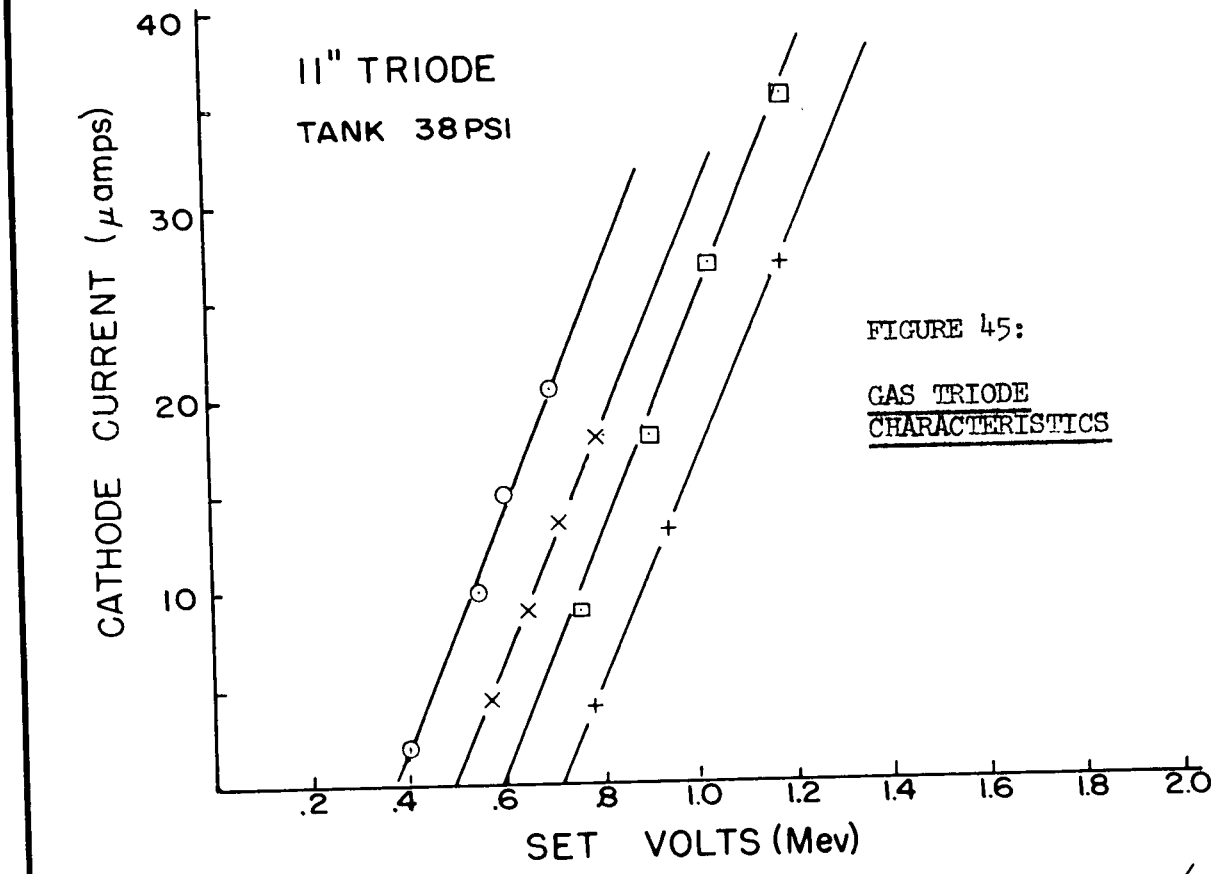

FIGURE 45:

GAS TRIODE CHARACTERISTICS

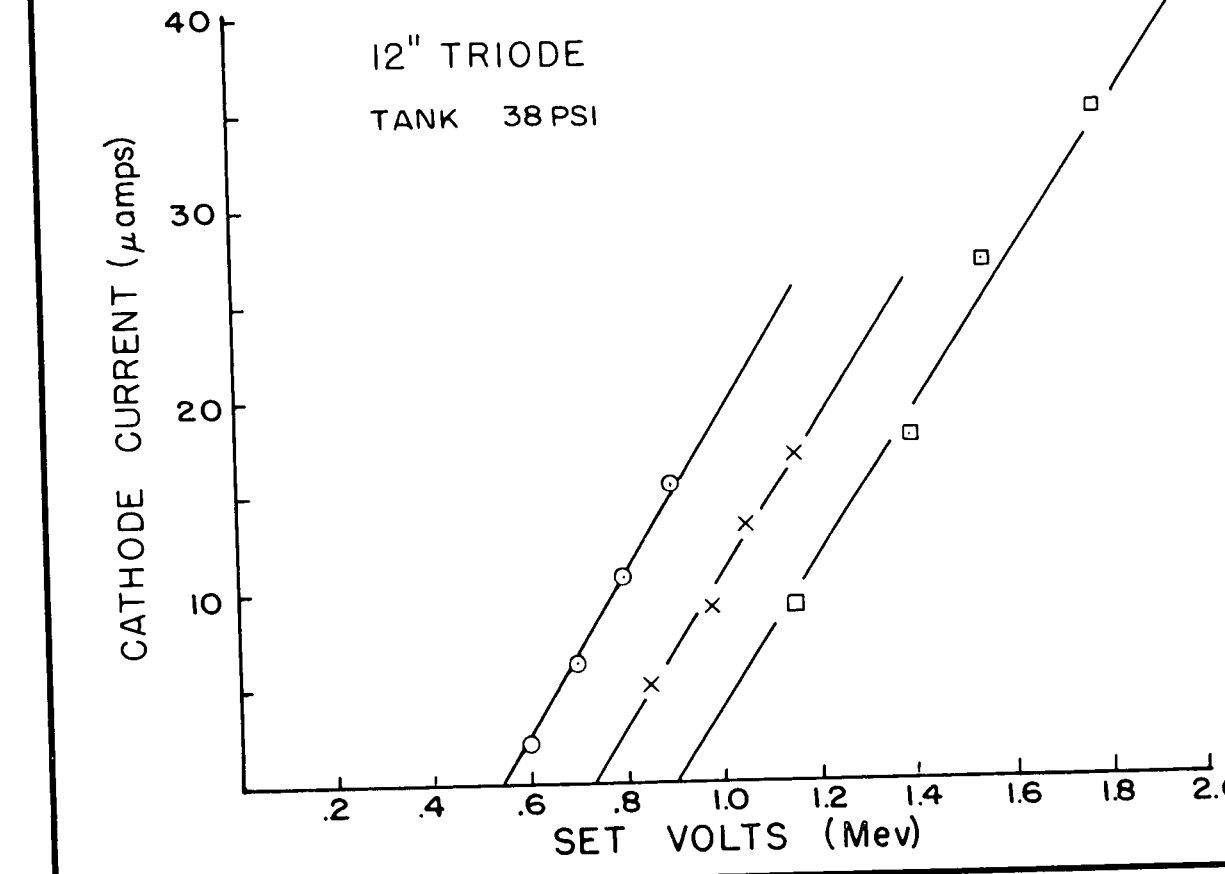

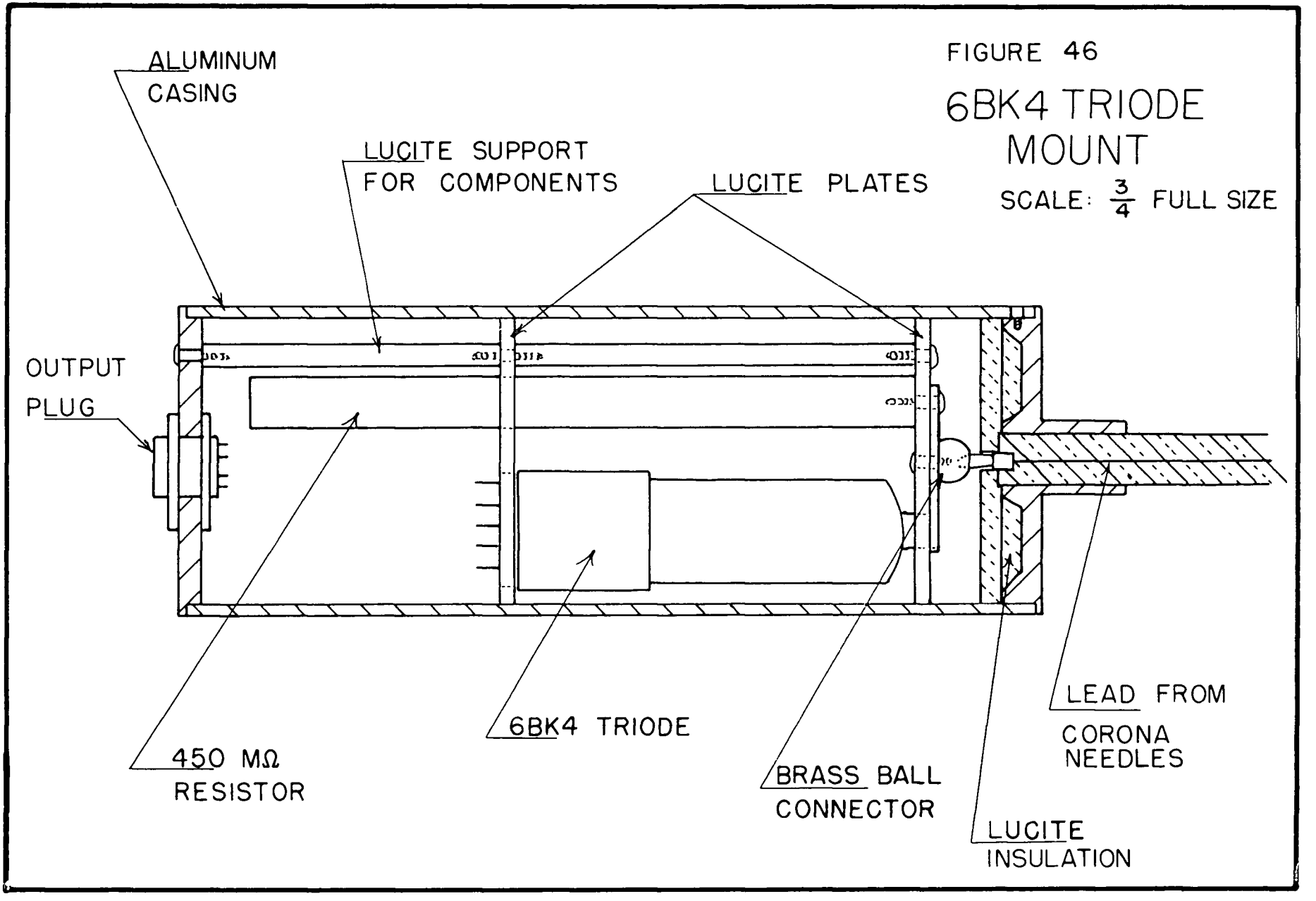

FIGURE 46

6BK4 TRIODE MOUNT

SCALE: $\frac{3}{4}$ FULL SIZE

FIGURE 49b

FOCUSED BEAM

$J = A e^{-x^2 - .04y^2}$

CROSS-SECTION

at $y = 0$

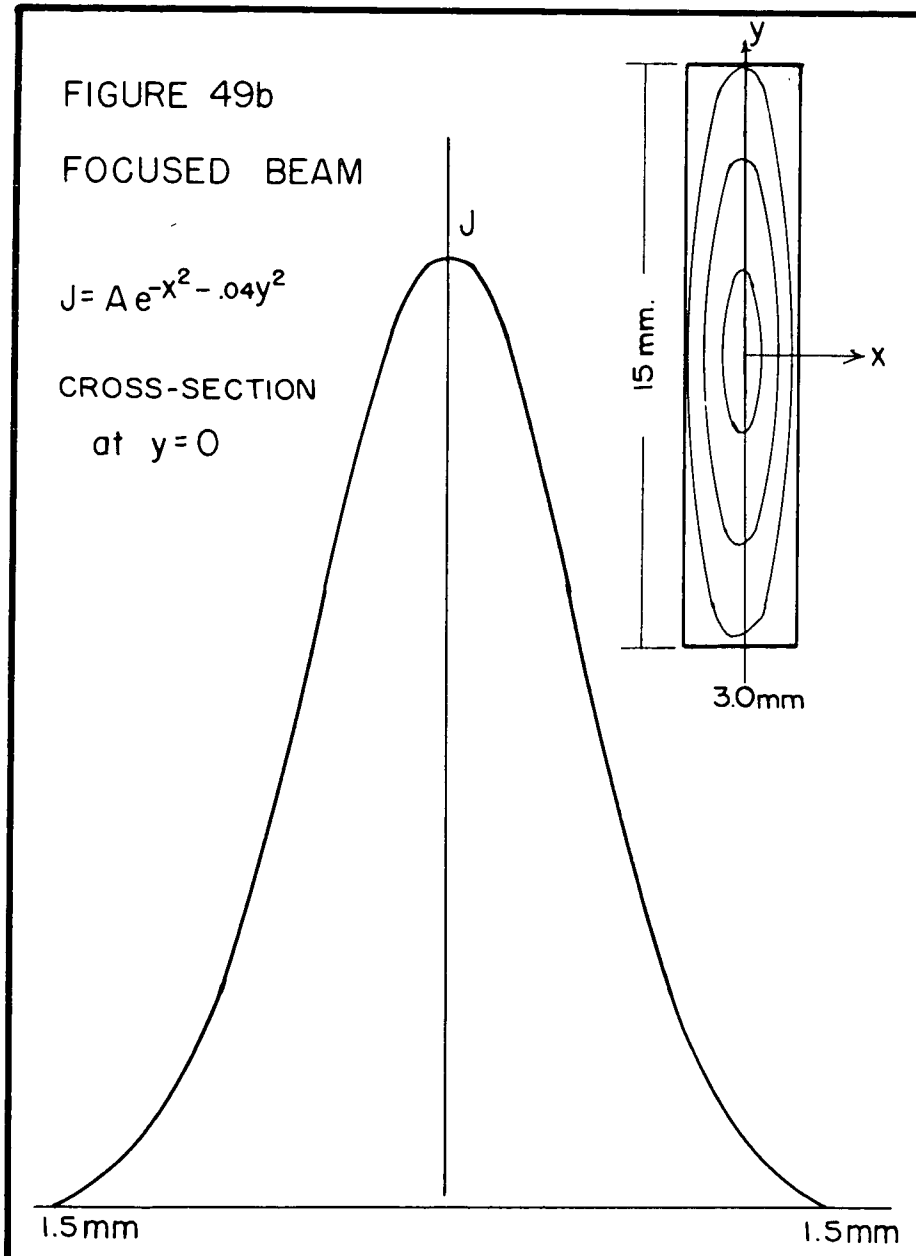

UPPER SNIFFER

BEAM

LOWER SNIFFER

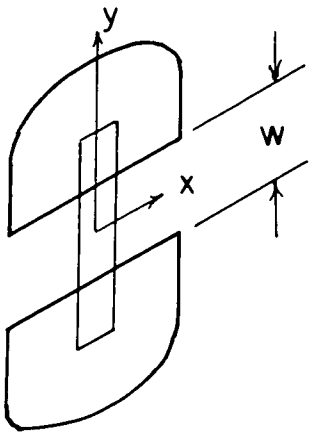

FIGURE 49a

UNFOCUSED BEAM

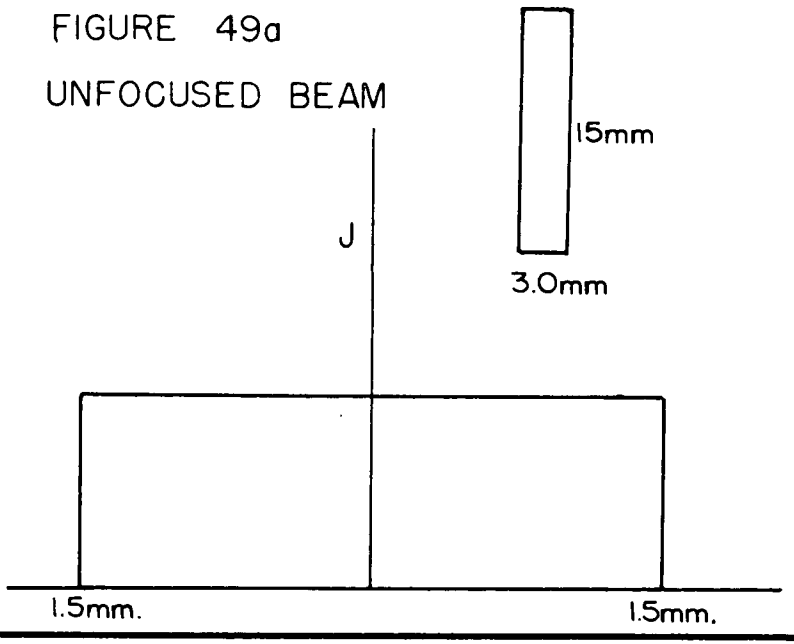

FIGURE 50a:

LOOP GAIN VS
BEAM ENERGY

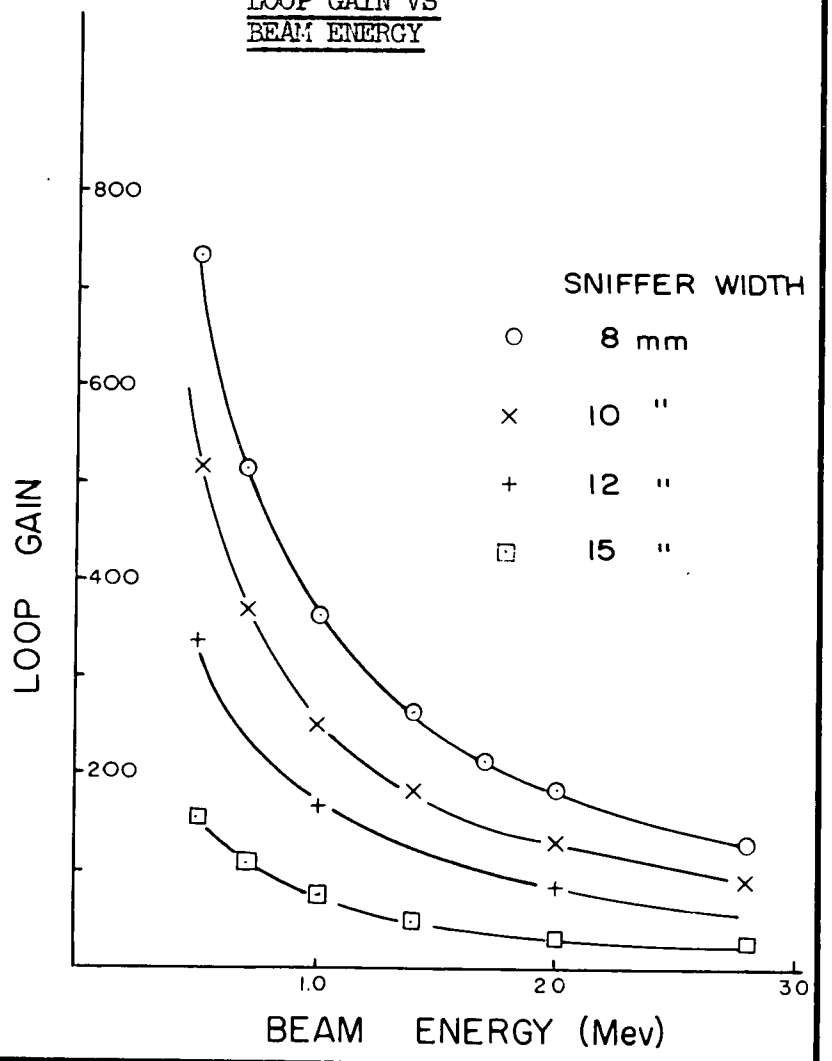

FIGURE 50b:

LOOP GAIN VS SNIFFER WIDTH

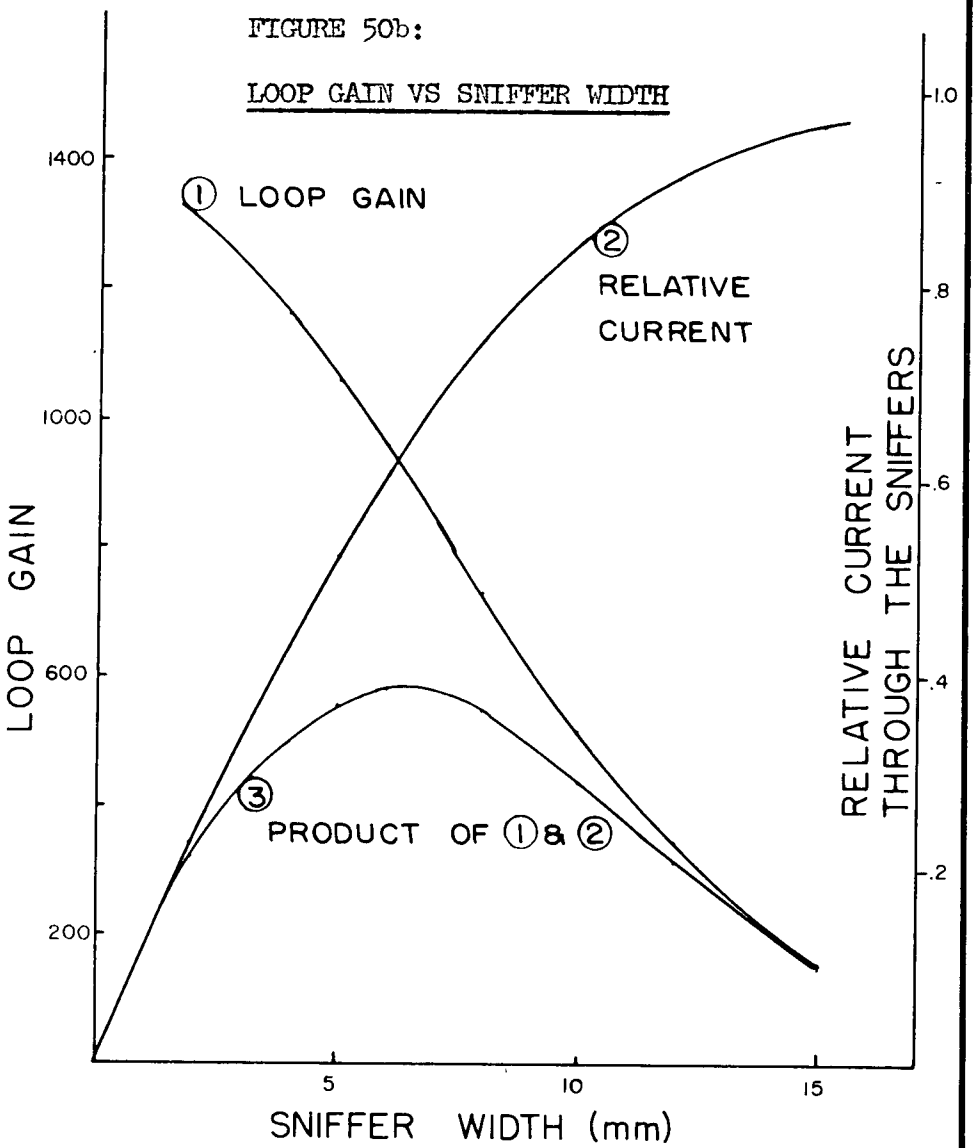

FIGURE 51a:

MAXIMUM ENERGY OF STABILIZATION WITH AND WITHOUT FREON

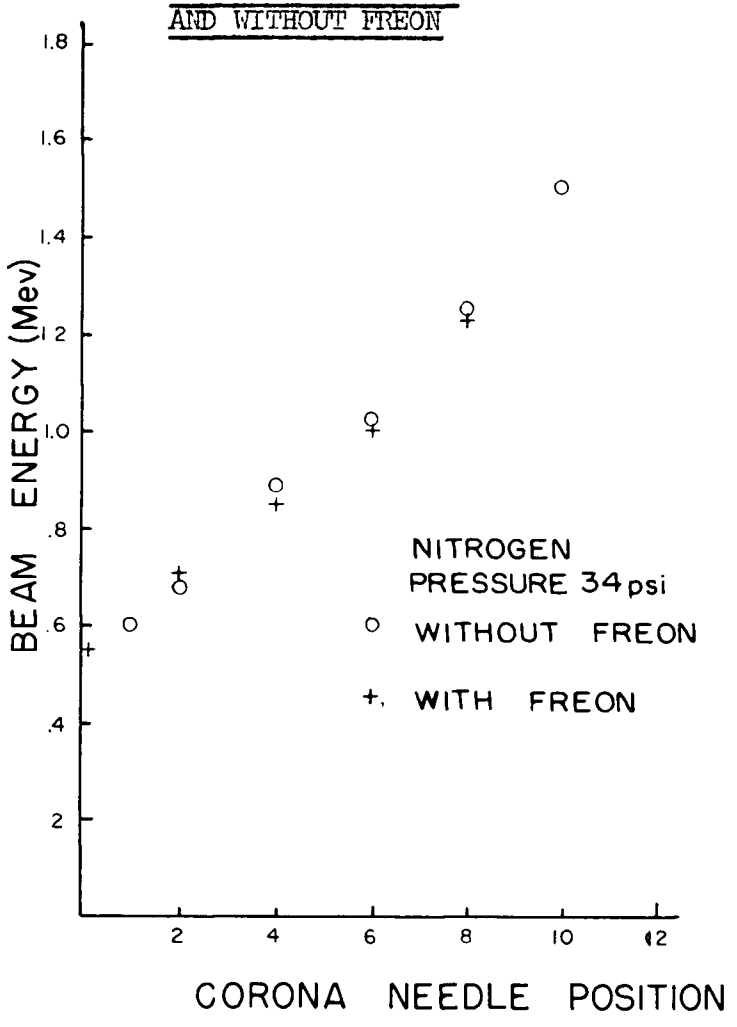

FIGURE 51b: .

STABILIZATION RANGE VS RELATIVE HUMIDITY OF TANK NITROGEN

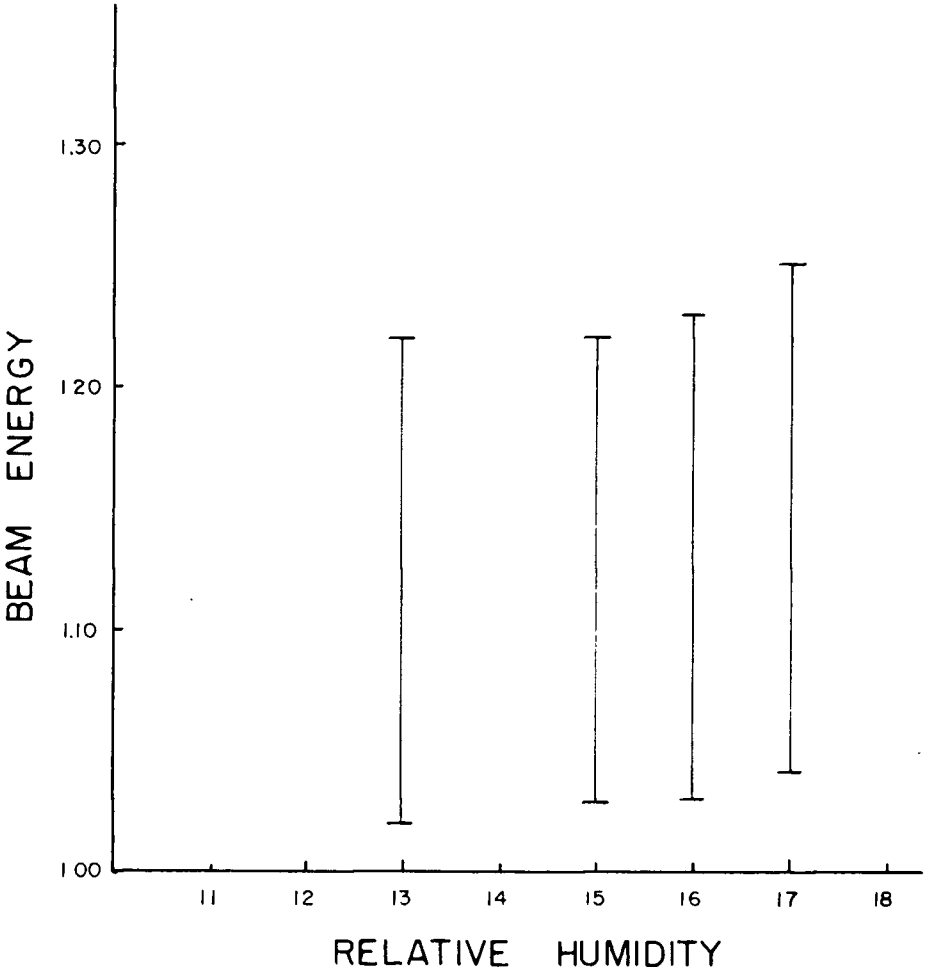

FIGURE 52:

STABILIZATION RANGE VS NEEDLE POSITION

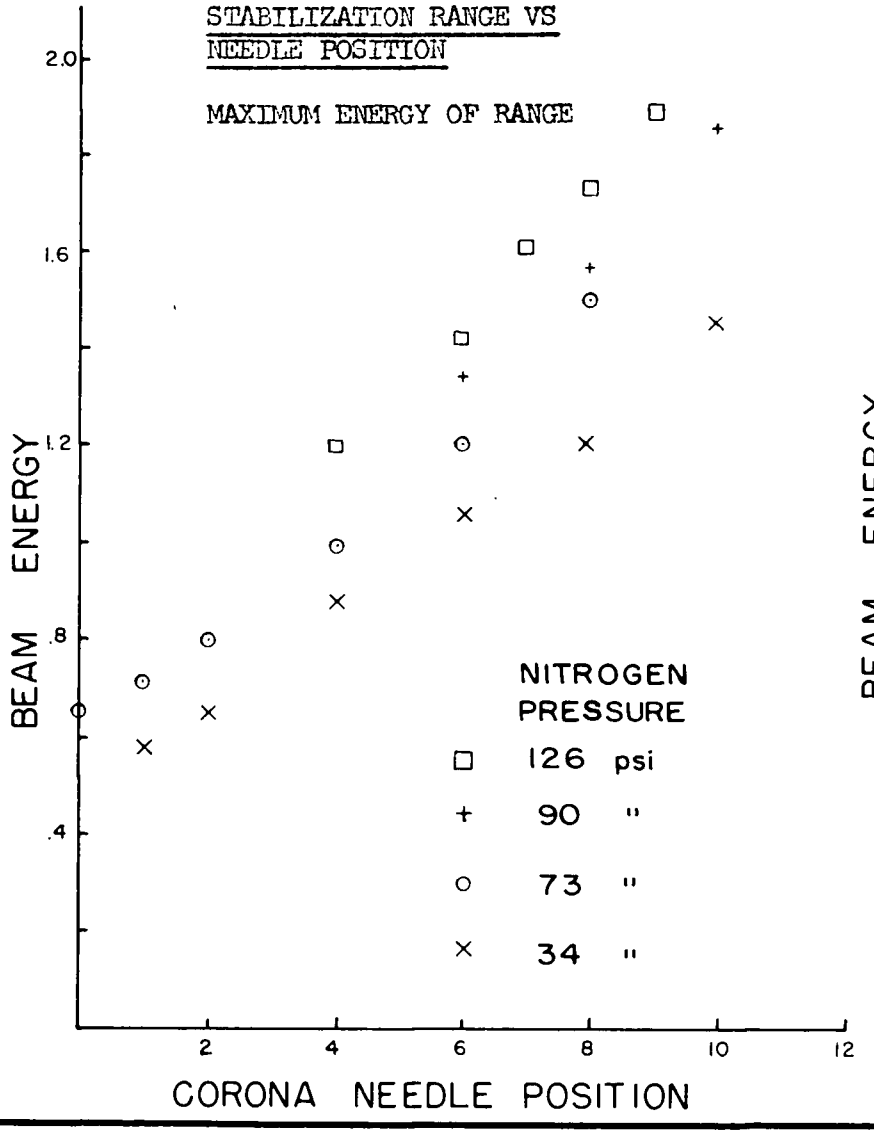

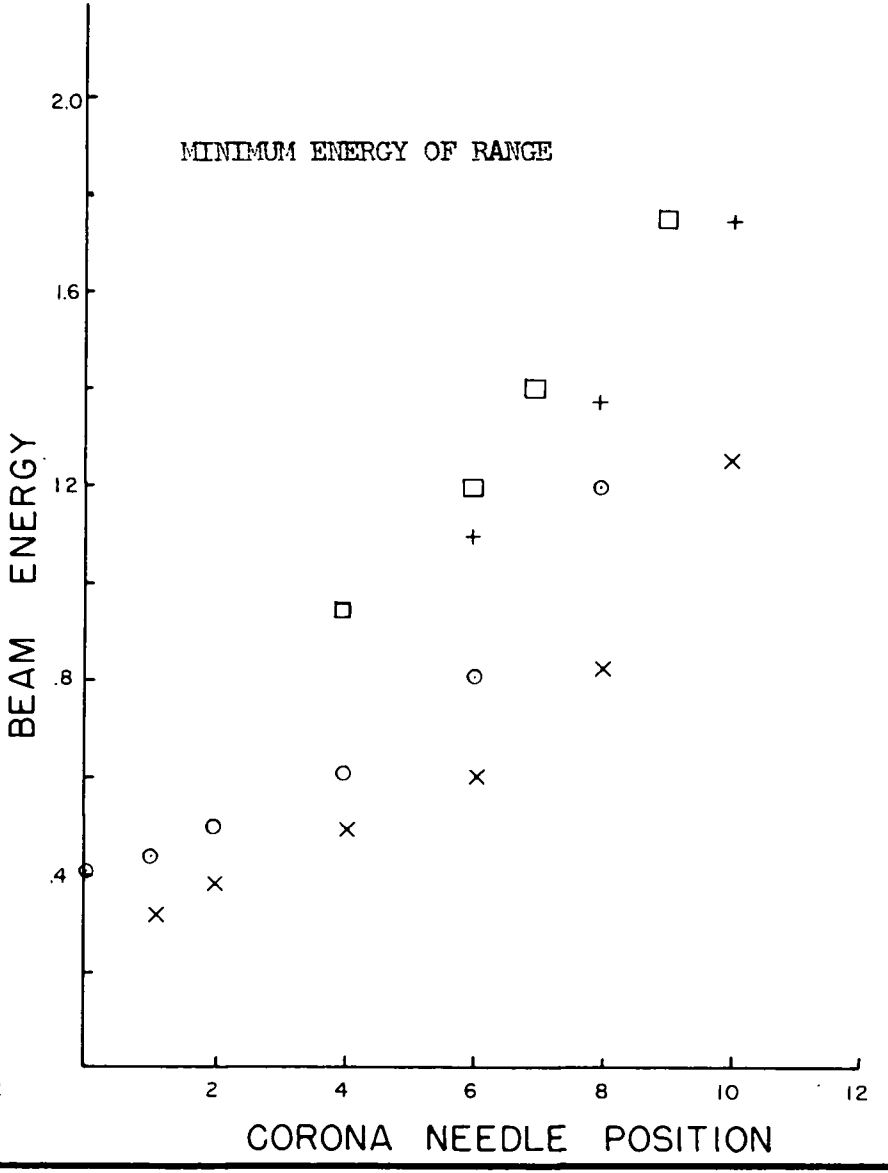

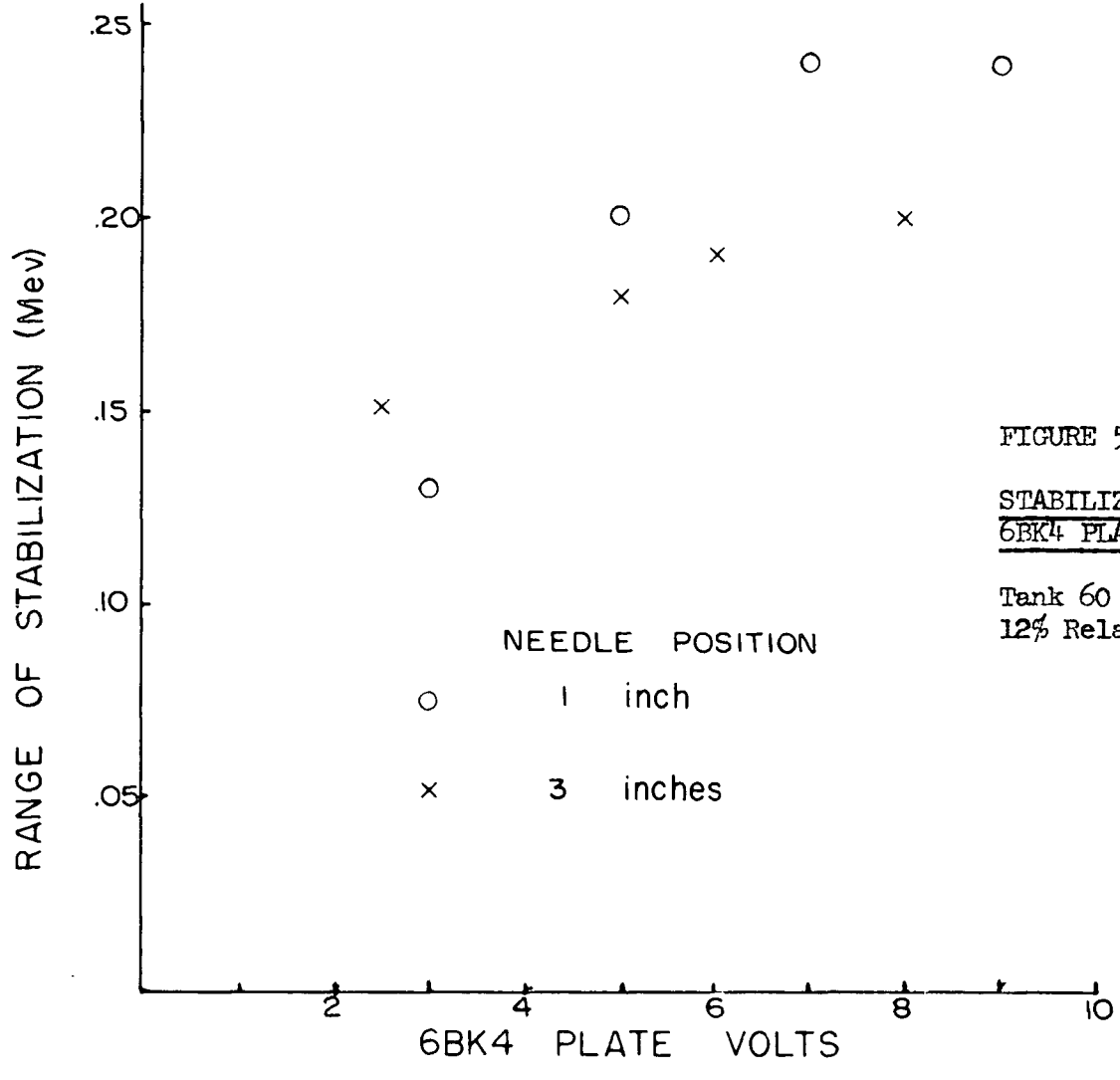

FIGURE 53:

STABILIZATION RANGE VS
6BK4 PLATE VOLTS

Tank 60 psi of Nitrogen
12% Relative Humidity

BIBLIOGRAPHY

G. Amsel, P. Baruch, O. Smulkowski, IRE Trans. on Nuclear Science, NS-8, #1, 21, (1961).

A. Ashmore and J. F. Raffle, Proc. Phys. Soc., A65, 296, 1952.

R. V. Babcock, IRE Trans. on Nuclear Science, NS-8, #1, 98, (1961).

W. L. Brown, IRE Trans. on Nuclear Science, NS-8, #1, 2, (1961).

Browne, Bul. Amer. Phys. Soc., 2, 350, (1957).

A. G. Chynoweth, and K. G. McKay, Phys. Rev. 108, 29, (1957).

G. Dearnaley, IRE Trans. on Nuclear Science NS-8, #1,11, (1961).

C. B. Garrett, and W. H. Brattain, J. Appl. Phys., 27, 299, (1956).

R. W. Gelinas, C. M. Class and S. S. Hanna, Phys. Rev., 83, 1260,(1951).

R. W. Gelinas and S. S. Hanna, Phys. Rev., 89, 483, (1953).

H. E. Gove and J. A. Harvey, Phys. Rev., 82, 658, (1951).

J. W. Haffner, Phys. Rev., 103, 1398, (1956).

W. A. Higinbotham, R. L. Chase, and G. L. Miller, IRE Trans. on Nuclear Science NS-8, #1, 147, (1961).

W. T. Joyner, H. W. Schmitt, J. H. Neiler and R. J. Silva, IRE Trans. on Nuclear Science, NS-8, #1, 54, (1961).

J. J. Jung and Pierre Cüer, Phys. Rad., 17, 555, (1956).

R. H. Kingston, J. Appl. Phys., 27, 101, (1956).

R. H. Kingston and A. L. McWhorter, Proc. IRE, 42, 1376, (1954).

T. A. Love and R. B. Murray, IRE Trans on Nuclear Science, NS-8, #1, 91 (1961).

K. G. McKay and K. B. McAfee, Phys. Rev., 91, 1079, (1953).
Phys. Rev., 84, 829, (1951).

J. M. McKenzie and G. T. Ewan, IRE Trans. on Nuclear Science, NS-8, #1, 50, (1961).

G. L. Miller, W. L. Brown, P. F. Donovan and I. M. MacKintosh, IRE Trans. on Nuclear Science, NS-7, #2-3, 185, (1960).

A. C. Prior, J. Chem. Phys. Solids, 12, 175, (1960).

Sah, Noyce, and Shockley, Proc. IRE, 45, 1228, (1957).

Seitz, Discussions Faraday Soc. #5, 271, (1949).

W. Shockley, Internation Conference on Semiconductor Physics, Prague, (1960).

R. G. Shulman and B. J. Wylunda, Phys. Rev., 102, 1455, (1956).

R. K. Smither, Phys. Rev., 107, 196, (1957).

V. S. Vavilov, J. Chem. Phys. Solids, 8, 223, (1959).

W. Whaling, "The Energy Loss of Charged Particles in Matter" Handbuch der Physik, 34, 193, (1958).

K. Wildermuth, F. C. Khanna, Y. C. Tang, Bull. Amer. Phys. Soc., #4, (1961).